

https://dspace.org/

Vector flattop beam generation for use in optical fibers

Phala, Ashley

2024
https://hdl.handle.net/10539/37482

Downloaded from a DSpace repository. https://dspace.org/

UNIVERSITY OF THE WITWATERSRAND

MASTERS DISSERTATION

Vector flattop beam generation for use in optical fibers

Author:
Ashley Phala

Supervisor:
Dr. Angela Dudley
Co-Supervisor:
Prof. Andrew Forbes

A thesis submitted in fulfillment of the requirements for the degree of Masters in Science

in the

Structured Light Laboratory
School of Physics

May 25, 2023

Declaration of Authorship

I, Ashey Phala,hereby declare that this thesis titled, "Vector flattop beam generation for use in optical fiber" represents my own work. I confirm that:

- This work was done entirely while in candidature for a MSc research degree at this University.
- In a case where any part of this dissertation has previously been presented for a degree or any other qualification at this University or any other university, this has been clearly attributed.
- Where I have consulted the published work of others, this is always clearly stated.
- Where I have quoted from the work of others, the source is always given. With the exception of such quotations, this thesis is entirely my own work.
- I have acknowledged all main sources of help.
- Where the thesis is based on work done by myself jointly with others, I have made clear exactly what was done by others and what I have contributed myself.

Signed:

Date:

"Eduation is the passport to the future, for tomorrow belongs to those who prepare for it today."

Malcolm X

UNIVERSITY OF THE WITWATERSRAND

Abstract

Faculty of Science
School of Physics

Masters in Science

Vector flattop beam generation for use in optical fibers

by Ashley Phala

Laser beam shaping with a uniform flattop profile has become a topic of interest in many industrial fields such as high-power beam delivery to a point of contact for laser cutting, welding and additive manufacturing. These applications require point of contact delivery through an optical fiber, hence we investigate how the flattop beam has changed (in terms of modal content and polarisation) when emerging from the fiber. These modes are not eigenmodes of free space as such they change their intensity profile as they propagate, and this may be overcome by the generation of vector flattop beams. In this research we exploit the polarisation dependence of a Spatial Light Modulator (SLM) to generate a vector flattop beam that preserves its intensity profile as it propagates. For this research we have experimental generated and simulated the vector flattop beam and the correlation between the two was found to be 86%. We propagate the vector flattop beam into a few mode step index fiber and apply a holistic classical toolkit to analyse the modal content and Stokes polarimetry of the vector flattop beam before and after propagating through the fiber.

Acknowledgements

I would like to express my sincerest gratitude to my supervisor Dr. Angela Dudley for the continuous support, her guidance, patience, motivation and immense knowledge. I could not have asked for a better supervisor her kindness and determination got me through my MSc study. I would also like to send my sincerest gratitude to Prof. Andrew Forbes for his insightful comments and motivation, most importantly for pushing me beyond my limits and trusting in my capabilities. I would like to send my sincere gratitude to Dr. Isaac Nape my mentor through out my study, for the constant support, the discussions we had, his insightful comments and giving me the opportunity to learn always when I ask for help. Most importantly I would like to acknowledge my family for the support and courage you gave me.

Contents

DECLARATION OF AUTHORSHIP iii

ABSTRACT vii

ACKNOWLEDGEMENTS ix

1 STRUCTURED LIGHT 1
- 1.1 INTRODUCTION . . . 1
- 1.2 PARAXIAL WAVE EQUATION . . . 3
- 1.3 GAUSSIAN BEAM . . . 5
- 1.4 LAGUERRE-GAUSSIAN BEAMS . . . 8
  - 1.4.1 MATHEMATICAL DESCRIPTION . . . 8
  - 1.4.2 ORBITAL ANGULAR MOMENTUM . . . 10
- 1.5 HERMITE GAUSSIAN BEAMS . . . 12
- 1.6 VECTOR BEAMS . . . 13
- 1.7 FLATTOP BEAMS . . . 17

2 EXPERIMENTAL TECHNIQUES 23
- 2.1 SPATIAL LIGHT MODULATOR . . . 23
  - 2.1.1 MECHANISM . . . 23
  - 2.1.2 CALIBRATION . . . 25
- 2.2 GENERATION OF SPATIAL MODES . . . 28
  - 2.2.1 LAGUERRE-GAUSSIAN MODES . . . 28
  - 2.2.2 VECTOR FLATTOP BEAMS . . . 34
- 2.3 DIGITAL MICRO-MIRROR DEVICE . . . 37
- 2.4 STOKES POLARIMETERY . . . 39
- 2.5 MODAL DECOMPOSITION . . . 44

3 FLATTOP BEAM PROPAGATION IN OPTICAL FIBER 47
- 3.1 FIBERS . . . 47
  - 3.1.1 TYPES OF FIBERS . . . 49
    - SINGLE MODE FIBERS . . . 49
    - MULTIMODE FIBERS . . . 49
    - STEP INDEX FIBERS . . . 50
    - GRADED INDEX FIBERS . . . 52
  - 3.1.2 FIBER PARAMETERS . . . 53
  - 3.1.3 COUPLING EFFICIENCY . . . 54
- 3.2 VECTOR FLATTOP BEAM PROPAGATION IN OPTICAL FIBER . . . 57
- 3.3 POLARISATION AND MODE COUPLING ANALYSIS . . . 59
  - 3.3.1 STOKES POLARIMETRY . . . 59

3.3.2 MODAL COUPLING 60

4 CONCLUSION AND FUTURE WORK **69**
4.1 FUTURE WORK 70

BIBLIOGRAPHY **73**

List of Figures

1.1 2-D intensity profiles of different beams that we can generate in the laboratory. . . . 2
1.2 A cross-section of the center of a Gaussian beam indicating its characteristics and evolution during propagation. . . . 7
1.3 A (a) 3D plot and (b) 2D density profile of a Gaussian beam intensity distribution at the beam waist ($z = 0$). . . . 8
1.4 Simulated LG modes with various azimuthal (l) and radial (p) indexes . . . 9
1.5 Illustrates (a) the 3D wavefronts and (b) the transverse intensity distribution for l = [-3,3]. . . . 11
1.6 2-D intensity profiles of HG beams. . . . 13
1.7 (a) is the example of scalar beams and (b) is the vector vortex beam profile intensities with uniform and non uniform state of polarisation, the arrows indicate the linear polariser which projects the beam into respective polarisation states which results in the intensity distribution shown on the right. . . . 15
1.8 An illustration of a higher order Poincaré sphere for $\pm\, l$ where l = [-1,1]. . . . 17
1.9 illustration of a Gaussian beam with a decay intensity from the center of the beam and a flattop beam with a uniform intensity profile. . . . 18
1.10 Illustration on how we can transform a Gaussian beam at $p = 2$ to a flattop beam at $p = 10$. . . . 19
1.11 3D intensity profile of a scalar beam as it propagates in the z direction over a distance of 4m. . . . 19
1.12 Intensity distribution of a LG_{00} (Gaussian), LG_{01} (vortex) and resultant flattop beam. . . . 20
1.13 Propagation of a vector flattop beam over a distance of 10m. . . . 20

2.1 A conceptional cross section of a liquid crystal SLM. For an incident beam that has the polarisation e_0 and e_n a spatially varying phase delay $\theta(x, y)$ can be observed by rotating the liquid crystals on the SLM. . . . 24
2.2 Schematic diagram that shows an experimental setup for calibrating a SLM. . . . 26
2.3 A plot showing the 1 dimensional intensity distribution of the interference pattern of a particular gray level. . . . 27
2.4 Plot showing the phase shift before and after calibration. . . . 27

2.5 Mode generation and detection using digitally encoded holograms on the SLM. A Gaussian beam is illuminated on the phase-only SLM that is encoded with an azimuthal phase profile. The output is a vortex mode. 29
2.6 Encoded SLM holograms displaying a sinusoidal gratings. . . 30
2.7 An experimental setup that we use to generate spatial modes. A laser (Gaussian) beam is illuminated on the SLM display screen encoded with a hologram with a transmission function given by Equ.(2.9). 32
2.8 2-D intensity profile of the LG modes with indices l and p. The inserted diagrams are the simulated LG beams. 33
2.9 Graph illustrating the correlation between LG modes $(l, p) = (1, 0)$, the purple line represented the simulated LG and the oriange line represents the experimentally generated mode. . 34
2.10 Experimental setup used to generate vector flattop beams. . . 35
2.11 By rotating the angle on the HWP, we can show the evolution from a Gaussian beam, vortex beam to a vector flattop beam. . 36
2.12 Illustration of 1-D intensity profile of the correlation between the simulated and experimentally generated vector flattop beams. 36
2.13 Schematic diagram of a simulated elongated vector flattop beam. 37
2.14 DMD chipset with a microscopic structure of the two dimensional array and a close-up view of the single pixel[46]. 38
2.15 A schematic showing the three possible states of the DMD, on-state, parked state and the off-state. 38
2.16 Diagram visualising the relationship between the polarisation ellipse and Poincaré sphere [52]. 40
2.17 Intensity measurements of a vector flattop beam, from the intensity measurements we can determine the Stokes parameters. 41
2.18 Stokes parameters of a vector flattop beam. 42
2.19 Reconstructed polarisation state of a vector flattop beam. . . . 42
2.20 Experimental setup used to determine the Stokes parameters. A 633 nm HeNe laser was passed through a HWP, a diagonally polarised beam was illuminated on the SLM display encoded with a phase-only vortex to generate a vector flattop beam. A QWP and linear polariser (LP) were then orientated at various angles to acquire four intensity measurements, of polarised components, which can be used to obtain the Stokes parameters. 43
2.21 Experimental setup used to generate and detect spatial modes. 46

3.1 Diagram of an optical fiber. The core is used to guide light through total internal reflection, the cladding has a lower refractive index as compared to that of the core and the coating is the outer layer that is used to protect the core of the fiber. . . 48
3.2 The total internal reflection phenomenon is used to propagate light in a homogeneous optical fiber. 48
3.3 Diagram of a single mode (uni-mode) fiber, the line represents the Gaussian mode as it propagates through the fiber. 49

3.4 Diagram of a multimode fiber, because of its big core size this fiber can support more than one mode as illustrated by the different lines. 50
3.5 Illustration of the first 6 $LP_{l,1}$ modes guided through multimode optical fiber, r represents the core radius of the optical fiber and $n(r)$ is the refractive index of the fiber. 50
3.6 Diagram of a step index fiber. The core possesses a high but uniform refractive index as compared to the cladding. 51
3.7 Illustration of a graded index fiber. The refractive index approximates a parabolic function and decreases as it moves away from the radial axis. 52
3.8 Modes that are supported by the 780 - 970 nm single mode fiber when used with the 633 nm wavelength. 54
3.9 Dispersion curve of different modes as they propagate through the fiber, the doted line represents the V parameter given by 4 in this case meaning the fiber supports 4 modes and the fundamental mode [78] 54
3.10 Plot of the experimental and theoretical coupling efficiency for a single mode fiber. 56
3.11 Experimental setup used to generate a vector flattop beam, which was coupled into a step index fiber and subsequently detected after emerging from the fiber. 58
3.12 1-D intensity profiles of the vector flattop beams before and after propagating through the fiber and the 2-D intensity profiles of the flattop before and after the fiber. 58
3.13 Illustrates the intensity measurements of the vector flattop: (a) is the intensity measurements before the fiber and (b) is the intensity measurements after the fiber. 59
3.14 Illustration of the 2-D Stokes parameters of a vector flattop beam: (a) before the fiber and (b) after the fiber. 60
3.15 2-D polarisation state of the vector flattop beams: (a) before the fiber and (b) after propagating through the fiber. 60
3.16 Modal decomposition of a vector flattop beam: (a) before the fiber and (b) after the fiber. 61
3.17 1-D intensity distribution of the simulated and experimental vortex and Gaussian beams 62
3.18 2-D simulated intensity measurements of (a) the vortex beam and (b) the Gaussian beam before the fiber. 62
3.19 Illustrates simulated (a) Stokes parameters of the vortex beam and (b) is the Stokes parameters of the Gaussian beam before the fiber. 63
3.20 Simulated reconstructed polarisation state of the vortex and Gaussian beam respectively. 63
3.21 Illustration of 1-D intensity profiles of the vector flattop beams before the fiber, generated by injecting only a Gaussian beam into the fiber and generated by injecting only a vortex beam into the fiber. 64

3.22 2-D intensity measurements of the flattops after the fiber (a) generated by injecting only a vortex and (b) generated by injecting only a Gaussian. 64
3.23 Stokes parameters of the flattop beam after the fiber (a) generated by injecting only a vortex and (b) generated by injecting only a Gaussian. 65
3.24 2-D reconstructed polarisation state of the flattop after the fiber (a) generated by injecting a vortex and (b) generated by injecting only a Gaussian beam into the fiber. 65
3.25 The simulated modal decomposition of the (a) Gaussian beam and (b) Vortex beam respectively before the fiber. 66
3.26 Modal decomposition of flattop beams after the fiber (a) generated by injecting only a vortex and (b) generated by injecting only a Gaussian beam. 66

4.1 Illustration of how the fiber sees the modes propagating under different condition, with no stress or bending and when the fiber is bent. 70

List of Tables

2.1 Table showing the orientation of the QWP fast axis and LP transmission axis used to obtain intensity measurements required. 43

3.1 Table of the difference between the step index fiber and graded index fiber [75]. 52

Dedicated to my family. What a long, hard and twisted road it's been...

Chapter 1

Structured light

In this research we study the different properties of light and how we can tailor this properties to generate what we call a vector flattop. We exploit the polarisation dependence of the Spatial Light Modulator (SLM) to generate vector flattop beam. We study the propagation of light (Gaussian beam) through an optical fiber and calculate the coupling efficiency. Lastly we propagate the vector flattop beams through the fiber. The aim of this research is to study how the properties (modal content and Stokes Polarimetry) differ before and after the fiber.

1.1 Introduction

Archimides was the first physicist to demonstrate beam shaping between 213 to 211 BC, in which a set of mirrors were devised using polished pieces of flat metal to break up incident light and focus it onto a single target [1]. French physicist called Augustine-Jean Fresnel developed the Fresnel lens in the 1700s, which was the first physical beam shaping optical element used in a lighthouse for navigating the cruise ships along the coastline [1]. The technology of beam shaping can be applied to both coherent and incoherent light. In the 1900s newer techniques for shaping incoherent light were introduced which involved the non-imaging methods and the use of reflective and refractive optical systems in order to increase the intensity of solar radiation by focusing it the desired region [2]. During the 1980s the shaping of coherent light took place after the emergence of the laser, with its full evolution established over the following decades. Early laser light shaping was first performed using the reflective, refractive and adaptive optical systems to modulate the phase and amplitude of the laser both externally and internal to laser resonator cavities. Lately modern techniques that involve encoding digital holograms on computer controlled light modulator devices made up of pixelated array of micro-mirrors and cells of liquid crystals are used to shape light. These devices provide more control and robustness in optical experiments, because the orientation of the micro-mirrors are computer controlled and enable dynamic beam shaping abilities.
Beam shaping refers to the process of altering the phase, amplitude and polarisation of the initial beam to obtain a desired beam. The beam shape is described by the intensity distribution. The phase of the generated beam plays a crucial role in determining the propagation properties of the beam profile,

for example, a beam with a uniform wavefront will maintain its profile over a considerable propagation distance. Different beams can be used for different applications, e.g in laser material processing, a uniform intensity profile with steep edges is used. In laser disk technology a focused beam with fewer side lobes is used to minimize cross-talk which can be explained as a spacing between neighbouring interconnection shrinkage which results in an increase in coupling capacitance between wires. Many other beams of interest in industrial, optical communication and medical applications such as Laguerre-Gaussian beams, vector beams and Hermite-Gaussian beams among others are used [3]. Experimentally beam shaping can be referred to as a process in which an incident light source is directed onto an optical system such as a Spatial Light Modulator (SLM) or a Digital Micro-mirror Device (DMD) that modulates either the phase and amplitude or both to generate the desired output beam at the observation plane. This can mathematically be expressed as follows

$$u(x,y) = A(x,y)e^{i\phi} \tag{1.1}$$

where ϕ is the phase of the beam and A is the amplitude. Figure 1.1 below shows a simulation of structured beams that can be generated in the laboratory.

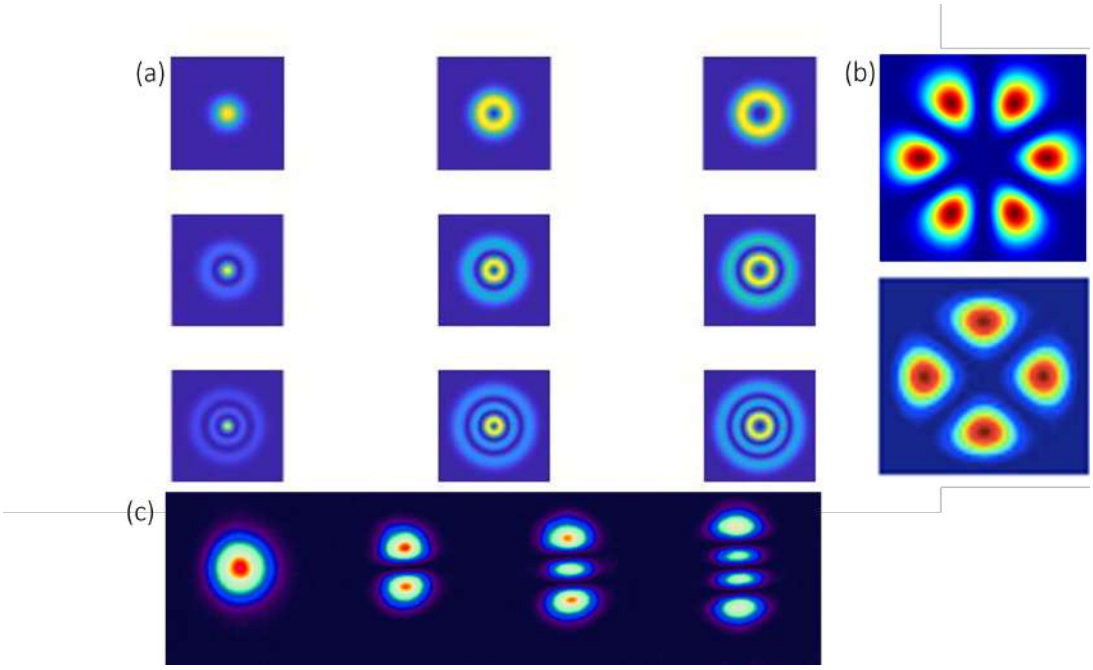

FIGURE 1.1: 2-D intensity profiles of different beams that we can generate in the laboratory.

From fig. (1.1) shown above, (a) is the intensity profile of different Laguerre-Gaussian (LG) beams, (b) are the petal beams that can be generated by superposition of two or more LG beams and (c) is the 2-D intensity profile of Hermite-Gaussian beams.
In this chapter we derive the Helmholtz wave equation. This equation is a solution to many beams such as the Gaussian beam, Laguerre-Gaussian beams

and Hermite Gaussian beams among others. We discuss the orbital angular momentum (OAM) and show examples of beams that posses OAM. We look at the difference between scalar and vector beams, and lastly we look at different techniques that we can use to generate vector flattop beams and compare the properties of vector flattop and scalar flattop beams.

1.2 Paraxial wave equation

Maxwell's equations will be used to derive the Helmholtz wave equation which governs the propagation of electric and magnetic waves and also apply to the paraxial equation to simplify the Helmholtz equation further [4]. Maxwell's equations contain the wave equation for the electromagnetic wave. The Maxwell's equations in their differential form can be written as follows

$$\nabla \times \mathbf{E} = -\frac{\partial \mathbf{B}}{\partial t}, \tag{1.2}$$

$$\nabla \times \mathbf{H} = -\frac{\partial \mathbf{D}}{\partial t} + \mathbf{J}, \tag{1.3}$$

$$\nabla \cdot \mathbf{D} = \rho, \tag{1.4}$$

$$\nabla \cdot \mathbf{B} = 0. \tag{1.5}$$

The bold format represents the vectors and $\nabla = \frac{\partial \hat{x}}{\partial x} + \frac{\partial \hat{y}}{\partial y} + \frac{\partial \hat{z}}{\partial z}$ is the del operator in 3-dimensional Cartesian coordinates, spanned by the orthogonal unit vectors denoted as $[\hat{x}, \hat{y}, \hat{z}]$. These equations are used to describe the relationship between electric field $(\mathbf{E})$, magnetic flux density $(\mathbf{B})$, electric flux density $(\mathbf{D})$, the magnetic field strength $(\mathbf{H})$, current density $(\mathbf{J})$ and the volume charge density (ρ). The $(\mathbf{H})$ magnetic field strength and the flux densities for both the electric and magnetic cases in vacuum can further be expressed as follows

$$\mathbf{D} = \epsilon_0 \mathbf{E}, \tag{1.6}$$

$$\mathbf{H} = \frac{1}{\mu_0} \mathbf{B}. \tag{1.7}$$

Where ϵ_0 and μ represents the permittivity and permeability of the free space respectively [5]. The above equations are a special case for a more general relation in any medium, and can be expressed as follows

$$\mathbf{D} = \epsilon_0 \mathbf{E} + \mathbf{P}, \tag{1.8}$$

$$\mathbf{H} = \frac{1}{\mu_0} \mathbf{B} - \mathbf{M}. \tag{1.9}$$

Where $\mathbf{P}$ denotes the polarisation density and $\mathbf{D}$ is the dielectric properties of the medium, $\mathbf{M}$ represents the magnetization density and $\mathbf{H}$ is the magnetic property of the medium.
In the absence of currents and sources the Maxwell's equations result in the

wave equation for both magnetic and electric fields. We can derive the electric field in a vacuum.
Considering the curl of Faraday's law of induction, which is shown in Eq.(1.2)

$$\nabla \times (\nabla \times \mathbf{E}) = \nabla \times \frac{-\partial \mathbf{B}}{\partial t}. \tag{1.10}$$

By implementing the identity $\nabla \times (\nabla \times \mathbf{E}) = \nabla(\nabla \cdot \mathbf{E})$, so that

$$\nabla \times (\nabla \times \mathbf{E}) = \nabla(\nabla \cdot \mathbf{E}) - \nabla^2 \mathbf{E} = \nabla \times (-\frac{\partial \mathbf{B}}{\partial t}) \tag{1.11}$$

Assuming that the is no charge density ($\rho = 0$), Eq.(1.11) becomes

$$-\nabla^2 \mathbf{E} = \frac{\partial(\nabla \times \mathbf{B})}{\partial t} \tag{1.12}$$

The magnetic field can be eliminated by exploiting Eq.(1.3) and Eq(1.6-1.7) and assuming that in a vacuum $J = 0$

$$\nabla \times \mathbf{H} = \tfrac{1}{\mu_0} \nabla \times \mathbf{B} = -\tfrac{\partial \mathbf{D}}{\partial t} + 0 = -\epsilon_0 \tfrac{\partial \mathbf{E}}{\partial t},$$

$$\nabla \times \mathbf{B} = -\mu_0 \epsilon_0 \frac{\partial \mathbf{E}}{\partial t}. \tag{1.13}$$

By substituting Eq.(1.13) into Eq.(1.12) to obtain the wave equation given by

$$\nabla^2 \mathbf{E} = \mu_0 \epsilon_0 \frac{\partial^2 \mathbf{E}}{\partial t^2}. \tag{1.14}$$

The same relation also exist for **B** The electric field in the spatial and temporal domains is given by

$$E(x, y, z, t) = U(x, y, z) T(t). \tag{1.15}$$

Most of the solutions used are associated with the scalar Helmholtz equation, the Helmholtz equation can be derived as follows, by substituting Eq.(1.15) into the wave equation given by Eq.(1.14) yields

$$\nabla^2 U(x, y, z) T(t) = \tfrac{1}{c^2} \tfrac{\partial^2}{\partial t^2} U(x, y, z) T(t),$$

$$T(t) \nabla^2 U(x, y, z) = \tfrac{1}{c^2} U(x, y, z) \tfrac{\partial^2}{\partial t^2} T(t),$$

$$\frac{1}{U(x, y, z)} \nabla^2 U(x, y, z) = \frac{1}{c^2 T(t)} \frac{\partial^2}{\partial t^2} T(t). \tag{1.16}$$

In such a way that the spatial and temporal functions are separated from each other. Since the two variables are not dependent on each other, the change in one variable will not affect the other. Assuming that both sides of Eq.(1.16) equals to constant -k^2,we have

$$\tfrac{1}{U(x,y,z)} \nabla^2 U(x, y, z) = \tfrac{1}{c^2 T(t)} \tfrac{\partial^2}{\partial t^2} T(t) = -k^2.$$

By replacing the right side of Eq.(1.16) with the constant $-k^2$, we can eliminate the temporal function. From rearranging Eq.(1.16) we obtain the Helmholtz equation

$$\frac{1}{U(x,y,z)}\nabla^2 U(x,y,z) = -k^2,$$

$$\nabla^2 U(x,y,z) = -k^2 U(x,y,z),$$

$$(\nabla^2 + k^2)U(x,y,z) = 0. \tag{1.17}$$

Where k denotes the wavenumber and it is defined as $k = \frac{w}{c} = \frac{2\pi}{\lambda}$ and w is the angular frequency. The structured beams, such as the Gaussian, Bessel, Hermite-Gaussian beams among others are all mathematical functions that solve the Helmholtz equation.

1.3 Gaussian beam

Over the past decade the use of laser beams has grown exponentially [6]. Laser beams are used in many fields such as in science and technology, medical, military and commercial [7–9]. The paraxial Helmholtz equation is known as the foundation of all the fundamental light beams and by solving this equation in cylindrical coordinates from this equation becomes a solution for the Gaussian and structured light beams such as the LG modes and the Bessel mode [7] is found. The paraxial Helmholtz equation can be written as follows

$$\nabla^2 E + 2ik\frac{\partial E}{\partial z} = 0. \tag{1.18}$$

Where E is the electric field, $k = \frac{2\pi}{\lambda}$ is the wavenumber and z is the direction of propagation. Assuming a Gaussian beam profile, the electric field is given by

$$E(r,z) = E_O(\frac{\omega_0}{w(z)})\exp(\frac{r^2}{\omega(z)^2})\exp(i\varphi(z)). \tag{1.19}$$

Where r is the radial coordinate,w_o is the waist radius and E_0 is the peak of the amplitude of the electric field. The function $\varphi(z)$ describes the phase of the wave and is given by

$$\varphi(z) = kz - arctan(\frac{z}{zR}) + \frac{kr^2}{zR(z)}. \tag{1.20}$$

Where $zR = \frac{\pi w_0^2}{\lambda}$ is the Rayleigh range, $R(z) = 2[1 + (\frac{zR}{z})^2]$ is the radius of curvature of the wavefront, and k is the wavenumber. Substituting the Gaussian beam profile equation in the paraxial wave equation we get [10]

$$E(r,z)(\frac{\partial^2}{\partial r^2} + \frac{1}{\partial r} + 2ik\frac{\partial}{\partial z}) = 0. \tag{1.21}$$

Then we can now separate the radial and axial dependence of the electric field by assuming a solution of the form

$$E(r,z) = u(r)\omega(z). \tag{1.22}$$

Substituting this solution into the paraxial wave equation and dividing through by $E(r,z)$, we obtain

$$\frac{1}{u}\frac{d^2u}{dr^2} + \frac{1}{r}\frac{du}{dr} + \frac{2ik}{\omega}\frac{d\omega}{dz} = 0 \tag{1.23}$$

Since the first two terms on the left hand side depend only on r and the last term depends only on z, the equation can be satisfied only if each term is equal to a constant. We can choose the constant to be $-k^2$, which gives two separate differential equations

$$\frac{d^2u}{dr^2} + \frac{2}{r}\frac{du}{dr} - (k^2 - \frac{r^2}{\omega^2})u = 0. \tag{1.24}$$

$$\frac{d^2\omega}{dz^2} + \frac{2k}{k^2}(k^2 - \frac{r^2}{\omega^2})\omega = 0. \tag{1.25}$$

The Eq.(1.24) is the radial part of the wave equation and has a solution of the form

$$u(r) = C\exp(\frac{r^2}{\omega^2}). \tag{1.26}$$

Where C is the constant and $w(z)$ is the radius of the beam size in the z direction. Substituting this equation back in the paraxial wave equation, gives Eq. (1.25) which has the following equation

$$w(z) = \exp(i\varphi(z)) \tag{1.27}$$

Substituting Eq.(1.26) and Eq.()1.27) back into the Gaussian beam profile we obtain

$$E(r,z) = E_0\frac{\omega_0}{\omega(z)}\exp(\frac{-r^2}{\omega(z)^2})\exp\left(i[kz - \arctan(\frac{z}{z_R}) + \frac{kr^2}{2R(z)}]\right) \tag{1.28}$$

Which is the Gaussian beam equation in polar coordinates. Where $r = \sqrt{x^2+y^2}$ is the transverse radial coordinate. Properties that characterize the propagation of the Gaussian beam and how it changes as it propagates in the z-direction are shown in Eq.(1.28). An illustration that shows how the Gaussian beam changes as it propagates in the z-direction is shown in fig.(1.2). The vertically curved lines inside the beam are showing the wavefront of the composing waves. It can be seen that the beam width which is denoted by w converges before z = 0 and diverges after z = 0 as it propagates. At z = 0 the beam waist (denoted by w_0) is at its minimal and it increases gradually as it moves away from the focal plane [11].

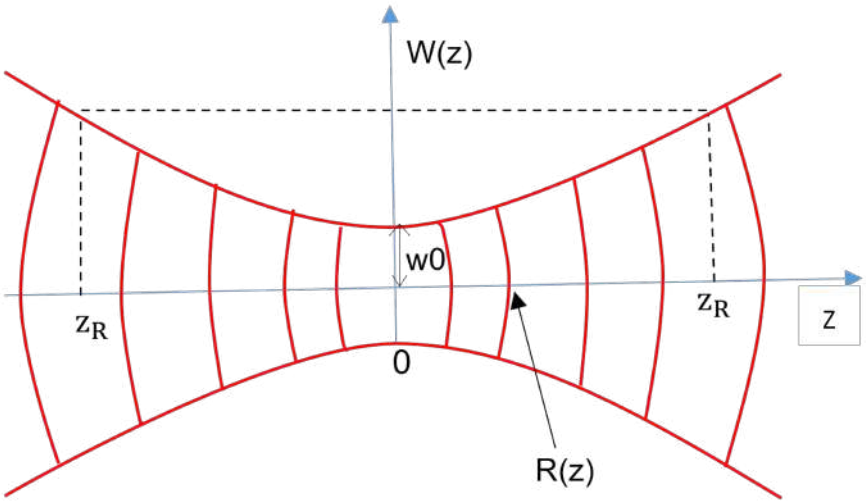

FIGURE 1.2: A cross-section of the center of a Gaussian beam indicating its characteristics and evolution during propagation.

The Rayleigh range can be used to explain how the beam width changes as the beam propagates. The Rayleigh range can be defined as the distance at which the beam width is larger than the beam waist by a factor of $\sqrt{2}$, and it can mathematically be expressed as follows

$$Z_R = \frac{\pi\omega_0^2}{\lambda} \tag{1.29}$$

Where λ is the wavelength. From Eq.(1.29) we can see that the Rayleigh range is directly proportional to the smallest transverse cross-section and inversely proportional to wavelength.
The intensity distribution of the Gaussian beam can be calculated with relation to the complex-amplitude equation in Eq.(1.30) [12].

$$I(r,z) = |\frac{\omega_0}{\omega(z)} e^{\frac{r^2}{\omega(z)^2}} e^{\frac{-ikr^2}{2R}} e^{-i\vartheta}|$$
$$= (\frac{\omega_0}{\omega(z)} e^{\frac{r^2}{\omega(z)^2}})^2 (e^{\frac{-ikr^2}{2R}} e^{-i\vartheta})(e^{\frac{ikr^2}{2R}} e^{i\vartheta})$$

$$I(r,z) = (\frac{\omega_0}{\omega(z)})^2 \exp(-2\frac{r^2}{\omega(z)^2})^2 \tag{1.30}$$

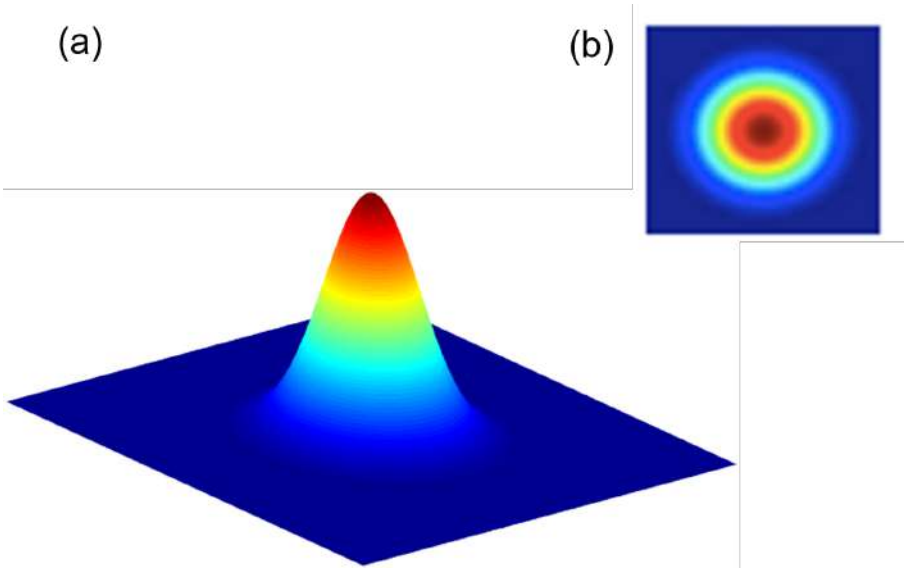

FIGURE 1.3: A (a) 3D plot and (b) 2D density profile of a Gaussian beam intensity distribution at the beam waist ($z = 0$).

Figure 1.3 illustrates the Gaussian beam intensity distribution as calculated in Eq.(1.30). Gaussian beams have a distinguished intensity profile which can be mapped to the exponential term of Eq.(1.18). Gaussian beams are known for having a peak intensity at the center of the beam where $r = 0$ and $z = 0$, and it gradually decreases as it moves outwards along the radial direction $(r \to \infty)$. This can be clearly seen in fig.(1.3a) which shows a 3D intensity distribution of the fundamental (Gaussian) beam, fig.(1.3b) is a 2D intensity distribution of the Gaussian beam.

1.4 Laguerre-Gaussian beams

1.4.1 Mathematical description

By solving the Helmholtz wave equation in cylindrical coordinates, we obtain a another set of solutions know as the Laguerre-Gaussian beams[13] . These beam play a very crucial role in our experimental work as such it is important for us to explore them. Unlike the fundamental Gaussian beam with a plane wavefront, the LG modes have helical wavefronts and these modes are usually called the doughnut shaped modes [14, 15]. The complex amplitude for the LG beams can be written as follows

$$E(r,\phi,z) = \sqrt{\frac{2p!}{\pi(p+|l|)!}}(\frac{r\sqrt{2}}{\omega})^{|l|}L_p^{|l|}(\frac{2r^2}{\omega^2})e^{\frac{-r2}{\omega^2}}e^{il\varphi}e^{\frac{-ikr^2}{2R}}e^{-i\vartheta_{p,l}}, \tag{1.31}$$

where $r = \sqrt{x^2+y^2}$ is known as the transverse radial coordinate, ϕ is the azimuthal angle and $Lp^{|l|}(x)$ is the Laguerre polynomial of the order $p \geq 0$ for ϵ Z, $l \epsilon$ Z. If $l = p = 0$, Eq.(1.31) reduces to a Gaussian solution. In comparison with the Gaussian beam solution in Eq.(1.28), the LG and Gaussian beams

have similar terms such as the beam waist (w), radius of curvature among others. The Gouy phase in this case depends on the l and p indices which is given by

$$\vartheta = (2p + l + 1)\arctan(\frac{z}{z_R}). \tag{1.32}$$

The intensities related to the LG modes can be obtained through the same method outlined for the Gaussian beams

$$I(r,z) = \frac{2p!}{\omega(z)^2\pi(p+|l|)!}(\frac{r\sqrt{2}}{\omega(z)})^{2|l|}[|L_P|^{|l|}(\frac{2r^2}{\omega(z)^2})]^2 e^{\frac{-2r^2}{\omega(z)^2}} \tag{1.33}$$

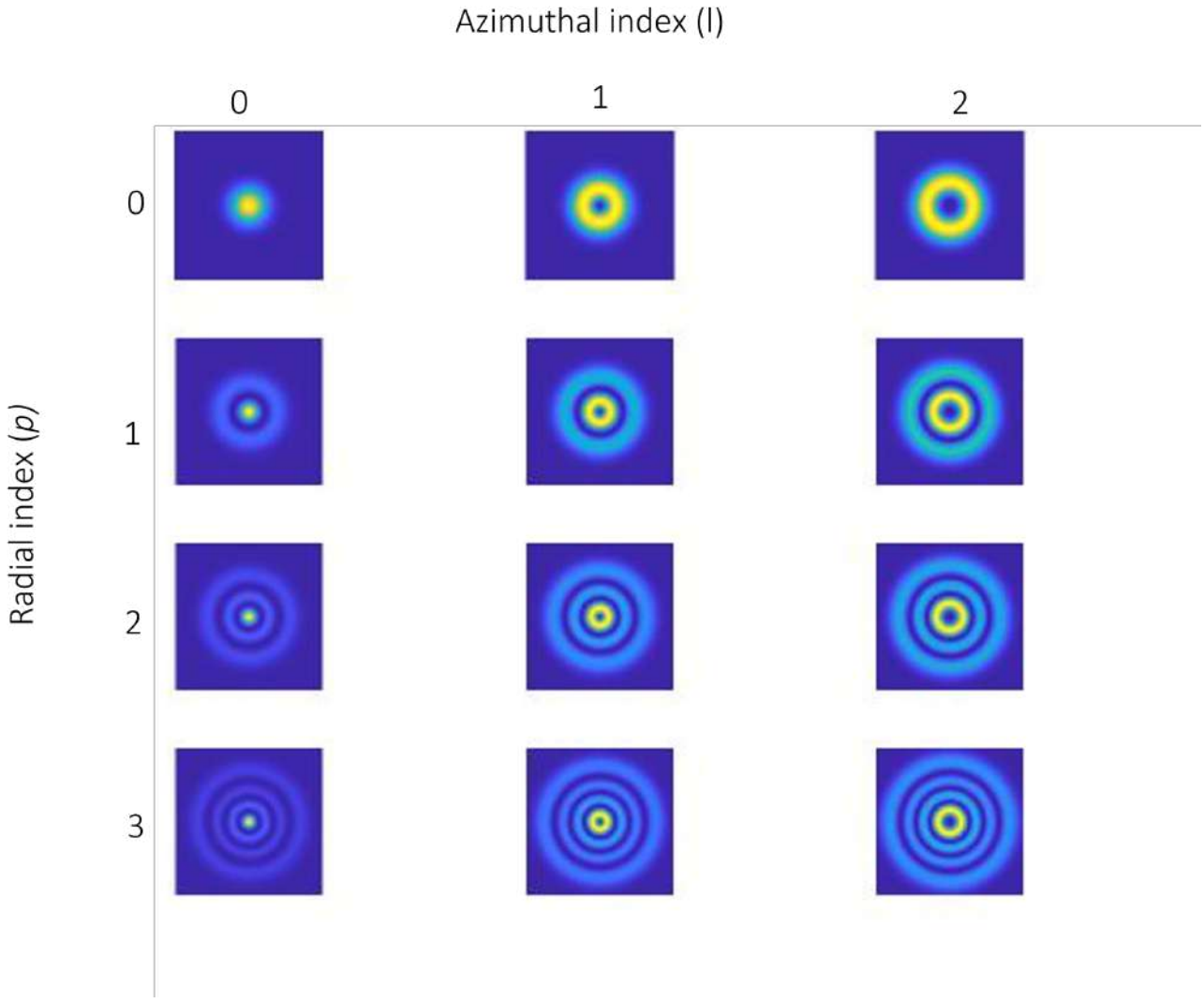

FIGURE 1.4: Simulated LG modes with various azimuthal (l) and radial (p) indexes

LG beams are derived from combining Gaussian beams and the Laguerre polynomial. Figure (1.4) illustrates various LG beams. Due to the coordinate space and cylindrical variables of this beams, they have circular symmetry. The p determines the number of radial nulls in intensity, which results in p

+ 1 concentric rings occurring in the profile distribution [16]. For instance, if $[l, p]$ = [0,2], two rings are observed inside the intensity distribution, which indicated intensity nulls, as such three intensity rings occur with correspondence to p + 1 = 3. As a result the p index is often referred to as the radial index. If we consider the l index from Eq.(1.33) a nonzero solution should be observed in order to obtain a central null (r = 0) in intensity. This null can be linked to $(\frac{r\sqrt{2}}{w})^{2|l|}$ in Eq.(1.23), in which the l-value modulates the Gaussian intensity distribution. LG beams are known to posses an OAM which is describe by $e^{il\varphi}$, in the complex amplitude equation shown above.In the next section we discuss what is OAM.

1.4.2 Orbital Angular Momentum

The electromagnetic waves are composed of both energy and momentum, where the momentum is made up of the linear momentum **P** and angular momentum **L**. The angular momentum has an extra component associated to polarization, spin angular momentum (SAM) and OAM, which is associated with the spatial distribution of the beam [17]. The OAM is the sum of the total angular momentum linked with the transverse spatial profile of the photon [18]. From the complex amplitude equation of the LG mode shown in Eq.(1.31), we notice the term $e^{il\phi}$. Where ϕ denotes the phase and l is the azimuthal index or the topological charge. OAM is the twisting of the wavefront, and it can posses both positive and negative integers i.e l =[...-2,-1,0,1,2...] [18]. We demonstrate that the OAM density is directly proportional to the topological charge l by calculating the Poynting vector [19]

$$\mathbf{S} = \frac{\mathbf{E} \times \mathbf{B}}{u_0}. \tag{1.34}$$

The vector potential in the Lorenz gauge for a linearly polarized beam propagating in the $\hat{x}$ direction is given by

$$\mathbf{A}(x, y, z, t) = U(x, y, z) \exp\left(i(kz - wt)\right)\hat{x}, \tag{1.35}$$

We can now represent the electric field ($\mathbf{E}$) and magnetic field ($\mathbf{B}$) shown in Eq.(1.34) as follows

$$\mathbf{B}(x, y, z) = \nabla \times \mathbf{A}(x, y, z) = ik \exp(i(kz - wt))(U(x, y, z))\hat{y} + (\frac{i}{k}\frac{\partial U(x.y.z)}{\partial y})\hat{y}, \tag{1.36}$$

$$\mathbf{E}(x, y, z) = \frac{ic^2}{w}\nabla \times \mathbf{B}(x, y, z) = iw \exp(i(kz - wt))(U(x, y, z))\hat{y} + (\frac{i}{k}\frac{\partial U(x.y.z)}{\partial y})\hat{y}. \tag{1.37}$$

By substituting Eq.(1.36) and (1.37), we can calculate the Poynting vector the following equations

$$\mathbf{E} = \frac{1}{2}(\mathbf{E} + \mathbf{E}^*), \tag{1.38}$$

$$\mathbf{B} = \frac{1}{2}(\mathbf{B} + \mathbf{B}^*). \tag{1.39}$$

By evaluating the Poynting vector from Eq.(1.38) and Eq.(1.39), we obtain

$$\begin{aligned}\mathbf{S} = \varepsilon c^2 \langle \mathbf{E}_{real} \times \mathbf{B}_{real} \rangle &= \frac{\varepsilon_0 c^2}{4}(\mathbf{E} \times \mathbf{B}^* + \mathbf{E}^* \times \mathbf{B}) \\ &= (\frac{\varepsilon_0 w c^2}{4}(i(U\nabla U^* - U^*)\nabla U) + 2k|U|^2\hat{z}).\end{aligned}$$

The acting Poynting vector in cylindrical coordinates along the azimuthal direction can be written as

$$\mathbf{S}_r = 0, \tag{1.40}$$

$$\mathbf{S}_0 = \frac{l w \varepsilon_0 U_0^2}{2r}, \tag{1.41}$$

$$\mathbf{S}_z = k \varepsilon_0 w U_0^2. \tag{1.42}$$

The equation of the total momentum density can be written as follows

$$L_z = \frac{1}{c^2}(r \times S)_z. \tag{1.43}$$

The total OAM density can be obtained by substituting Eq.(1.40), Eq.(1.41) and Eq.(1.42), which is expressed as follows

$$L_z = \frac{l w \varepsilon_0 U_0^2}{2c^2} \tag{1.44}$$

It can be noticed from Eq.(1.44) that OAM density is directly proportional to the topological charge l. This expression $e^{il\phi}$ introduces an azimuthal phase dependence of the beam as it propagates which is influenced by l. And results in the azimuthal rotation of the wavefronts, the number of rotations per wavefront depend on the absolute value of the l index [16].

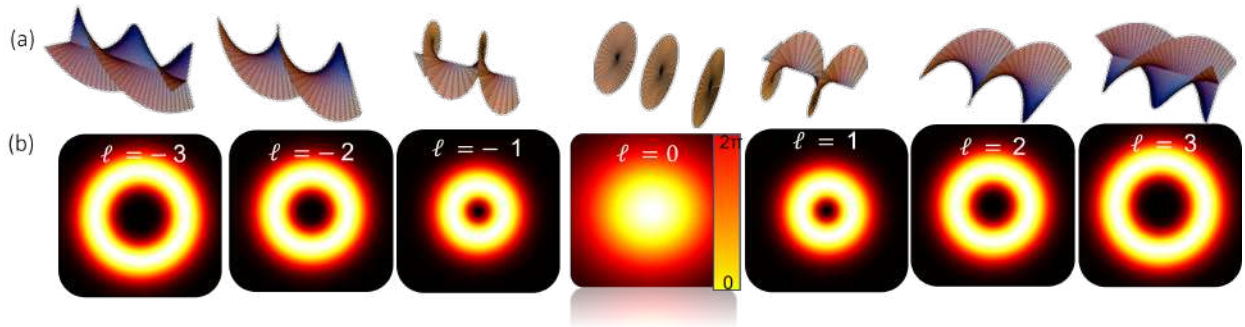

FIGURE 1.5: Illustrates (a) the 3D wavefronts and (b) the transverse intensity distribution for l = [-3,3].

This is usually referred to as helical twisting along the direction of propagation, and this twisting can be seen in fig.(1.5a). The l index affects the handedness, such that a positive l is associated with a right rotation and a negative l is associated with an left rotation. This twisted form of a wavefront is associated with OAM which is conveyed by the beam in the paraxial regime such that it possesses an OAM of $l\hbar$ per photon [13], l determines the azimuthal index of the vortex beams, the higher the l value the bigger the vortex as seen in fig.(1.5b).

1.5 Hermite Gaussian beams

HG beams have a rectangular symmetry and are usually used for modal analysis of radiation from a laser of which the laser cavity design is asymmetric in a rectangular manner. Over the past decades research has been done on both theoretical and experimental aspects of HG beams e.g Saghafi researched the characteristics of elegant and standard HG beams [20], Lu' looked at the difference between the two beams (elegant and standard HG beams) [21], the elliptic HG beams were later introduced by Cai, and they also determined the propagation of HG beams by using a misaligned optical system which involved a vector integral [22]. Hermite-Gaussian beams are solutions to the Helmholtz wave equation using the paraxial approximation and it can also be referred to as a higher order Gaussian beam mode. HG beams are mathematically presented in terms of a Gaussian function and the Hermite polynomial $H_n(x)$ as follows

$$HG_{nm}(x,y,z) = E_0 \frac{\omega_0}{\omega(z)} \exp\left(-\frac{x^2}{\omega(z)^2}\right) H_n.H_m\left(\sqrt{2}\frac{y}{\omega(z))}\right) \exp\left(-\frac{y^2}{\omega(z)^2}\right.$$
$$\left.\exp\left(i[kz - (1+n+m)\arctan\left(\frac{z}{z_R}\right) + \frac{k(x^2+y^2}{2R(z)}\right]\right.$$

Where $n, m \in \mathbf{Z}$ represents the indices of the Hermite polynomials H_n and H_m respectively, if $n = m = 0$ it can be seen from fig.(1.6) that the HG beam equations becomes the fundamental Gaussian solution. The Gouy phase in this case has changed and can be written as follows

$$\psi(z) = (N+1)arctan\left(\frac{z}{z_R}\right). \tag{1.45}$$

The total order of the mode N is represented as $N = l + m$.

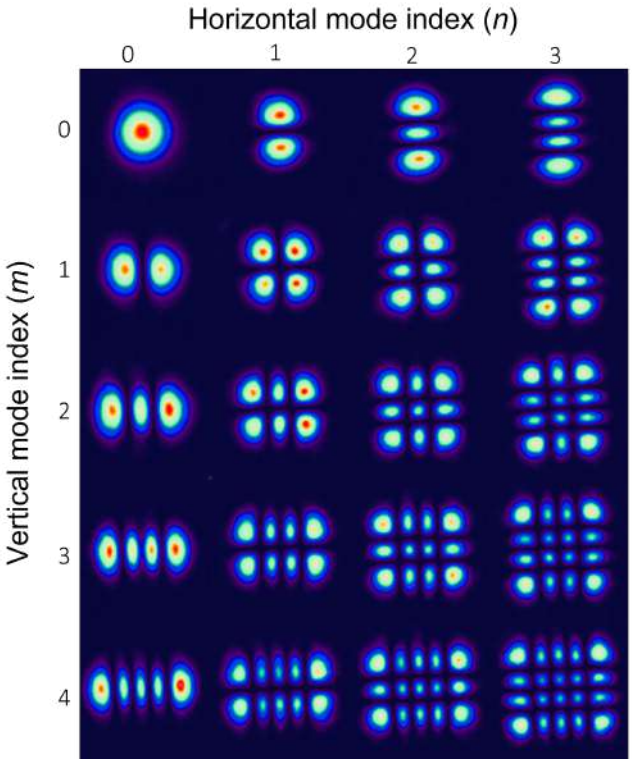

FIGURE 1.6: 2-D intensity profiles of HG beams.

The shape of the profile in the direction x and y is obtained by the indices n and m. The intensity profile of the HG beams have n nodes in the horizontal and m nodes in the vertical as shown in fig.(1.6).

1.6 Vector beams

In order to understand vector beams we first have to discuss the polarisation. A vector nature can be represented by the polarisation structure linked to the light wave. Consider any arbitrary polarisation state which relates to a light wave that can be expressed by two orthogonal and linearly polarised fields as follows [23]

$$\mathbf{E}(z,t) = E_x \cos(wt - kz + \delta_x)\mathbf{x} + E_y \cos(wt - kz + \delta_y)\mathbf{y}. \tag{1.46}$$

Where $w = 2\pi f$ represents angular frequency, the wavenumber is given by k, the corresponding phases are given by δ_x and δ_y, E_x and E_y are the amplitudes of the fields. Using Jones vector notation we can represent Eq.(1.46) as follows

$$\mathbf{E}(x,y) = \begin{bmatrix} E_x \\ E_y \end{bmatrix} = \begin{bmatrix} E_x \cos(wt - kz + \delta_x) \\ E_y \cos(wt - kz + \delta_y. \end{bmatrix} \tag{1.47}$$

In complex notation Eq.(1.48) can be written as follows

$$\mathbf{E}(x,y) = \exp i(wt - kz + \delta_x) \begin{bmatrix} E_x \\ E_y \exp(i\delta). \end{bmatrix} \tag{1.48}$$

Where δ, given by $\delta = \delta_y - \delta_x$ represents the phase difference between the E_x and E_y fields. The common phase factor can be neglected for simplicity and Eq.(1.47) becomes

$$\mathbf{E}(x,y) = \begin{bmatrix} E_x \\ E_y \exp(i\delta). \end{bmatrix} \tag{1.49}$$

Equation (1.49) represents the electromagnetic wave equation in Jones vector notation. The normalised Jones vector of the electromagnetic wave equation can be written as follows

$$\mathbf{E}(x,y) = \frac{1}{\sqrt{E_{(x,y)}^2 + E_{(x,y)}^2}} \begin{bmatrix} E_x \\ E_y \exp(i\delta). \end{bmatrix} \tag{1.50}$$

The Jones vector equation shown in Eq. (1.50) is used to represent any arbitrary polarisation state of a field, e.g a linearly polarised state can be acquired when $E_x = \cos(\theta)$, $E_y = \sin(\theta)$ and $\delta = 0$. For horizontally and vertically polarised states $\theta = 0$ or $\theta = \frac{\pi}{2}$ respectively, we can also obtain any other linear polarisation by varying θ provided that $\delta = 0$. By superimposing E_x and E_y we can obtain circular polarisation but this requires a relative phase shift of $\delta = -\frac{\pi}{2}$ or $\delta = \frac{\pi}{2}$ for the LCP and RCP respectively between the two fields. The vertical (V), horizontal (H), Right circular polarisation (RCP) and left circular polarisation (LCP) can be expressed using Jones vector notation mathematically as follows [24]

$$V = \begin{bmatrix} 0 \\ 1 \end{bmatrix}, H = \begin{bmatrix} 1 \\ 0 \end{bmatrix}, LCP = \frac{1}{\sqrt{2}} \begin{bmatrix} 0 \\ -i \end{bmatrix}, RCP = \frac{1}{\sqrt{2}} \begin{bmatrix} 0 \\ i \end{bmatrix}$$

We can expressed the diagonal (D), anti-diagonal(A) , RCP and LCP as linear combinations of the horizontal and vertical polarisation state as follows

$$A = \frac{H-V}{\sqrt{2}}, D = \frac{H+V}{\sqrt{2}}, LCP = \frac{H-iV}{\sqrt{2}}, RCP = \frac{H+iV}{\sqrt{2}}. \tag{1.51}$$

Now that we have discussed how light can have different polarisation states and how we can use the Jones vectors to describe various states of light, next we will discuss vector beams. Vector beams can be described as fully polarised beams that have locally varying polarisation states. These beams can be generated by tailoring the polarisation state of the incident field, which modulates the direction of the electric field **E**.
Taking into consideration the transverse plane given by $x - y$, we can choose the electric field **E** independently to orientate either along the x for E_x or y for E_y directions. As such we can define the polarisation state of the electromagnetic wave as polarised in the x direction for E_x and y direction for E_y. Vector beams are generated by super-positioning two fields (E_x) and (E_y) with orthogonal polarisation states x and y and each field having a unique amplitude and phase component. The coaxial superposition of the two fields amplitude will result in a transverse intensity profile given by E^2. Vector beams are characterised by inhomogeneous polarisation distribution across their spatial intensity profile.

Cylindrical vector vortex beams are the most common vector light fields and are solutions to the Helmholtz wave equation in cylindrical coordinates. Cylindrical vector vortex beams can be described as linear combination of scalar vortex beams with opposite OAM indices and orthogonal polarisation. These beams can mathematically be expressed as follows [25]

$$U(r,\theta) = A_R(r)e^{il_1\theta_1}\hat{R} + [A_L(r)e^{-il_2\theta_2}]e^{i\delta}\hat{L}. \tag{1.52}$$

Where $\hat{L}$ and $\hat{R}$ represents the left and right circular polarisation vectors, the radial profiles of the beams are represented by A_L and A_R. The OAM is given by l and θ denotes the azimuthal angle, $e^{i\delta}$, where $\delta = [0, \pi]$ introduces a new phase term. A common set of cylindrical vector vortex beams can be obtained by setting $l_1 = l_2 = \pm 1, \theta = \theta_1 = \theta_2$ and $\delta = 0$ or π as shown by the following equations

$$\begin{aligned} TM &= \tfrac{1}{\sqrt{2}}(e^{i\theta}\hat{R} + e^{-i\theta}\hat{L}), \\ TE &= \tfrac{1}{\sqrt{2}}(e^{i\theta}\hat{R} - e^{-i\theta}\hat{L}), \\ HE^e &= \tfrac{1}{\sqrt{2}}(e^{i\theta}\hat{L} + e^{-i\theta}\hat{R}), \\ HE^o &= \frac{1}{\sqrt{2}}(e^{i\theta}\hat{L} - e^{-i\theta}\hat{R}). \end{aligned} \tag{1.53}$$

Equation (1.43) describe the first low order cylindrical vector vortex beams, where TE is the transverse electric, TM is the transverse magnetic and HE is the Hybrid electromagnetic modes. Illustration of the spatial and polarisation relations of the scalar and vector beams are shown in fig.(1.7)

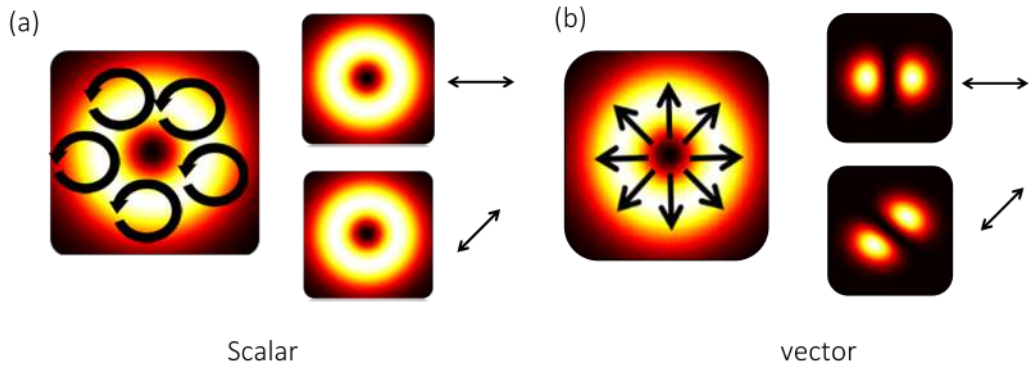

FIGURE 1.7: (a) is the example of scalar beams and (b) is the vector vortex beam profile intensities with uniform and non uniform state of polarisation, the arrows indicate the linear polariser which projects the beam into respective polarisation states which results in the intensity distribution shown on the right.

Figure.1.7(a) illustrates the scalar beam. The arrows represents the direction of the electric field oscillations around the beam profile. By putting a linear

polariser in front of the beam, it can be projected to the horizontal and vertical polarisation basis by assuming associate directions. The black arrows represents the polarization possessed by the beam. It can be observed that the spatial phase of the beam remains unchanged, which indicates the separability of the properties as well as the uniformity in the polarisation state. It is also important to note that the different polarisaton state comes as a results of the heterogeneous phase along the cross section of the beam [26]. Figure.1.7(b) illustrates the vector beams, it can be observed that the polarisation arrows on the beam profile, illustrate a clear variation in the polarisation state of the beam as the phase profile is traversed. This is observed more clearly by projecting in the horizontal and vertical basis which results in a change in the phase profile of the original beam. Even though the polarisation is limited to two orthogonal basis, the spatial mode orthogonal basis can go beyond an infinite range. Vector modes can be categorised into various orders depending on their phase profile mode order [27], the number of spatial bases increase with an increase in the order number. The spatial modes are paired with the polarisation states such the state of any vector mode is confined to a 2D combination in its simplest term [27].
The Poincaré sphere can be used to express all possible vector beams in a specific spatial mode to polarisation basis combination. Milione *et.al* [28] were the first to demonstrates the concept of the Poincaré sphere, which gave more understanding to the spatial and polarisation state of vector beams. This optical portrayal of vector beams were named high order Poincaré spheres (HOPSs). Figure 1.8 illustrates an example of HOPSs for vortex beams ($\pm l$). The states are demonstrated in Dirac notation with OAM used to illustrate the phase profile of the LG beam in order to emphasis the change and conservation of angular momentum as the sphere is traversed.

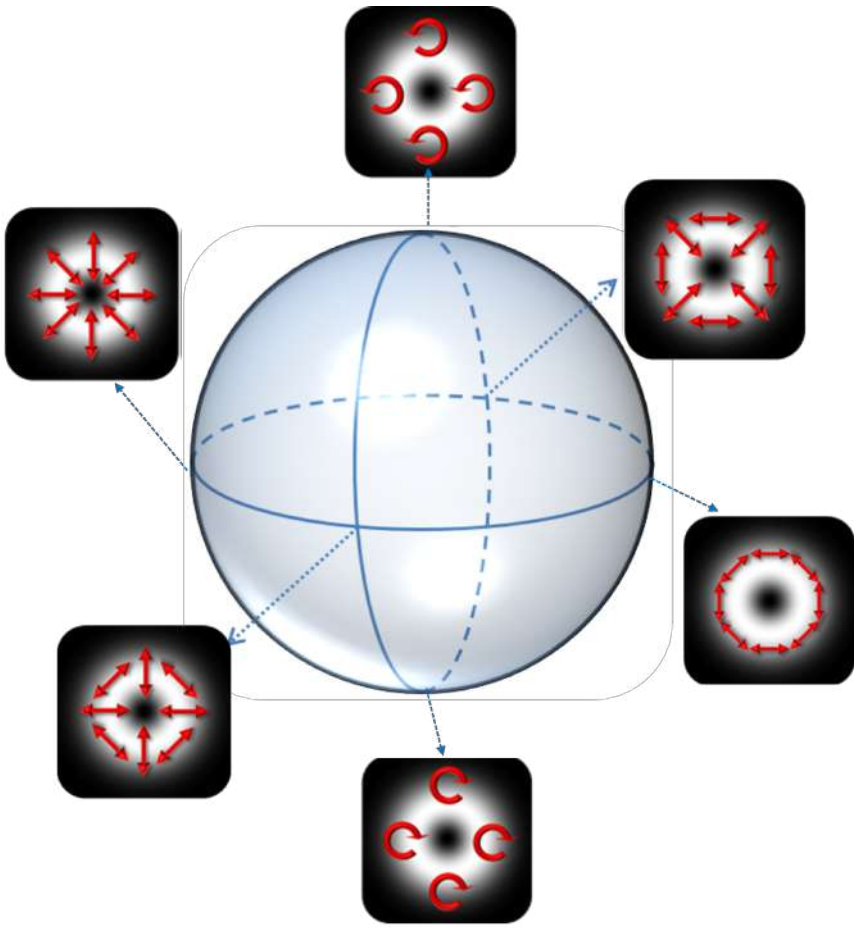

FIGURE 1.8: An illustration of a higher order Poincaré sphere for $\pm$ l where l = [-1,1].

The beams on the poles of the Poincaré sphere contain one basis pair and describe the contributing scalar beams that produce the vector beams. This is represented by the uniform circular polarisation distribution along the cross section as shown in the poles of the sphere. Any other state are non-factorizable as such regarded as vector beams. The polarisation state of the modes located at the equator is linear, this follows from the equal weighting of opposite circular polarisation. Looking in the longitudinal direction, the polarisation state has been changed from circular to elliptical polarisation. It is very important for this research to understand the properties of scalar and vector beams, in the following section we will discuss the difference between scalar and vector flattop beams.

1.7 Flattop beams

Most lasers possess the Gaussian beam intensity profile. Gaussian beams are the fundamental beam as such making them easy to manipulate during experiments for structured light. We look at how we can manipulate the fundamental Gaussian mode into a flattop beam.

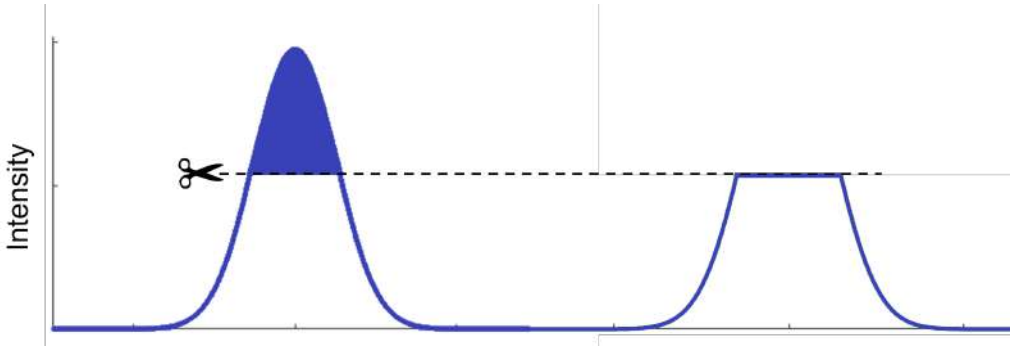

FIGURE 1.9: illustration of a Gaussian beam with a decay intensity from the center of the beam and a flattop beam with a uniform intensity profile.

Gaussian beams have a high intensity at the center of the beam and decreases gradually from its maximum on the beam axis to zero, which can be seen on fig.(1.9). On the other hand flattop beams have a uniform intensity profile with steep edges and have over the years become a topic of interest, this is because of many applications in which this profile is preferred such as for optical trapping and laser material processing [29]. Flattop beams have a continuous tunable order parameter p that can be used to transform the electric field $E(r)$ from a perfect Gaussian at $p = 2$ to a flattop at $p = \infty$ [30]

$$E(r) = \exp\left[-(\frac{r}{w})^p\right]. \tag{1.54}$$

And the intensity distribution of the flattop can be written as follows

$$I(r) = I_p \exp\left[-2(\frac{r}{w})^p\right] \tag{1.55}$$

The higher the value of p the steeper the intensity gradient and flatter the intensity at the center of the beam. From fig.(1.10) it is observable that when $p = 2$ we have a perfect Gaussian beam and when $p = 10$ we have a flattop beam.

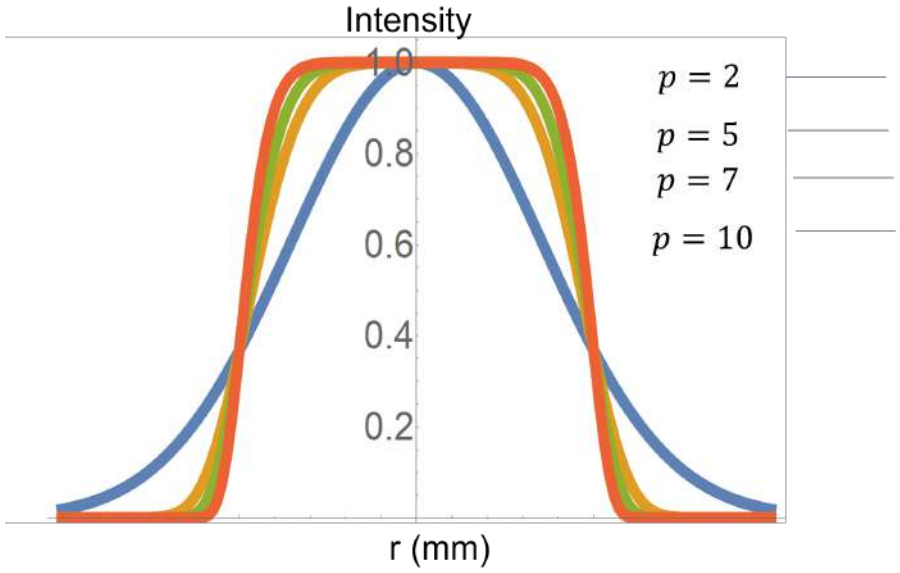

FIGURE 1.10: Illustration on how we can transform a Gaussian beam at $p = 2$ to a flattop beam at $p = 10$.

Flattop beams can be categorised into either vector flattop beams or scalar flattop beams depending on their characteristics and properties. Scalar beams are not eigenmodes of free space, as such the desired intensity profile can only be observed at the exact single plane and changes drastically during propagation as illustrated in fig.(1.11). This change in the spatial distribution of the scalar flattop makes optical delivery very difficult [31].

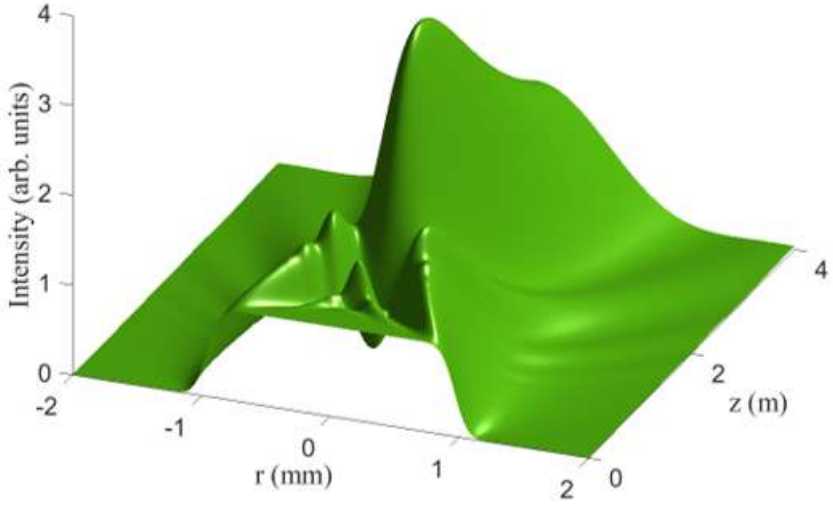

FIGURE 1.11: 3D intensity profile of a scalar beam as it propagates in the z direction over a distance of 4m.

The main focus for this research is on the vector flattop beams. The electric field of the vector flattop beam can be expressed as follows [31]

$$E(r,\phi,z) = \sqrt{1-\alpha}LG_{0,1}(r,\phi,z)\hat{e_H} + \sqrt{\alpha}LG_{0,0}(r,\phi,z)\hat{e_V}. \tag{1.56}$$

Where $\hat{e}_H$ and $\hat{e}_V$ represents the horizontal and vertical components of the Jones matrix and α represents the angle of the half-wave plate (HWP).

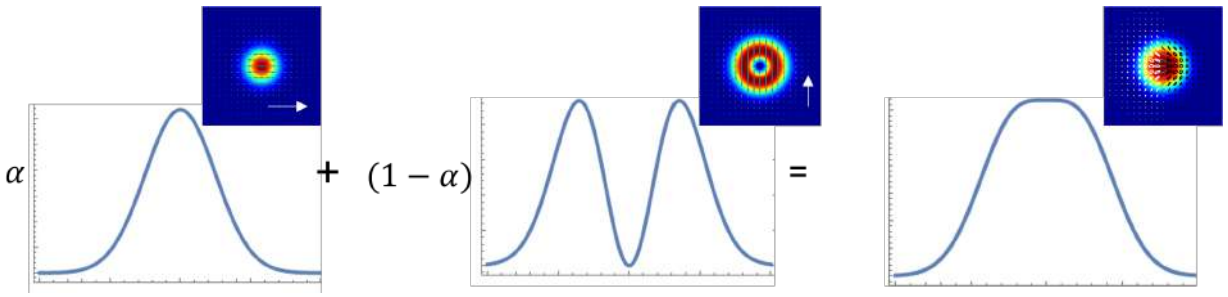

FIGURE 1.12: Intensity distribution of a LG_{00} (Gaussian), LG_{01} (vortex) and resultant flattop beam.

The intensity of vector flattop beams depends on the polarisation of the initial beam (Gaussian beam), which can easily be alter by the use of wave plates and polarisers as shown in fig. (1.12) and it can generally be written as

$$I(r,\phi,z) = \alpha|LG_{0,0}(r,\phi,z)|^2 + (1-\alpha)|LG_{0,1}(r,\phi,z)|^2 \tag{1.57}$$

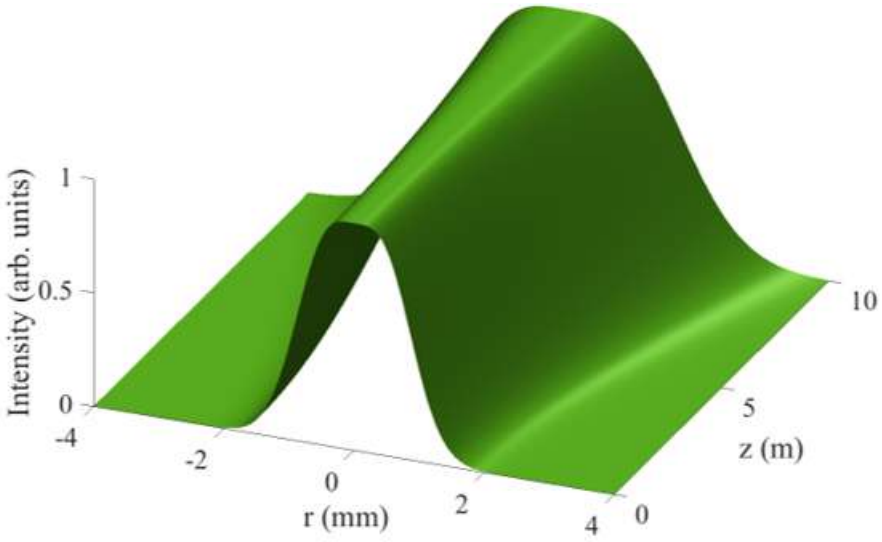

FIGURE 1.13: Propagation of a vector flattop beam over a distance of 10m.

This beam can be generated by using a SLM, whereby the polarisation dependence of the SLM can be exploited. This can be done by super-positioning a Gaussian and vortex beam (with orthogonal polarisation) and the resultant is a vector flattop beam which can be seen on fig.(1.13). By simply tuning the polarisation of the initial beam we can see an evolution from the Gaussian beam to vortex then a vector flattop (where the weighting between the Gaussian and vortex beam are nearly the same). Since the Gaussian and vortex beams are eigenmodes of free space their superposition is also an eigenmode of free space [31]. Figure 1.12 shows that vector flattop beams are invariant during propagation. In the next chapter we will discuss in detail SLMs

and how they can be used to generate different beams, and look into how to generated vector flattop beams in the laboratory.

Chapter 2

Experimental techniques

In this chapter we discuss the mechanism of Spatial Light Modulator, how to calibrate them and the importance of calibrating them for a specific wavelength. We look at the characteristics of a Digital Micro-mirror Device (DMD) and how they work. We illustrate how to generate various modes by using a SLM and calculate the correlation between the simulated and experimental modes. This is done by overlapping (cross-correlation) two modes together and a good correlation is between 60% and a 100%. Lastly we discuss Stokes polarimetry and modal decomposition techniques which will help us analyse our mode's spatial profile and polarisation content.

2.1 Spatial light modulator

2.1.1 Mechanism

A SLM is a device that uses liquid crystal molecules to alter the phase and amplitude of light by applying a controlled voltage [32]. Liquid crystals where first introduced back in 1985 as Hughes liquid crystals valve [26]. Over the years more affordable Liquid Crystal Display (LCD) technology where manufactured for the development of SLM applications such as resolution and speed [33]. This device can be used for image projection, holographic data storage , optical computing as well as for shaping ultrashort pulses [34–36]. Nematic LCDs are the most commonly used type and can be used for phase-only modulation, they are constructed as a two dimensional array of pixels, where each pixel is filled with a nematic liquid crystal material [37]. These molecules can be represented by a cigar-shaped ellipsoid which has an extraordinary refractive index donated as n_e and an ordinary refractive index as n_0 [38]. The modulation of light depends on the arrangement of the molecules on the LCD within the pixels of micro-displays, which can be classified as vertically aligned nematic (VAN), parallel aligned nematic (PAN) or the twisted nematic (TN). The type determines how the incident light beam will be modulated, it can either be phase-only, amplitude-only or both phase and amplitude modulation [39–41].

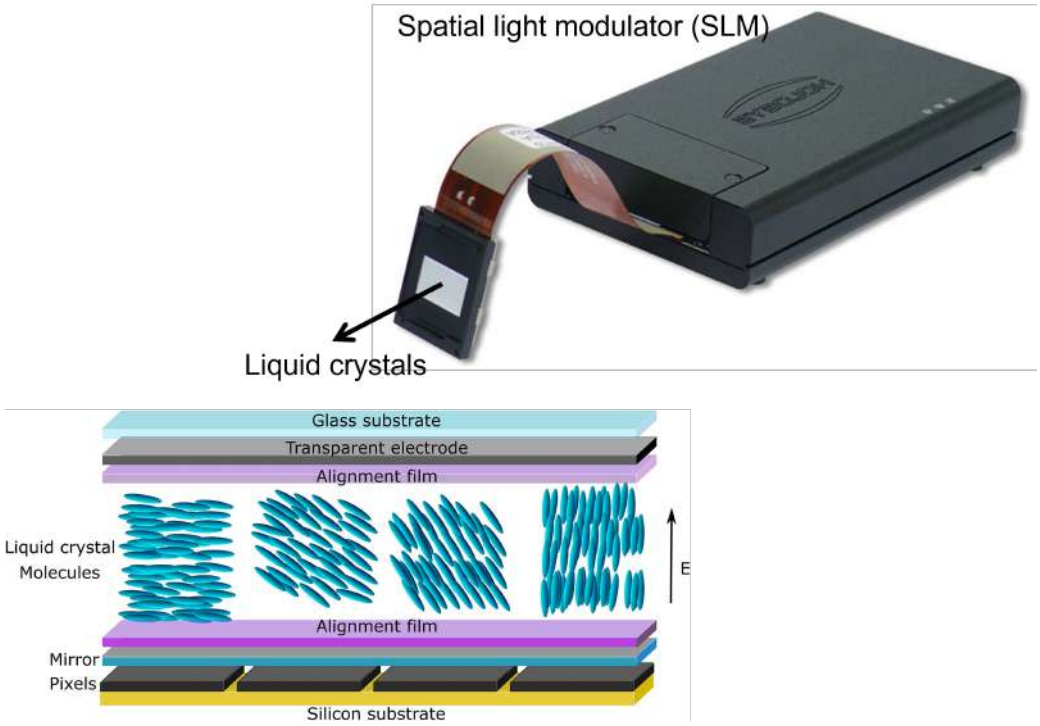

FIGURE 2.1: A conceptional cross section of a liquid crystal SLM. For an incident beam that has the polarisation e_0 and e_n a spatially varying phase delay $\theta(x, y)$ can be observed by rotating the liquid crystals on the SLM.

SLMs allows for the phase information to be encoded on the on computer controlled display. SLMs use liquid crystals (LC) an interface between the solid matter phase and the liquid to alter either the phase or amplitude of the beam, it can also be used to modulate both (phase and amplitude). The LC are sandwiched between an array of electrodes as shown in fig.(2.1). The orientation of the crystal vary depending on the voltage applied between the electrodes which enables each pixel's refractive index to be altered. The change in phase can be written as

$$\delta_d = \frac{2\pi V L}{\lambda}. \tag{2.1}$$

Where V is the applied voltage across the electrodes, L represents the depth(which is the measurements of an object from the back to the front) of each pixel and d is the thickness(which is the measure of the object in the direction perpendicular to its surface) of the pixel. Liquid Crystals are made up of elongated birefringent material which allows the modulation of horizontally polarised light (along the slow axis). The applied voltage determines the index of refraction, as such the phase retardance can be varied through controlling the voltage which allows quick variation of the phase information encoded on each pixel. In our group we use HoloEye PLUTO SLMs, which are designed to modulated only the phase of the incident light and not the amplitude, but we can manipulate them to modulate both the phase and amplitude of the

incident beam. The display screen of the SLM has 1920×1080 pixel resolution and each pixel is 8μm in size which has an 8-bit encoding capacity that is addressed with a gray scale image that ranges from black (0) to white (255) which corresponds to 0 to 2π phase shift. The gray level depends on the applied voltage as they are associated with the LC. The pixels have a refresh rate of 50 Hz.
SLMs use digital holography to modulate the intensity of the light, this can be implemented by the use of generated computer holograms. Appropriate encoding techniques which map each pixel of the SLM onto a coordinate matrix with dimensions equal to that of the SLM are used to generate digital holograms. A digital hologram is a digital display of the transmission function that acts on an incident beam. This hologram is displayed on the SLM as a gray scale level image with 256 colours from 0 which is black to white represented by 256, which relates to the phase change of the device. The SLM is made up off thousands of pixels, which diffracts the incident beam into many diffraction orders and the modulated mode is obtained from the 1st order mode . A diffraction grating such as sinusoidal or blazed grating is normally encoded with the hologram to separate the diffraction orders.
The advantage of using a SLM is that, SLMs are easy to use as the device does not require any software to function. They use high definition media interference (HDMI) cables which provide versatility and dynamic control in optical experiments. However SLMs also have some limitations which include the fact that they are polarisation sensitive (only modulate horizontally polarised light), because of this they only have one degree of freedom (phase) and require the use of optical elements such as wave plates and a polariser in a case where beams of different polarisation are required. They have very low frame rates which limits the dynamic control in optical experiments and lastly they are very expensive. The above mentioned disadvantaged can be overcame by the use of DMDs which will be discussed in detail in section 2.2. It is important to first calibrate your SLM for your wavelength in order to get the correct phase shift. In the next section we will discuss how to calibrate SLMs for use in optical experiments.

2.1.2 Calibration

It is important to calibrate the SLM in order to obtain the desired phase shift. A SLM is used as an external display which shows the gray scaled image, where the 256 shades ranges from 0 (black) to 256 (white) corresponds to the phase retardance starting from 0 to 2π. In order for this to work the applied voltages mapped to the shades should be calibrated for that specific wavelength in order to convey the correct crystal rotations, and this can be done by adjusting the applied voltages in order to get the desired phase. An easy method that can be used to achieve this in the laboratory is performed as follows. Two lenses l_1 and l_2, having focal lengths $f_1 << f_2$ are positioned a distance $f_1 + f_2$ apart from the front of the laser source (633nm HeNe laser). The light is then expanded and collimated after passing through the two lenses such that the beam waist w is very large. The laser source that

we use in the lab is usually coherent light that emits a Gaussian beam with a planar phase. The central region of the uniform intensity of this beam after expansion can be treated as a plane wave with constant amplitude, passing this beam through a mask (double pinhole) yields two identical plane waves which are illuminated on two halves of the SLM screen and reflected off. After being reflected off the SLM screen a third lens is used to spatially overlap the beams in the far field, generating an interference pattern. The objective lens is then used to expand the interference pattern and then measured using a CCD camera . One half of the screen is kept constant (either with black or white shade) and the other half is displayed with different gray shades from 0 (black) to 256 (white) and the phase retardance resulting from the default voltages can be determined using the observed fringe shift. A diagram demonstrating this process is shown in fig.(2.2). The voltage mapped to the gray shades are found in a 'gamma file' included with the SLM.

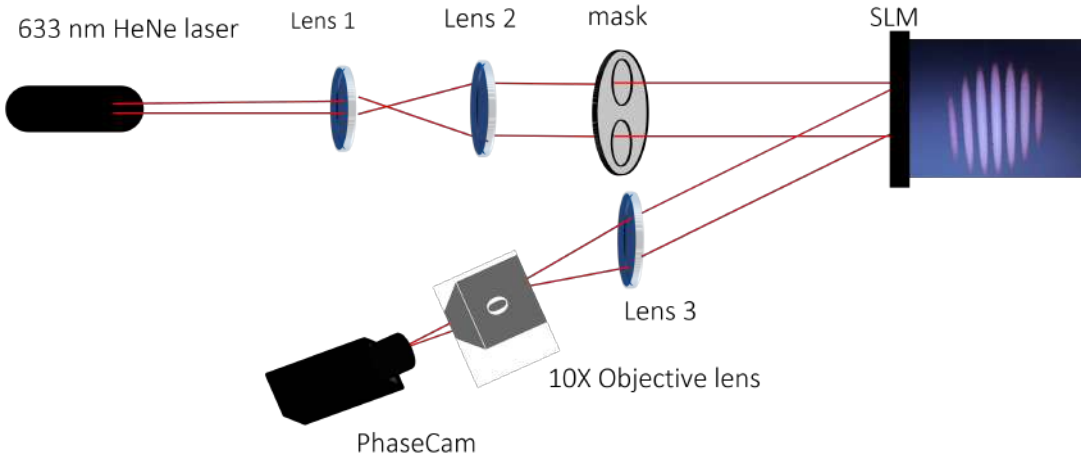

FIGURE 2.2: Schematic diagram that shows an experimental setup for calibrating a SLM.

The HoloEye SLM systems use a translucent (LCD) or reflective (LCOS) liquid crystal micro-display. HoloEye provides a calibration software called phaseCam which is an automated program that can simultaneously change the gray level scale of the hologram encoded on the SLM screen and also monitor the location of the maximum interference pattern as it shifts across the camera. This software is used to generate a 1 dimensional intensity profile of the interference pattern of each gray level as shown by fig.(2.3) below

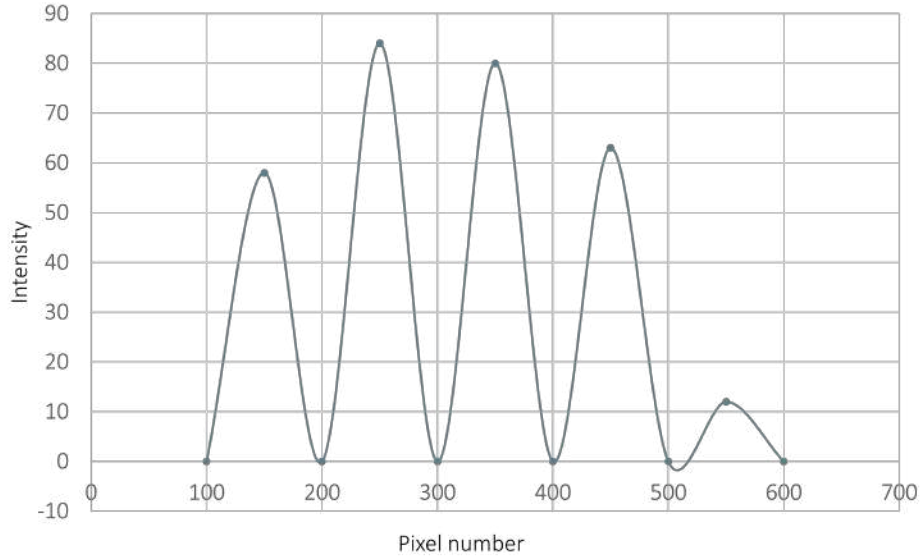

FIGURE 2.3: A plot showing the 1 dimensional intensity distribution of the interference pattern of a particular gray level.

Figure (2.3) is a graph that shows the phase shift before and after calibration. The CCD camera was used to measure the maximum phase shift of the SLM. The HoloEye calibration excel file creates a gamma file from the measured phase shift. This gamma file is a file that is loaded on the SLM and instructs the SLM to modulate the phase optimally. The SLM is said to be calibrated if it modulates from 0 gray scale level to 2π gray scale level adjusted accordingly.

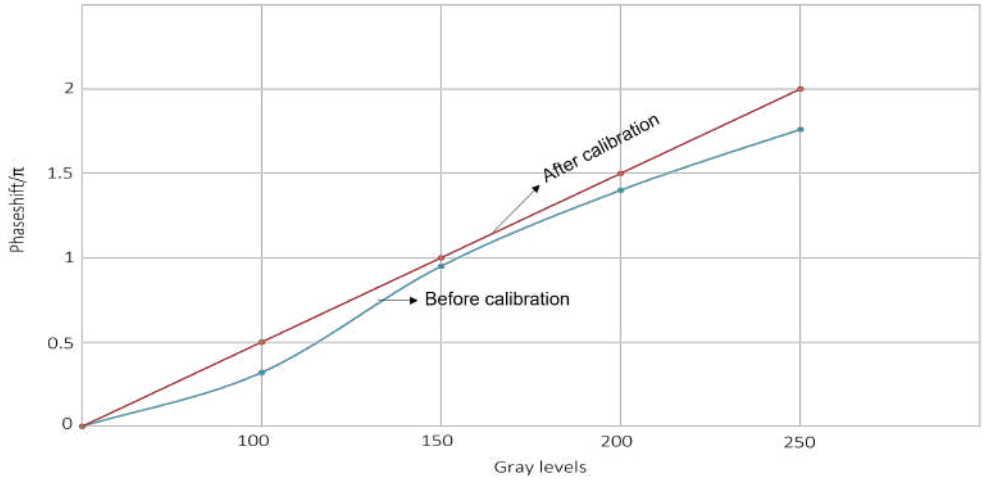

FIGURE 2.4: Plot showing the phase shift before and after calibration.

From the graph shown in fig.(2.4) we can see that before calibration that the phase shift was below 2π and the graph is not linear, after calibration with a linear graph with phase shift of 2π was obtained. Now that we have

shown how to calibrate SLM to get the desired phase shift, next we will discuss how to generate beams with SLMs.

2.2 Generation of spatial modes

2.2.1 Laguerre-Gaussian modes

SLMs can be used to generate vortex (OAM) modes by modulating the phase only, this can be done by encoding a phase-front associated with the field desired on the SLM display screen. This is associated with the following transmission function

$$T_l(\phi) = e^{il\phi}, \tag{2.2}$$

where ϕ represents the azimuthal coordinate and l denotes the topological charge of the OAM. The argument of the transmission function is encoded on the SLM display function in a form of a gray scale image. A Gaussian beam from the laser source will interact with the hologram and the wanted phase fronts will be diffracted into the first order of the output beam in order for a vortex beam to be generated. It should be noted that not all of the incident light will be modulated. The 0th order, which is the light that is unmodulated propagates on axis with the diffracted modulated first order, causing them to interfere. A periodic grating is added to separated the 0th order from the first order, in order to retrieve the modulated light. An aperture can then be used to filter out the modulated first order. Now, the transmission function is given by

$$T_l(\phi) = e^{(-il\phi + 2\pi \frac{x}{t_x})}. \tag{2.3}$$

Where t_x is the periodic grating and x is the coordinates in Cartesian form, as such the diffraction order from the SLM will be diffracted horizontally. It is important that any direction can be chosen for the grating i.e replacing x with y means that the diffraction order will be diffracted vertically. Figure. 2.5 illustrates how to generate and detect a vortex beam. As demonstrated a Gaussian beam with a plane wavefront is illuminated on an SLM screen with a computer generated hologram phase only encoded with a desired transmission function.

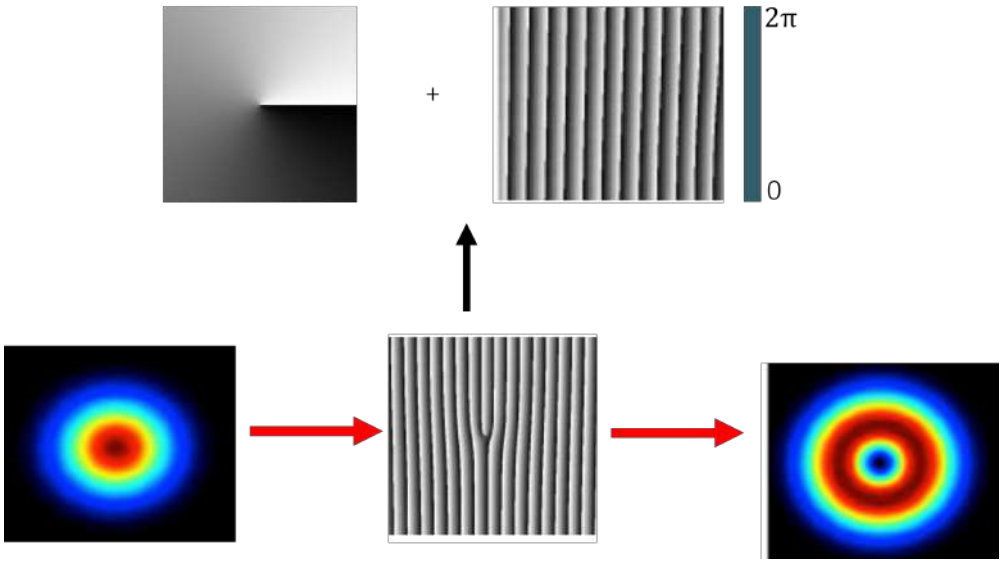

FIGURE 2.5: Mode generation and detection using digitally encoded holograms on the SLM. A Gaussian beam is illuminated on the phase-only SLM that is encoded with an azimuthal phase profile. The output is a vortex mode.

SLM can also be used to tailor both the phase and amplitude of an incident beam. One way that an SLM can tailor light is by modulating the phase of light. By changing the phase of the light waves in a controlled manner, an SLM can create interference patterns that can be used to shape the light in specific ways . This is associated with the transmission function given as follows

$$T(\phi) = \frac{A_1}{A_0} \exp\left[i(\phi_1 - \phi_0)\right]. \tag{2.4}$$

From Eq.(2.4) we notice that in order to generate a spatial mode we should have both the phase and amplitude modulation. Since we are having a phase-only SLM, we require a phase transmission function which can be written as follows

$$T(\Phi) = \exp(i\Phi_{SLM}). \tag{2.5}$$

A spatial mode can be generated by encoding a hologram with a transmission function T of amplitude 1 as shown in Eq.(2.5), which takes more light towards the zeroth order [42] and results in the creation of spatial modes. The holograms encoded on the SLM display screen with both the phase and amplitude term can be written as follows

$$\Psi_{SLM} = mod[\Phi(r,z) + 2\pi(x\frac{G_x}{\lambda f} + y\frac{G_y}{\lambda f}), 2\pi], \tag{2.6}$$

where $\Phi(r,z)$ denotes the phase of the spatial mode in the transverse orientation. A lens is placed a focal length away from the SLM display screen in order to separated the 1st order mode (desired order) from the 0th and higher order modes. $G_y = g_y\lambda f$ and $G_x = g_x\lambda f$ are the grating which is periodic along the x and y direction and are related to the grating frequency (g_y and

g_x) and are depended on the focal length of the lens used. Gratings are used to disperse desired mode into different directions, let $G_x x = 0$ $G_y y = 0$ the modes will scatter in the x- direction and vice-versa. By varying both $G_y y$ and $G_x x$ the orders will disperse diagonally. There are many types of gratings, for our research we will discuss the sinusoidal grating which is usually used in the generation of LG modes. Figure (2.6) shows a sinusoidal grating encoded on an SLM screen for beam generation

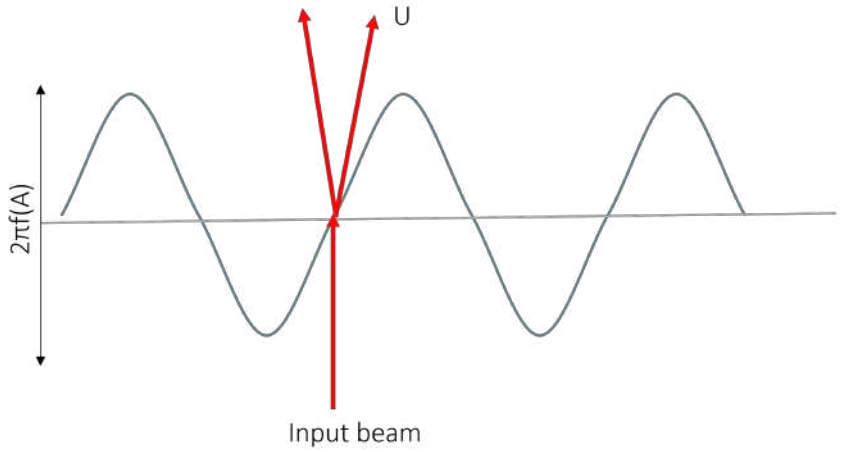

FIGURE 2.6: Encoded SLM holograms displaying a sinusoidal gratings.

The sinusoidal grating can be written as

$$\Phi = \sin(G \cdot r + \phi). \tag{2.7}$$

Where $\Phi \epsilon [-\pi, \pi]$ is chosen to be symmetrical about zero in order to remove any additional phase modulation and G denotes the grating.
Victor Arrizon and et. al. [43], published a paper in about different techniques that can be used to generate spatial LG modes using pixelated phase computer holograms. Arrizon suggested that the complex field can be written as

$$u(x, y) = A(x, y) \exp[i\phi(x, y)], \tag{2.8}$$

where $A(x, y)$ denotes the amplitude and $\phi(x, y)$ in the phase and can take intervals [0,1] and $[-\pi, \pi]$, respectively. The encoded complex field can be written in terms of the phase transmittance Computer Generated Holograms (CGH) as follows

$$T(x, y) = \exp(i\phi(A, \Phi)), \tag{2.9}$$

where CGH $\phi(A, \Phi)$ represents the function of the amplitude denoted by $A(x, y)$ and $\Phi(x, y)$ is the phase of the desired field. Equation (2.8) can be

written as a transmission function in the domain Φ transform as follows

$$U(x,y) = \sum_{q=-\infty}^{\infty} C_{A,n} \exp(iq\Phi). \tag{2.10}$$

By multiplying both side of Eq.(2.10) by $e^{in\Phi}$ and integrating from π to $-\pi$ we obtain

$$\int_{-\pi}^{\pi} T(x,y) \exp(-in\Phi) d\Phi = \sum_{q=-\infty}^{\infty} C_{A,q} \int_{-\pi}^{\pi} \exp(i(q-n)\Phi) d\Phi, \tag{2.11}$$

By using Euler's formula on the right side of Eq.(2.11) we obtain

$$\int_{-\pi}^{\pi} \exp(i(q-n)\Phi) d\Phi = \int_{-\pi}^{\pi} \cos(q-n)\Phi d\Phi + i \int_{-\pi}^{\pi} \sin(q-n)\Phi d\Phi. \tag{2.12}$$

If $q = n = 0$ and $q \neq n$ and Eq. (2.12) = 2π, we can now write Eq. (2.12) as follows

$$\int_{-\pi}^{\pi} \exp(i\phi(A,\Phi) \exp(-in\Phi) d\Phi = C_{A,n} 2\pi, \tag{2.13}$$

Where $C_{a,n}$ is the coefficient of the Fourier transform which can be expressed as follows

$$C_{A,n} = \frac{1}{\sqrt{2}} \int_{-\pi}^{\pi} \exp(i\phi(A,\Phi)) \exp(-in\Phi) d\Phi. \tag{2.14}$$

If we use the Euler's formula, Eq. (2.14) becomes

$$C_{A,n} = \frac{1}{\sqrt{2}} [\int_{\pi}^{\pi} \cos(i\phi(\Phi,A) - n\Phi) d\Phi + i \int_{-\pi}^{\pi} \sin(i\phi(\Phi,A) - n\Phi) d\Phi]. \tag{2.15}$$

It can be observed that Eq.(2.15) depends on amplitude (A), from Eq. (2.15) we can obtain the complex field by choosing the first order ($n = 1$) the complex field signal encoding condition can be satisfied when $n \geq 1$

$$C_{a,1} = na. \tag{2.16}$$

The following conditions should be met in order for Eq. (2.16) to be satisfied

$$\int_{-\pi}^{\pi} \sin(\Psi(\Phi,A) - \Phi) d\Phi = 0 \tag{2.17}$$

$$\int_{-\pi}^{\pi} \cos(\Psi(\Phi,A) - \Phi) d\Phi = 2\pi nA. \tag{2.18}$$

We can obtain suitable CGHs from Eq.(2.17) and (2.18).
Figure. 2.7 illustrates an experimental setup used to generated structured modes. An incident Gaussian beam is illuminated on the SLM screen with a digital hologram encoded, Lens-1 and Lens-2 are used to expand and collimate the incident light illuminated on the SLM display. We use lenses to separate diffraction order and image to the desired plane. Lens-3 is used to separate the diffraction orders at the Fourier plane, an aperture is used to

isolate the desired order and lens-4 is used to image the SLM screen (mode) into the camera and record the intensity profiles. Figure 2.8 shows the 2-D intensity profile of the generated and simulated LG mode with l and p indices.

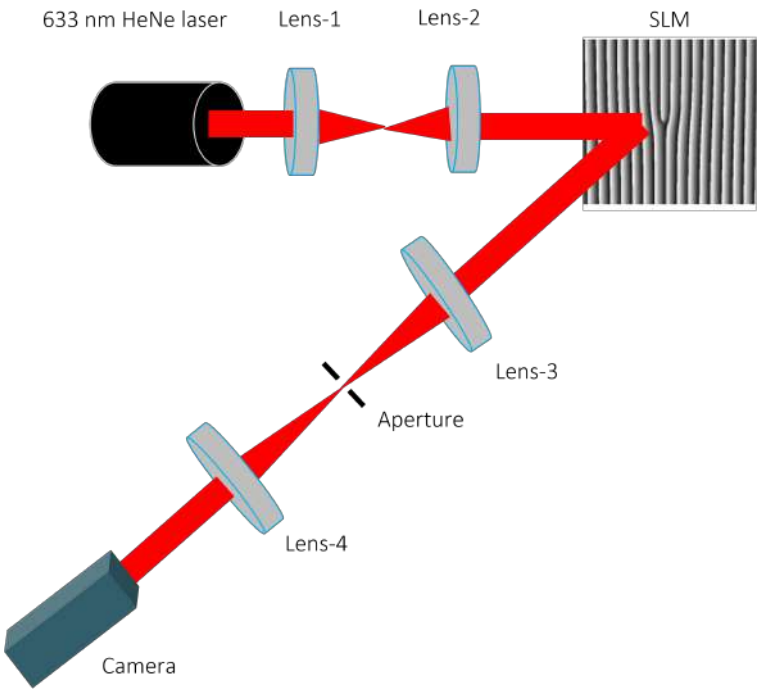

FIGURE 2.7: An experimental setup that we use to generate spatial modes. A laser (Gaussian) beam is illuminated on the SLM display screen encoded with a hologram with a transmission function given by Equ.(2.9).

Figure 2.8 shows some of the LG modes ($l = p = [0,2]$) that we generated in the laboratory and the simulated LG modes.

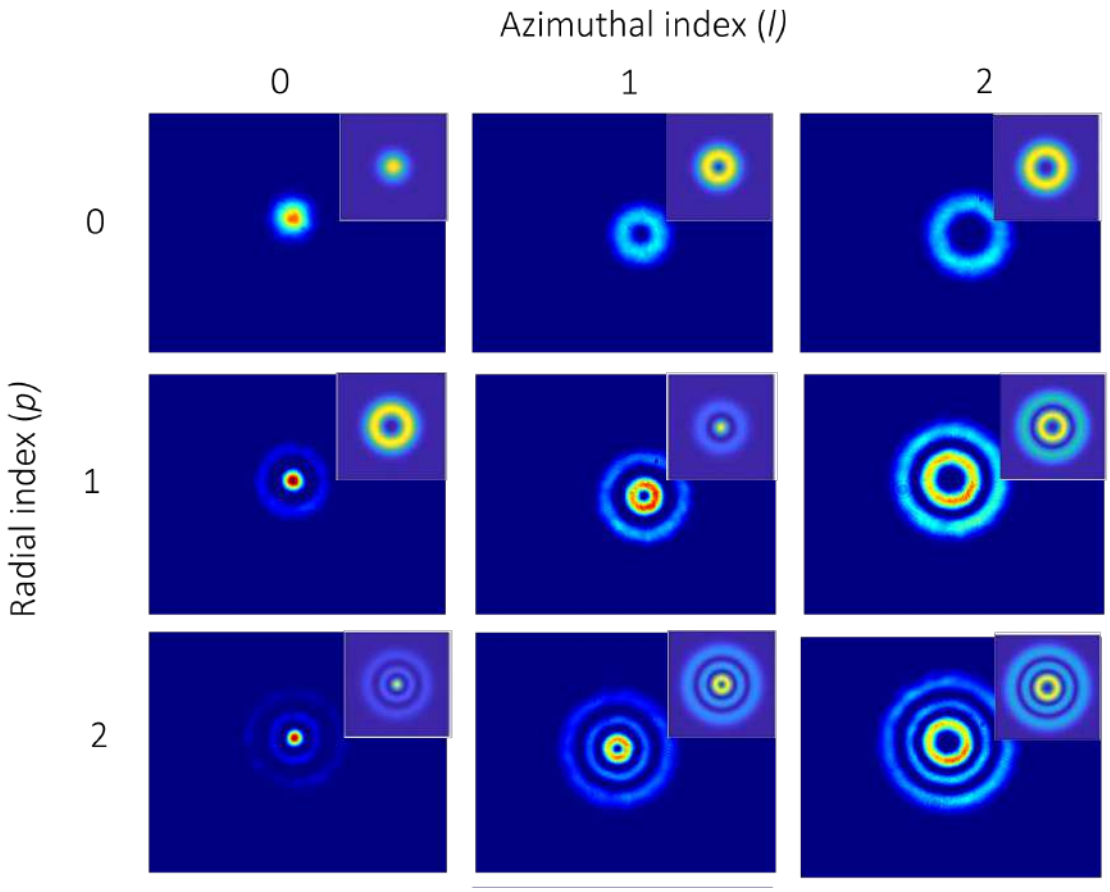

FIGURE 2.8: 2-D intensity profile of the LG modes with indices l and p. The inserted diagrams are the simulated LG beams.

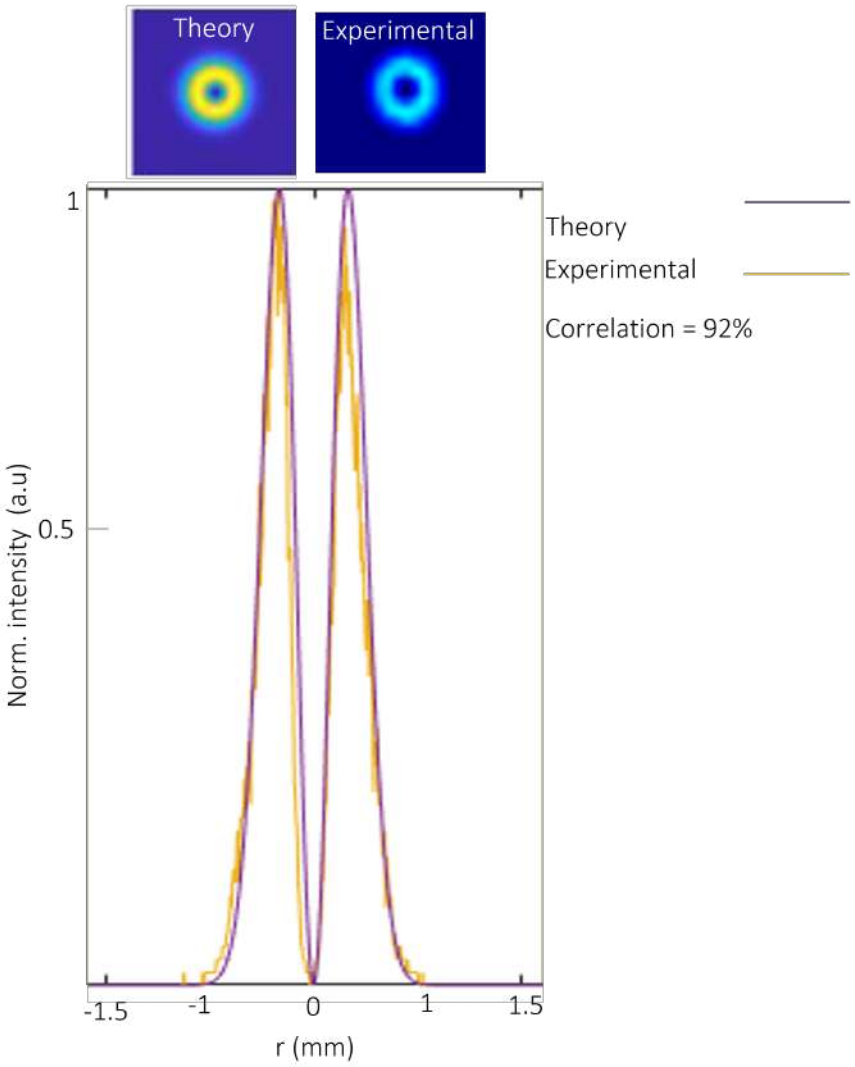

FIGURE 2.9: Graph illustrating the correlation between LG modes $(l, p) = (1, 0)$, the purple line represented the simulated LG and the oriange line represents the experimentally generated mode.

Figure 2.9 shows the calculate correlation between the the simulated and experimental LG beams, we found that the correlation is 92% which shows that the generated beams are indeed LG modes, we can conclude that the generated LG beams agree very well with the simulated LG beams. We used the least-squares method to determine the correlation between the simulated and experimental LG beams.

2.2.2 Vector flattop beams

Here we outline the concept of generating vector flattop beams, this will be done using the experimental set up shown in fig.(2.10). A Gaussian beam propagating through a half-waveplate (HWP) was illuminated on the SLM display screen. The HWP is used to control the polarisation state of the incident beam. The SLM was set to modulate horizontally polarised light when

vertically polarised was reflected off the SLM screen unmodulated. To generate the vector flattop beam a vortex phase-only hologram with azimuthal index $l = 1$ was encoded on the SLM screen, see fig.(2.10), with no gratings resulting in co-propagation between the unmodulated (Gaussian mode) and the modulated (vortex mode) being reflected off the SLM. The vector flattop is acquired by altering the polarisation state of the input beam, such that near equal weighting is obtained between the Gaussian and vortex beams.An aperture is used to filter out the unwanted order in the Fourier plan of lens-1. And lens-2 is used to image the SLM screen to the camera which records the intensities. Figure 2.11 shows the superposition of the Gaussian beam and a vortex to generate a flattop beam as we rotate the HWP, this can be achieved by rotating the angle (θ) on the HWP. If $\theta = 0$ we have a vortex, if $\theta = \frac{\pi}{2}$ we have a Gaussian and if we have an equal weighting between the two beams we have a vector flattop beam.

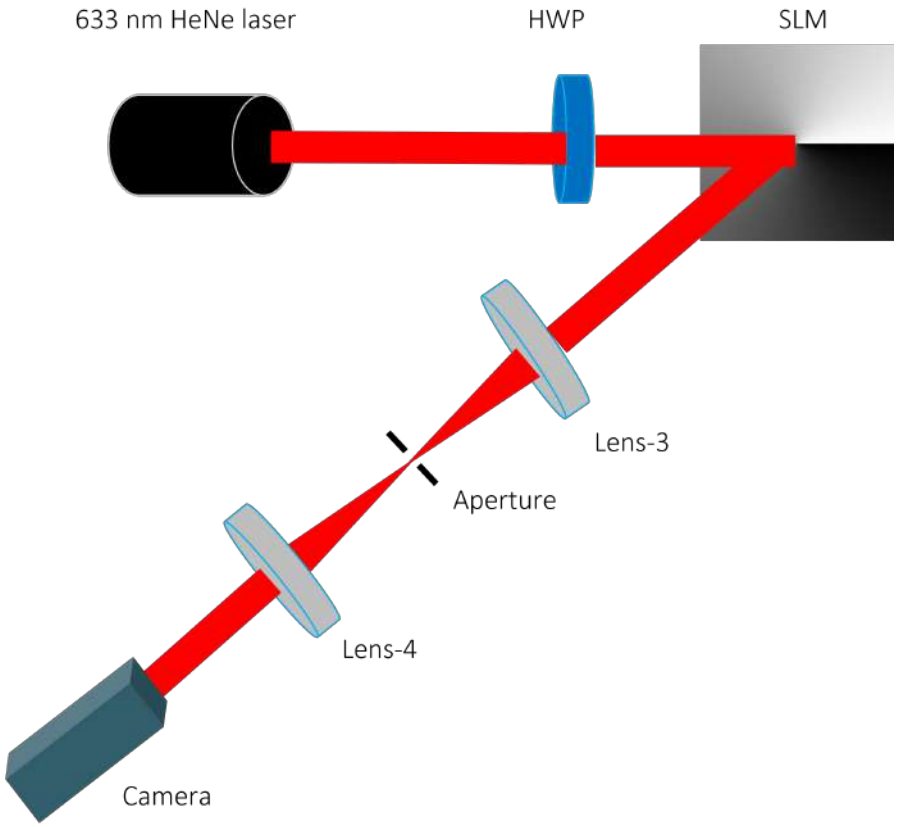

FIGURE 2.10: Experimental setup used to generate vector flattop beams.

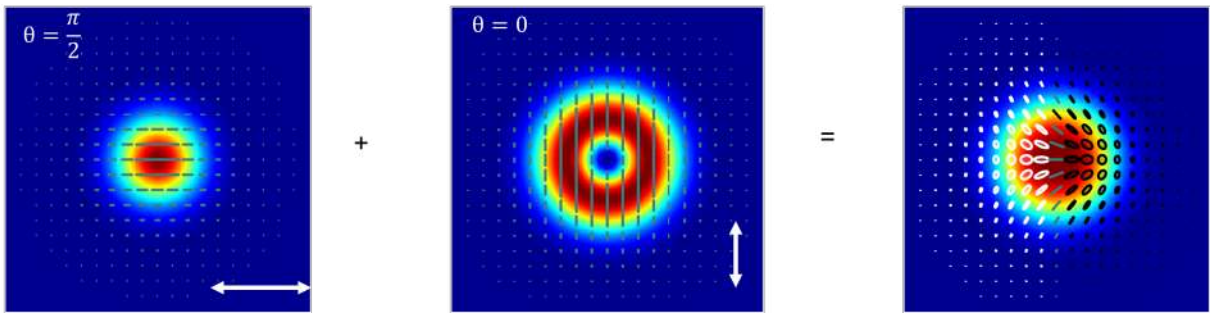

FIGURE 2.11: By rotating the angle on the HWP, we can show the evolution from a Gaussian beam, vortex beam to a vector flattop beam.

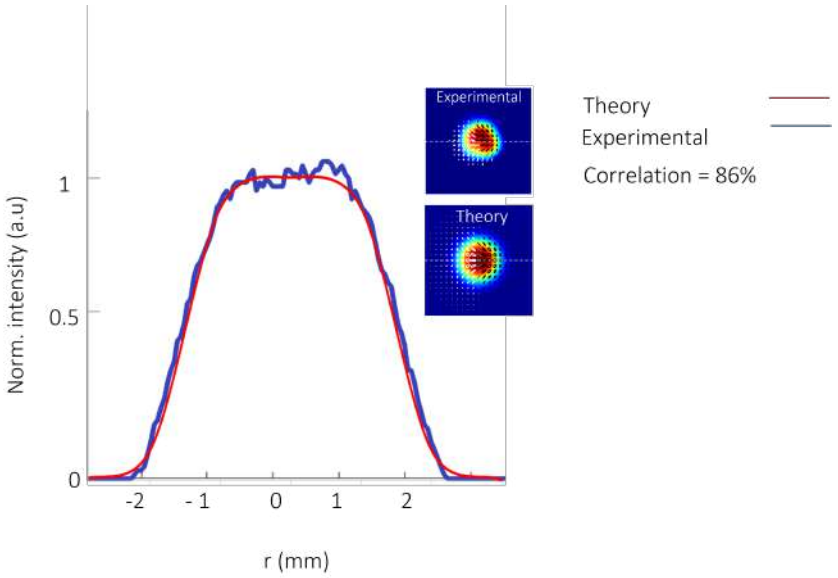

FIGURE 2.12: Illustration of 1-D intensity profile of the correlation between the simulated and experimentally generated vector flattop beams.

The correlation between the simulated and experimental vector flattop beam was calculated as shown on fig.(2.12), and we observe a 86% correlation between the two beams. Which we can conclude that our experimental results agree with the simulated.

We can also generate what we call an elongated (rectangular shaped) flattop beam. This can be achieved by superposition of a vortex with azimuthal indices l =1, l =-1 and a Gaussian beam. This beam exhibits the same properties and characteristics as the beam discussed above. Fig.(2.13) shows a 2D and a 1D intensity profile of a simulated elongated flattop beam.

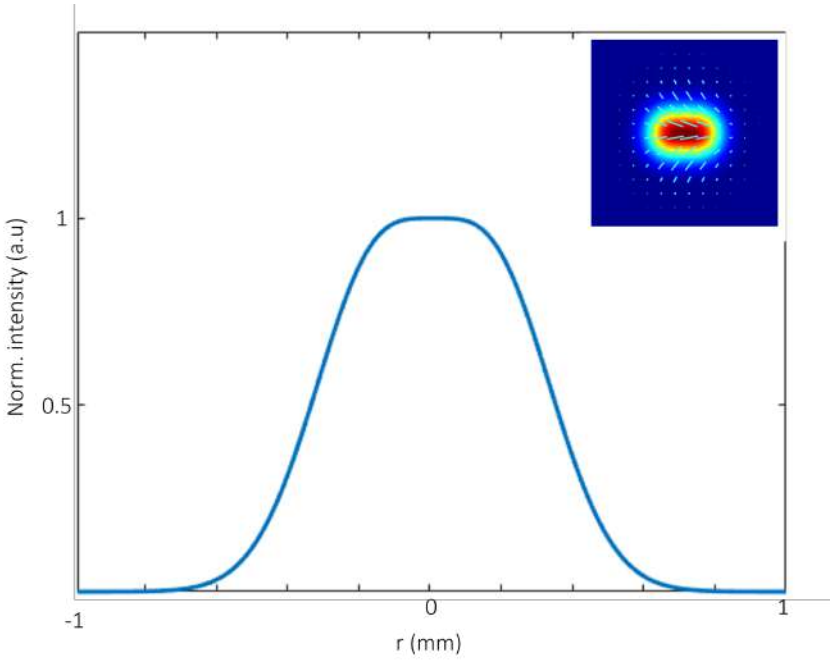

FIGURE 2.13: Schematic diagram of a simulated elongated vector flattop beam.

For this research optical fibers are used to direct beams to a point of contact. Optical fibers change both the polarisation and phase of the initial beam, this is because of modal coupling between different mode groups inside the fiber, we will only use the cylindrical shaped flattop beam as it is easier to propagate in an optical fiber.

2.3 Digital micro-mirror device

A DMD was first introduced back in 1987 as a deformable mirror device that uses a micro-mechanical analog light modulator and were first manufactured for use as a liquid crystal display alternative [44]. Over the years the device properties have improved which allowed for more suitable applications in projection. The first ever DMD to ever be manufactured was a T1 DMD2000 airline ticket printer that replaced the laser scanner with a DMD.
Fig.(2.14) shows the arrangement of the micro-mirrors in a form of arrays in a DMD [45].

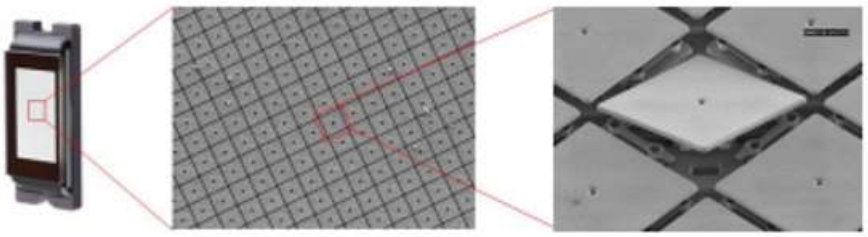

FIGURE 2.14: DMD chipset with a microscopic structure of the two dimensional array and a close-up view of the single pixel[46].

A DMD chip surface is made up of hundreds of microscopic mirrors that are arranged in a square array that corresponds to the number of pixels in the image to be displayed on the screen [47]. Fig.(2.15) shows the DMD in three different states.

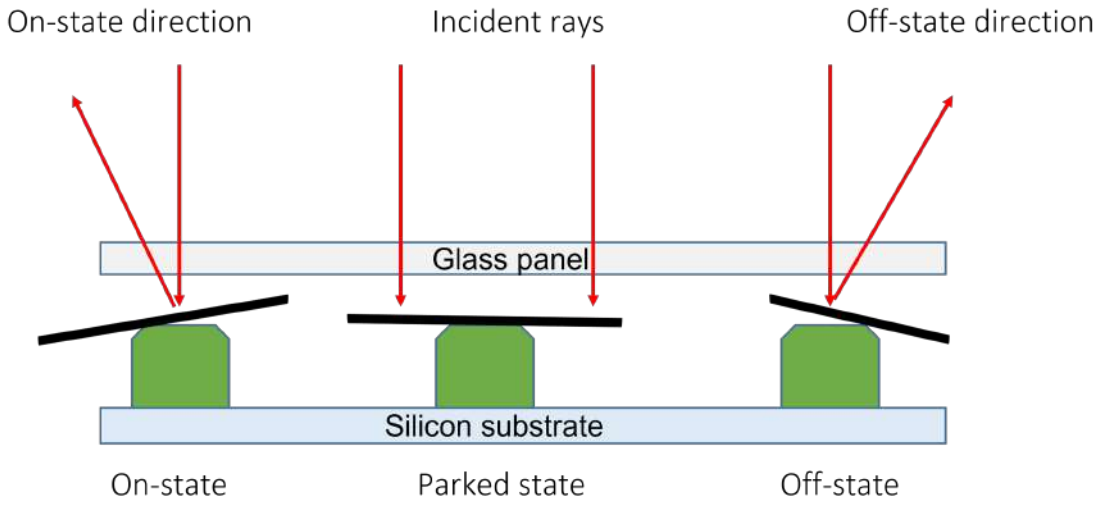

FIGURE 2.15: A schematic showing the three possible states of the DMD, on-state, parked state and the off-state.

The mirror can be titled $\pm 12^0$ to an on or off state. The on state is when the light from the incident beam (light source) is reflected to an angle of $+12^0$ into the lens making the pixels appear bright on the DMD screen, on the other hand the off state is when the incident beam is reflected at the angle -12^0 making the pixels on the DMD screen to appear darker. If the DMD is un-powered this means that the DMD is off and no hologram is encoded on the DMD screen, the pixels remain in what is called the parked state and the mirrors are not titled in either direction. In order to generate gray-scales on the DMD, the mirrors are togged on and off several times at a high speed. The ratio between the on time and off time determines the shade generated (binary pulse-width modulation).
DMDs can generate up to 1024 different shades of gray (10 bits). These mirrors are made from aluminum and are around 16 micrometers in size. The DMD is made up of two discrete mirror layouts which is the Cartesian layout

and the Diamond layout, when a hologram is encoded on the DMD screen the mirrors may only be on the off-state or the on-state. Each pixel has a dimension of 0.4um, and each mirror is attached to the yoke which is connected to two support posts by compliant torsion hinges, where the axle is fixed on both ends and twisted in the middle due to the small scale, hinge fatigue is not a problem [48]. The electrodes adjust the position of the mirrors by electrostatic attraction. Each pair of the mirror is attached to an electrode on either side of the hinge, with one of the pairs acting on the yoke and the other pair acting directly on the mirror. In most cases both sides of the mirror experience the same bias charge applied simultaneously [49]. DMDs are used to display binary holograms, these are images that consist of ones and zeros, acquired through complex amplitude modulation. The DMD has a maximum efficiency of 62% with no hologram encoded on. When a hologram with grating is encoded the DMD efficiency drops to 6.2%, the value of the grating number chosen doesn't affect the efficiency of the DMD and this is because for all the binary amplitude gratings exactly half of the mirrors will always reflect on the off-state and half will always reflect on the on-state. The grating number only affects the separation of the diffraction orders, as such the smallest number possible should be chosen for the grating to get a clear separation at the desired plane. In this work we use a DMD to detect modes for modal decomposition. The DMD is an amplitude modulating device, as such in order to control both the phase and intensity a complex amplitude modulation technique should be implemented. For modal decomposition we encode a complex conjugate of the mode present in the output field on the DMD screen then the mode is being reflected off. A lens is used to separate the orders in the far field where a camera is used to record the intensity detected. This technique will be discussed in more detail in section(2.5).

2.4 Stokes Polarimetery

The Stokes vector $\vec{S}$ is made up of four real components $\vec{S} = (S_0, S_1, S_2, S_3)$, known as Stokes parameters. Stokes parameters are used to describe the intensity and polarisation state of light. S_0 is the first Stokes parameter which is the total intensity of the field and is proportional to the optical intensity and dependents on three parameters which can be expressed in terms of the Cartesian co-ordinate points of the Poincaré sphere [50] - such that

$$S_0 = \sqrt{S_1^2 + S_2^2 + S_3^2} = E_x E_x^* + E_y E_y^* \tag{2.19}$$

$$S_1 = S_0 \cos 2\chi \cos 2\psi = E_x E_x^* - E_y E_y^* \tag{2.20}$$

$$S_2 = S_0 \cos 2\chi \sin 2\psi = E_x E_y^* + E_y E_x^* \tag{2.21}$$

$$S_3 = S_0 \sin 2\chi = i(E_x E_y^* - E_y E_x^*). \tag{2.22}$$

Where χ and ψ represents the angles which describe the ellipticity and orientation of the polarisation ellipse with respect to the $x - y$ plane as can

be seen in Fig.(2.16), and thus fully describes the polarisation state of the light [51].

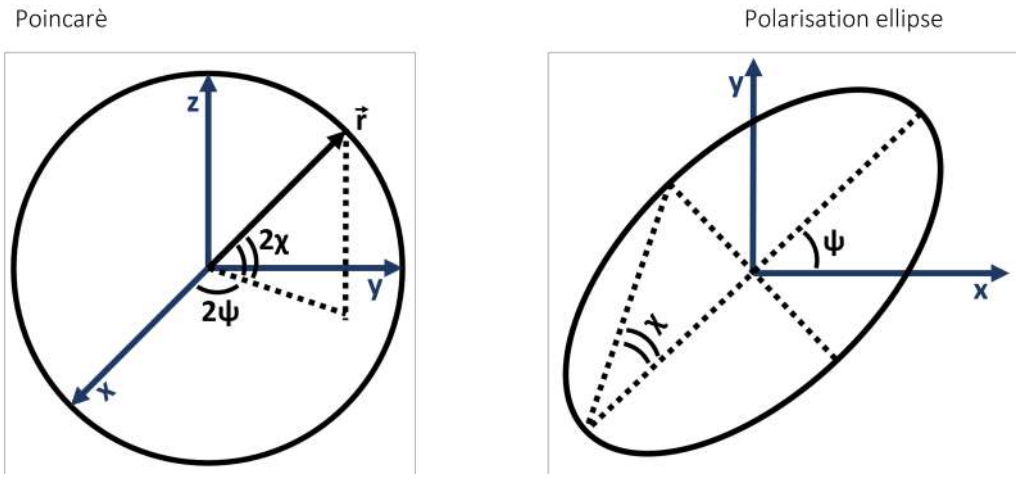

FIGURE 2.16: Diagram visualising the relationship between the polarisation ellipse and Poincaré sphere [52].

Equation (2.19) to (2.22) describes the Stokes parameters in terms of the x and y components of the electric field amplitude. It can be observed that the stokes parameters are intensity distributions which also describe the polarisation state of the field. Stokes parameters involve the use of a phase retarder which is used to change the phases of the electric field amplitudes according to the following equations [53]

$$E'_x = E_x e^{i\phi}, \tag{2.23}$$

$$E'_y = E_y e^{-i\phi}. \tag{2.24}$$

The field propagates through a polariser orientated with its transmission axis at an angle θ resulting in a total transmitted electric field amplitude of

$$E = E_x e^{i\phi} \cos\theta + E_y e^{-i\phi} \sin\theta \tag{2.25}$$

Which has an intensity denoted by $I = E \cdot E^*$, expanding out and applying appropriate *double angle* trigonometric identities together with the cosine Euler identity the expression for the transmitted intensity becomes

$$I(\theta,\phi) = \tfrac{1}{2}$$
$$[(E_x E_x^* + E_y E_y^*) + (E_x E_x^* - E_y E_y^*)\cos(2\theta) + (E_x E_y^* + E_y E_x^*)\cos(\phi)\sin(2\theta)]$$
$$\tfrac{1}{2} i (E_x E_y^* + E_y E_x^*)\sin(\phi)\sin(2\theta)$$

then, substituting the above intensity equation to Eq.(2.19) - Eq.(2.), the intensity is given by:

$$I(\theta,\phi) = [S_0 + S_1\cos 2\theta + S_2\cos\phi\sin 2\theta + S_3\sin\phi\sin 2\theta]\frac{1}{2}. \tag{2.26}$$

We can now determine for which retarding ϕ and polarisation orientation θ the observed intensity pattern $I(\theta, \phi)$ will directly give simple linear combinations of Stokes parameter pairs [53].

It can be observed that $I(\theta = \phi = 0) = \frac{1}{2}(S_0 + S_1)$, $I(\theta = \frac{\pi}{4}, \phi = 0) = \frac{1}{2}(S_0 + S_2)$, $I(\theta = \frac{\pi}{2}, \phi = 0) = \frac{1}{2}(S_0 - S_1)$ and $I(\theta = \frac{\pi}{4}, \phi = \frac{\pi}{2}) = \frac{1}{2}(S_0 + S_3)$. The experimental determination of the Stokes parameters can be obtained by acquiring these four intensity measurements and taking the following linear combinations [53]:

$$S_0 = I(\theta = \phi = 0) + I(\theta = \tfrac{\pi}{2}, \phi = 0)$$
$$S_1 = I(\theta = \phi = 0) - I(\theta = \tfrac{\pi}{2}, \phi = 0)$$

$$S_2 = 2I(\theta = \tfrac{\pi}{4}, \phi = 0) - I(\theta = \phi = 0) - I(\theta = \tfrac{\pi}{2}, \phi = 0)$$
$$S_3 = 2I(\theta = \tfrac{\pi}{4}, \phi = \tfrac{\pi}{2}) - I(\theta = \phi = 0) - I(\theta = \tfrac{\pi}{2}, \phi = 0).$$

We can note that the only required phase retardation of $\phi = \frac{\pi}{2}$ can be achieved through the implementation of a quarter waveplate (QWP) orientated with its fast axis at 45°.

The State Of Polarisation (SOP) is described by the orientation and ellipticity of the polarisation ellipse can be determined using the Stokes parameters - this can be used to reconstruct the SOP.

Figure.2.17 shows the simulated intensity measurements of a vector flattop beam and using the measure intensity measurements we can determine the Stokes Parameters

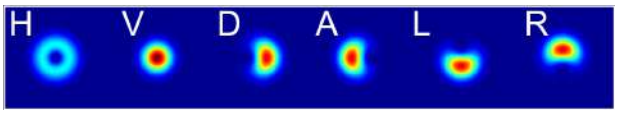

FIGURE 2.17: Intensity measurements of a vector flattop beam, from the intensity measurements we can determine the Stokes parameters.

Using the obtained intensity measurements presented in Fig.2.17, we can determine the Stokes parameters according to

$$S_0 = I_R + I_L,$$
$$S_1 = 2I_H - S_0,$$
$$S_2 = 2I_D - S_0,$$
$$S_3 = I_R - I_L.$$

Figure 2.18 shows the Stokes parameter of the vector flattop beam obtained from the intensity measurements.

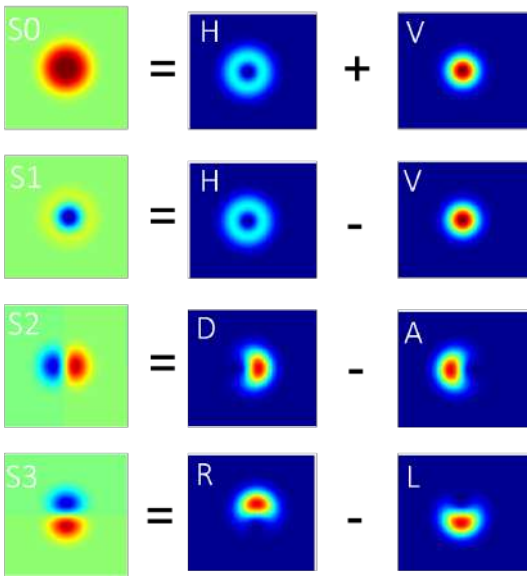

FIGURE 2.18: Stokes parameters of a vector flattop beam.

Lastly from the Stokes parameters we can reconstruct the polarisation state of the field. The Stokes Polarimetry can be calculated from the intensity measurements by using the following equation $\sqrt{\frac{S_1^2+S_2^2}{S_0^2+S_1^2+S_2^2}}$. Figure (2.19) shows the polarisation state of the vector flattop beam.

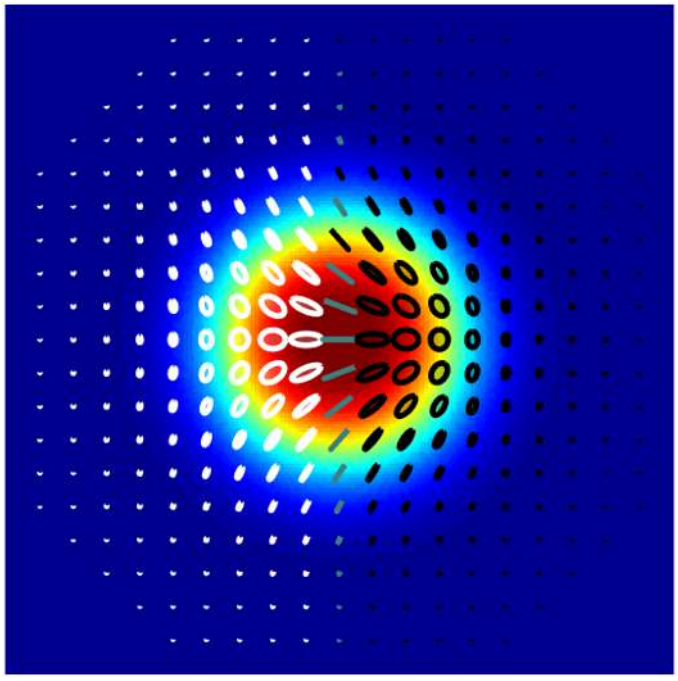

FIGURE 2.19: Reconstructed polarisation state of a vector flattop beam.

Fig.(2.20) shows an experimental setup that illustrates how to determine the Stokes parameters in the laboratory [50].

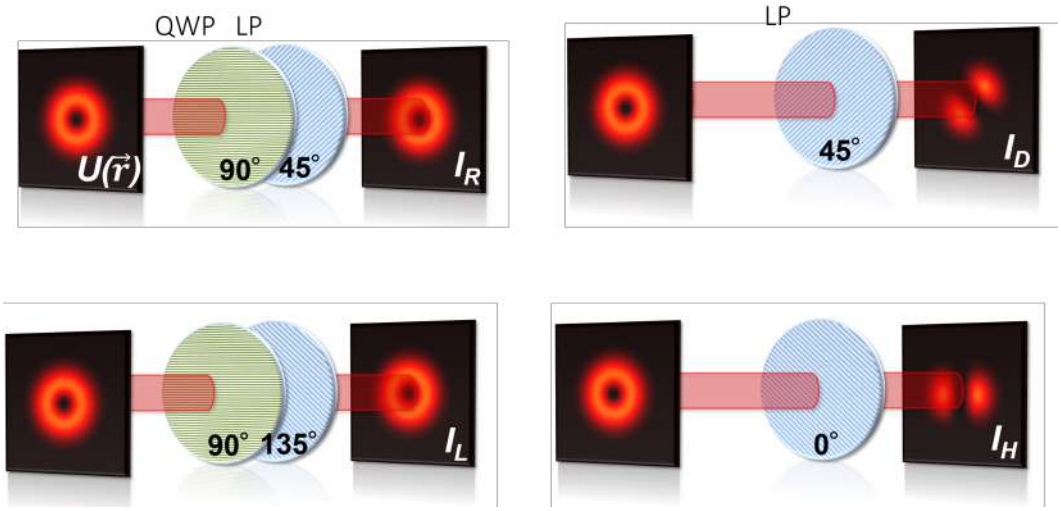

FIGURE 2.20: Experimental setup used to determine the Stokes parameters. A 633 nm HeNe laser was passed through a HWP, a diagonally polarised beam was illuminated on the SLM display encoded with a phase-only vortex to generate a vector flattop beam. A QWP and linear polariser (LP) were then orientated at various angles to acquire four intensity measurements, of polarised components, which can be used to obtain the Stokes parameters.

A QWP and linear polariser (LP) are orientated at different angles to obtain four intensity measurements, of polarised components, which can be used to acquire the Stokes parameters. Table 2.1 below shows the orientation of the QWP and linear polariser transmission axis used to acquire the intensity measurements.

TABLE 2.1: Table showing the orientation of the QWP fast axis and LP transmission axis used to obtain intensity measurements required.

QWP	LP	Intensity Component
-	90°	Horizontal (I_H)
-	45°	Diagonal (I_D)
0°	45°	Right (I_R)
45°	90°	Left (I_L)

It can be noted that for the I_H and I_D measurements the QWP was removed from the system. In this research we use Stoke polarimetry to determine how the polarisation state of the vector flattop beam varies before and after propagating through an optical fiber. In the next chapter we discuss the various types of fiber and how light propagates through fibers.

2.5 Modal decomposition

Modal decomposition also referred to as modal analysis can be defined as a technique used to decompose a complex waveform or system into its constituent modes or eigenfunctions. Modal decomposition is commonly applied in different field such as acoustics, vibration analysis, optics, and quantum mechanics. This techniques allows for a better understanding and characterisation of the complex waveform's behaviour by isolating the individual modes and their contribution [54].
The main purpose of modal decomposition is to determine the modal parameters of a system, such as the natural frequencies, mode structure and the modal damping ratios. The natural frequencies refers to the frequencies at which the system tends to vibrate when excited, mode structure represents the spatial distribution of deformation associated with the natural frequency [55]. Modal decomposition involves conducting the experimental tests or performing numerical simulations to measure the dynamic response of the system. This response data is then used to extract the modal parameters through various mathematical techniques such as the Fourier transform, singular value decomposition, or eigenvalue analysis [55].

Modal decomposition can be used in different fields such as civil engineering, aerospace engineering, mechanical engineering, architectural design and optics. The modal decomposition technique can be used for several applications to access the dynamic behaviour of structures, identify potential resonance issues, optimize structural design, and aid in the development of vibration control strategies [56]

Modal decomposition is a technique used to determine the modal content (with respect to the phase and amplitude) of the mode. If the modal content of a particular mode that is being analysed is known, then it is easier to determine the properties such as phase, intensity, beam quality and OAM density of the unknown field [54, 57, 58]. The main purpose of modal decomposition depends on the fact that structured modes are orthogonal and they span the infinite dimensional Hilbert space. As such any optical field can be decomposed into a superposition of basis functions [59] each with a complex weighting. The optical field can mathematically be written as follows

$$U(x,y) = \sum_{n=1}^{n_{max}} c_n \psi_n(x,y), \tag{2.27}$$

where n is the number of modes needed to decompose the optical field $U(x,y)$, ψ_n is the spatial mode which satisfies the orthogonality property according to the following equation

$$\langle \psi_n | \psi_m \rangle = \int\int dA \psi_n^* \psi_m = \delta_{nm}. \tag{2.28}$$

Where c_n is the expansion coefficient and can be expressed as follows

$$c_n = p_n \exp\left(i \triangle \phi_n\right) = \langle \psi_n | U \rangle. \tag{2.29}$$

Where p_n is the amplitude of the nth mode and $\triangle\phi_n$ is the intermodal phase difference. The main task of the modal decomposition techniques is to determine the expansion coefficient denoted by c_n. The phase profile and intensity of the optical field can be determined using the following expressions

$$I(x,y) = |U(x,y)|^2, \tag{2.30}$$

and the phase profile is given by

$$\Phi(x,y) = arg(U(x,y)). \tag{2.31}$$

Experimentally modal decomposition can be performed by illuminating an optical field $U(x,y)$ on a DMD screen encoded with a detecting hologram with transmission function $T(x,y) = \psi_n^*(x,y)$, where ψ^* is the complex conjugate of the optical field. The first diffraction order refracted from the DMD is given by

$$U_1(x,y) = \psi_1(x,y)U(x,y). \tag{2.32}$$

Where ψ_1 is the hologram of the spatial mode encoded on the DMD. A lens is then placed a focal length away from the DMD, Fourier transforming the DMD screen. Then the Fourier transform of the field is expressed as follows

$$F(k_x,k_y) = \int\int dAT_m(x,y)U(x,y)\exp{(ik_x + ik_y)}. \tag{2.33}$$

If $k_x = k_y = 0$ it means we are detecting on-axis. Figure (2.21) shows an experimental setup used to detect spatial modes in the Fourier plane, with a camera used to recorded the intensity profile. A single pixel corresponding to $k_x = k_y = 0$ is chosen for signal detection. Which corresponds to the mode weighting written as follows

$$|c_n|^2 = F(0,0)^2 = |\int\int dA\psi_n(x,y)U(x,y)|^2 = |\langle\psi_n|U\rangle|^2. \tag{2.34}$$

This technique can be used to determine the modal content of any optical field. For this research we want to determine how the modal content of a vector flattop beam varies before and after propagating through a fiber. Figure 2.21 shows the experimental setup used to detect the spatial content of the vector flattop beam before and after propagating through an optical fiber. The plane of the SLM is imaged into the plane of the DMD. We encode a match filter on the DMD to decompose the incident beam. A lens (lens-3) is used to Fourier transform the DMD screen and separate the diffraction order. A match filter is encoded on the DMD screen which corresponds to the complex conjugate of the input beam. when the match filter matches with the input mode a signal is detected. When the match filter doesn't match the input beam no signal is detected as such we get null.

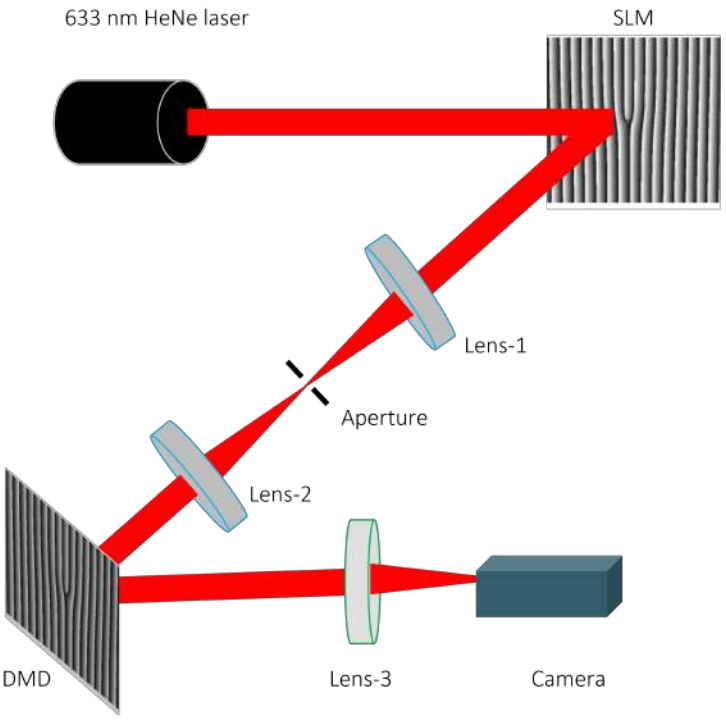

FIGURE 2.21: Experimental setup used to generate and detect spatial modes.

In the next chapter, we discuss the different fibers and their properties. We discuss how modes propagate through a fiber and investigate how an optical fiber can change the modal content and polarisation state of an input beam by making use of the modal decomposition and Stokes polarimetry techniques.

Chapter 3

Flattop Beam Propagation In Optical Fiber

In this chapter we discuss how light travels through a fiber under a phenomenon known as total internal reflection. We also look at the different types of fibers and their parameters. We calculate the number of modes our fiber can support as this is crucial for our experiment, the fewer modes propagating through the fiber the better as this reduces cross talk between modes in the fiber. We measure the Stokes parameters and perform a modal analysis of the vector flattop before the fiber and after the fiber and compare how the mode changes as it propagates through the fiber. We lastly, look at how different modes couple inside the fiber.

3.1 Fibers

Daniel Colladon and Jacques Babinet were the first to demonstrate the idea of guiding light through refraction in Paris in the 1840s. Twelve years later John Tyndall incorporated a demonstration of it in his public lecture in London. Tyndall also published a book about the total internal reflection in 1870 [60]. Optical fibers are cylindrical dielectric wave-guides and their main function is to guide light (light injected in one end of the fiber should stay in the fiber meaning it must be prevented from escaping the fiber through the surface), fibers can also be used to transport optical energy and information [61]. Optical fibers can be made up of glass (silica), plastic or copper wires with a diameter a bit thicker than the human hair [62]. Optical fibers have many applications such as fiber optical communication, where fibers are used to transmit information over long distances at low data transfer rates (at higher bandwidths) than electric cables. Fibers have the following advantages as compared to the metal wire cables: signals propagate through with minimal loss and fibers are immune to electromagnetic interference [63]. Fibers can also be used for imaging and illumination [64], fiber optic sensors and fiber lasers [65]. Optical fibers are made up of 3 main components as shown in fig. (3.1), the core (light is being retained inside the core by total internal reflection), a transparent cladding with a refractive index a bit lower (by $\approx 1\%$) and a protective coating layer which is used to eliminate cross talk between adjacent fibers and protects the core from micro-bending which can occur when the fiber is pressed to rough surfaces.

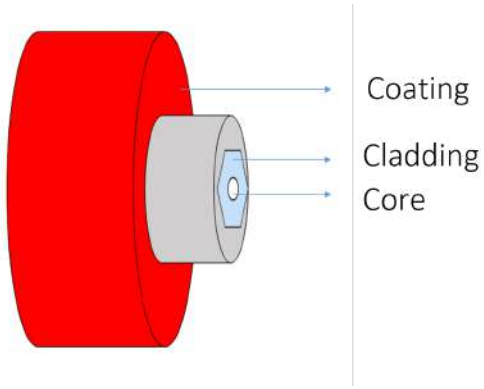

FIGURE 3.1: Diagram of an optical fiber. The core is used to guide light through total internal reflection, the cladding has a lower refractive index as compared to that of the core and the coating is the outer layer that is used to protect the core of the fiber.

Light propagating through at one end of the fiber undergoes total internal reflection and emerges at the other end of the fiber and this is shown in fig.(3.2)

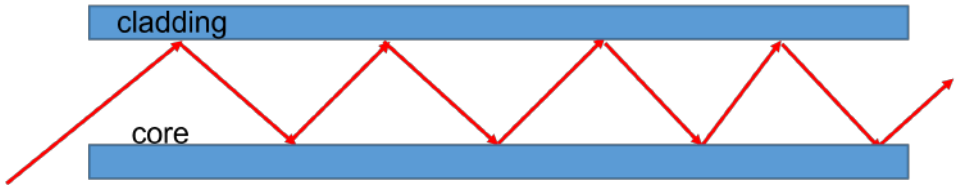

FIGURE 3.2: The total internal reflection phenomenon is used to propagate light in a homogeneous optical fiber.

Light refracts towards the normal as it enters inside the fiber, when the light propagates outside the fiber the incident angle is now less than the critical angle as such light refracts away from the fiber core into the environment. In physics, total internal reflection is defined as when light undergoes a complete reflection at the interference between two mediums with different reflective indices [66–68]. The angle of refraction at the interface of the two materials can be expressed using Snell's equation [69] as follows

$$n_1 \sin(\theta_1) = n_2 \sin(\theta_2). \tag{3.1}$$

The critical angle Q_c where $n_1 > n_2$ which is between two material boundaries can be written as follows

$$Q_c = \arcsin\left(\frac{n_2}{n_1}\right). \tag{3.2}$$

The following conditions need to be achieved in order for total internal reflection to take place, firstly the incident angle should be greater than the critical angle $Q > Q_c$. The reflected light does not exists as such the light is

totally reflected back into the first medium and secondly the refractive index of the first medium should be greater than the second medium $n_1 > n_2$.

3.1.1 Types of fibers

Fibers can be classified into two categories based on the number of modes they can support.

Single mode fibers

Elias Snitzer published a comprehensive theory about single mode fibers in the Journal of the Optical Society of America in 1962 [70]. Robert Maurer, Donald Keck *et.al*. [71] years later used fused silica (because of its high melting point and low refractive index) to manufacture a single mode fiber. They produced circular preforms by putting a purified material from the vapor phase and adding measured amounts of dopants carefully so that the refractive index of the core is a bit higher than that of the cladding, without affecting the attenuation [71]. In September 1970 they managed to produced a single mode fiber with attenuation of below 20 dB/km for a laser with wavelength 633 nm. A single mode fiber can also be referred to as a fundamental fiber or mono-mode fiber, this is because it has a small core diameter (between 8-10.5um) and it only supports the fundamental Gaussian mode. These fibers can be used to transmit information over long distances because of the following advantages, no degradation of signal during propagation and low dispersion. Figure 3.3 illustrates how light propagates in a single mode fiber.

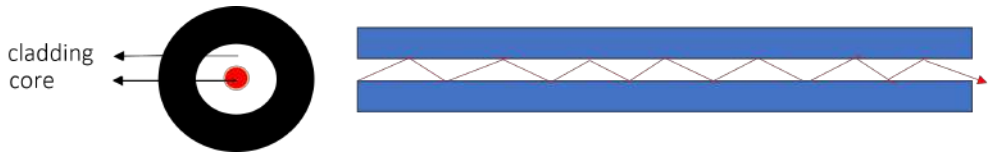

FIGURE 3.3: Diagram of a single mode (uni-mode) fiber, the line represents the Gaussian mode as it propagates through the fiber.

Multimode fibers

Multimode fibers are mostly used to transfer communication signals over a short distance i.e such as between buildings or around campus, they can also be used for imaging because the transmission of image information requires the use of devices that can support multiple spatial modes. Multimode fibers have larger core diameter (62.5 or 50 um), which enables them to propagate multiple modes at the same time [61]. Due to their large core diameter multimode fibers have limited maximum length of transmission because of intermodal coupling between the modes as they propagate through the fiber [72]. Multimode fiber can be classified into two categories depending on their refractive index profile. Figure 3.4 illustrates how different modes propagate through a multimode fiber.

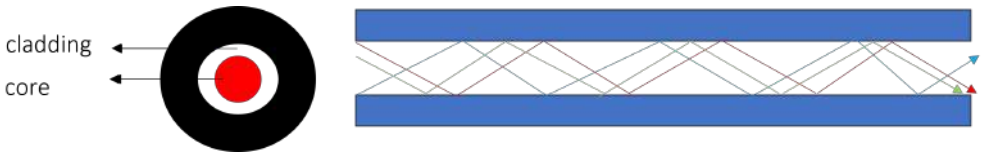

FIGURE 3.4: Diagram of a multimode fiber, because of its big core size this fiber can support more than one mode as illustrated by the different lines.

These modes are approximated by the linearly polarised (LP) modes, where l is the azimuthal index. Figure 3.5 shows the first six guided modes of the set $LP_{l,p}$.

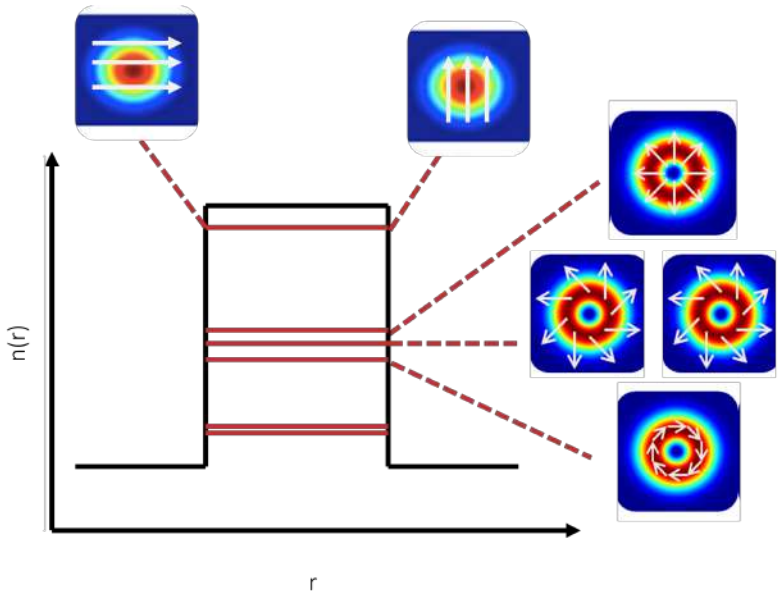

FIGURE 3.5: Illustration of the first 6 $LP_{l,1}$ modes guided through multimode optical fiber, r represents the core radius of the optical fiber and $n(r)$ is the refractive index of the fiber.

Step index fibers

A step index fiber has a core characterised by a uniform refractive index and it is slightly higher than that of the cladding, the refractive index decreases at the cladding-core interference as shown in fig.(3.6). The change in the refractive index of a step index fiber can be expressed as follows

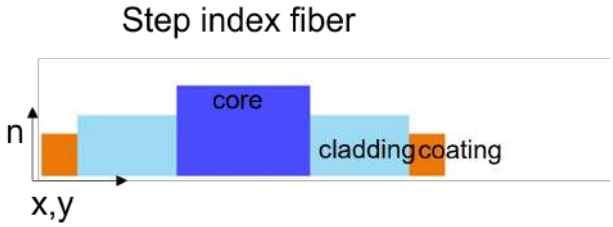

FIGURE 3.6: Diagram of a step index fiber. The core possesses a high but uniform refractive index as compared to the cladding.

$$\triangle = \frac{n_1 - n_2}{n_1} << 1. \tag{3.3}$$

Where n_1 is the refractive index of the core which is usually between 1.44 and 1.46 and n_2 is the refractive index of the cladding. The solution of the paraxial wave equation in fibers differs depending on the refractive index of the core [73]. Step index fibers are the most commonly known types of fibers. For a step index fiber, The Helmholtz solution can be expressed as follows

$$(\nabla^2 + n^2k^2 - \beta^2)\mathbf{E}(r,\phi) = 0, \tag{3.4}$$

two sets of solutions are obtained for the reduced wave equation, for the first group of modes $\beta > k_0 n_2$ which these modes are core modes and propagate at the core/cladding interface; for the second group of modes $\beta < k_0 n_2$, β represents the different modes in the fiber. Which these modes are cladding modes and propagate at the cladding/air interface.

can be approximated by the (LP) modes shown in fig.(3.5) and the optical field is given by

$$\mathbf{E}(l,p) = R_{l,p}(r)\Phi_l(\phi), \tag{3.5}$$

where

$$\begin{aligned} R_{l,p}(r) &= J_{|l|}(\tfrac{ur}{a})/J_l(u) \text{ for } r < a \\ &= K_{|l|}(\tfrac{wr}{a})/K_{|l|}(w) \text{ for } r \geq a \end{aligned}$$

and

$$\begin{aligned} \Phi_l(\phi) &= \cos(l\phi) \text{ for even modes} \\ &= \sin(l\phi) \text{ for odd modes,} \end{aligned}$$

where a denotes the radius of the core. J_l represents the lth order of the Bessel function, K_l is the lth order of the modified Bessel function, u and w represents the normalized propagation constants and can be expressed as follows

$$\begin{aligned} u &= \sqrt{k^2 n_{co} - \beta^2} \\ w &= \sqrt{\beta^2 - k^2 n_{cl}}. \end{aligned}$$

Where n_{co} and n_{cl} represents the refractive index of the core and cladding respectively and $k = \frac{2\pi}{\lambda}$.

Graded index fibers

Graded index fibers have a core whose refractive index decreases with an increase in the radial distance from the optical axis of the fiber. Parts of the core which are closer to the radial axis have a higher refractive index as compared to those that are near the cladding-core interference. Light rays experience different velocities and follow a sinusoidal path as they propagate through the fiber. The refractive index can be approximated to be nearly parabolic, which minimizes modal dispersion resulting in continual refocusing of the rays inside the core of the fiber [74]. Figure 3.7 illustrates the profile of a graded index fiber.

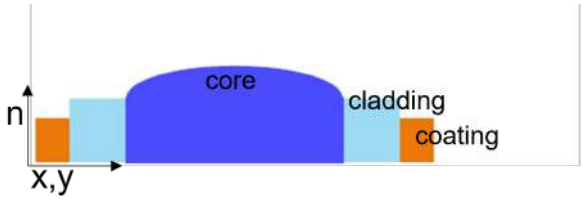

FIGURE 3.7: Illustration of a graded index fiber. The refractive index approximates a parabolic function and decreases as it moves away from the radial axis.

The graded index refractive index can be represented as follows

$$n^2(r) = n_{co}^2(1 - 2\triangle r^2). \tag{3.6}$$

In the paraxial regime $\triangle \cong (n_{co} - n_{cl}/an_{co})$, supports LG modes and petal modes that can be mathematical written as

$$LG_{l,p}^{e} = A_{l,p}(r,z)\cos(l\phi) = A_{l,p}(r,z)[\exp(il\phi) + \exp(-il\phi)], \tag{3.7}$$

$$LG_{l,p}^{0} = A_{l,p}(r,z)\sin(l\phi) = A_{l,p}(r,z)[\exp(il\phi) - \exp(-il\phi)], \tag{3.8}$$

where $A_{l,p}$(r,z) represents the LG radial profile. Table 3.1 contains the difference between the step index and graded index fiber.

For our research we use the step index fiber, because of its uniform refrac-

Step index fiber	Graded index fiber
Has both SMF and MMF	Only MMF
MMF has a core size (50 or 62.5 um) Light propagates in zig-zag manner	Core diameter of 50 um. Light propagates in sinusoidal manner
Has low attenuation for SMF and high for MMF	Has high attenuation
Has low bandwidth	Has high bandwidth
No. of modes it can support $N_{step} = \frac{v^2}{2}$	No. of modes it can support $N_{grad} = \frac{v^2}{4}$.

TABLE 3.1: Table of the difference between the step index fiber and graded index fiber [75].

tive index profile. Modes propagating through the fiber experience the same

velocity as such reaching the end of the fiber simultaneously. Next we will discuss different parameters of the fiber that will help us determine the number of modes our fiber can support.

3.1.2 Fiber parameters

In this research we use a 780HP single mode fiber from Thorlabs, this fiber is designed to work for wavelengths ranging from 780 - 970 nm. If the wavelength used is less than that of the cut-off wavelength then the fiber acts as a few mode fiber, for example the wavelength used in the experiment is less than the recommended wavelength as such allowing multiple modes to propagate through, for this research a 633 nm wavelength was used. Therefore our fiber acts as a few mode fiber. The cut-off wavelength is the wavelength at which the fiber acts as a single mode fiber. The cut-off wavelength can mathematically be expressed as [76]

$$\lambda_c = \frac{2\pi a}{V_c}\sqrt{n_{co}^2 - n_{cl}^2}. \tag{3.9}$$

Where λ_c is the cut-off wavelength, a is the core radius, n_{co} and n_{cl} is the refractive index of the core and cladding respectively and V_c is the cut-off Vnumber given by 2.405.
It is crucial for this experiment to know the number of modes the fiber can support, as the fewer modes propagating through the fiber the less the cross talk between the modes as they propagate. This parameter is known as the V number. The V number, also known as the normalized frequency parameter, is to determine the number of modes an optical fiber can support at a given wavelength. The V number can mathematically be expressed as follows [77]

$$V = \frac{\pi d}{\lambda}\sqrt{n_{co}^2 - n_{cl}^2}. \tag{3.10}$$

Where d is the core diameter of the fiber. IF
$V < 2.405$ the fiber is said to be a single mode fiber.
$V > 2.405$ the fiber is a multimode fiber
$V = 2.405$ the fiber corresponds to the cut-off wavelength.
For a step index fiber the V-number is given by

$$N = \frac{V^2}{2}. \tag{3.11}$$

We can now calculate the number of modes (N) that can be supported by the 780HP single mode fiber at a wavelength of 633 nm. Refractive index of the core is given by 1.4540 and of the cladding is given by 1.4482 with the core diameter of 4.4 um

$$V = \frac{2\pi}{\lambda} d\sqrt{n_{co}^2 - n_{cl}^2} = dNa. \tag{3.12}$$

From the above equation V is 4 shown on the dispersion curve in fig. (3.9) , the number of supported modes is 8.

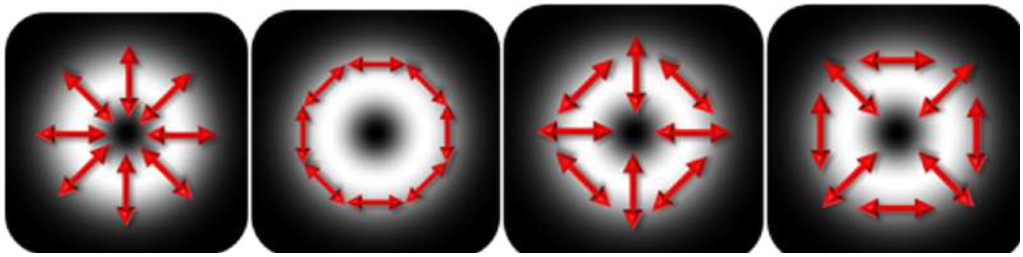

FIGURE 3.8: Modes that are supported by the 780 - 970 nm single mode fiber when used with the 633 nm wavelength.

These modes can be represented on a dispersion curve of HE and TE modes as they propagate in an optical fiber as shown In fig. (3.9), where the doted line represents the calculated V parameter.

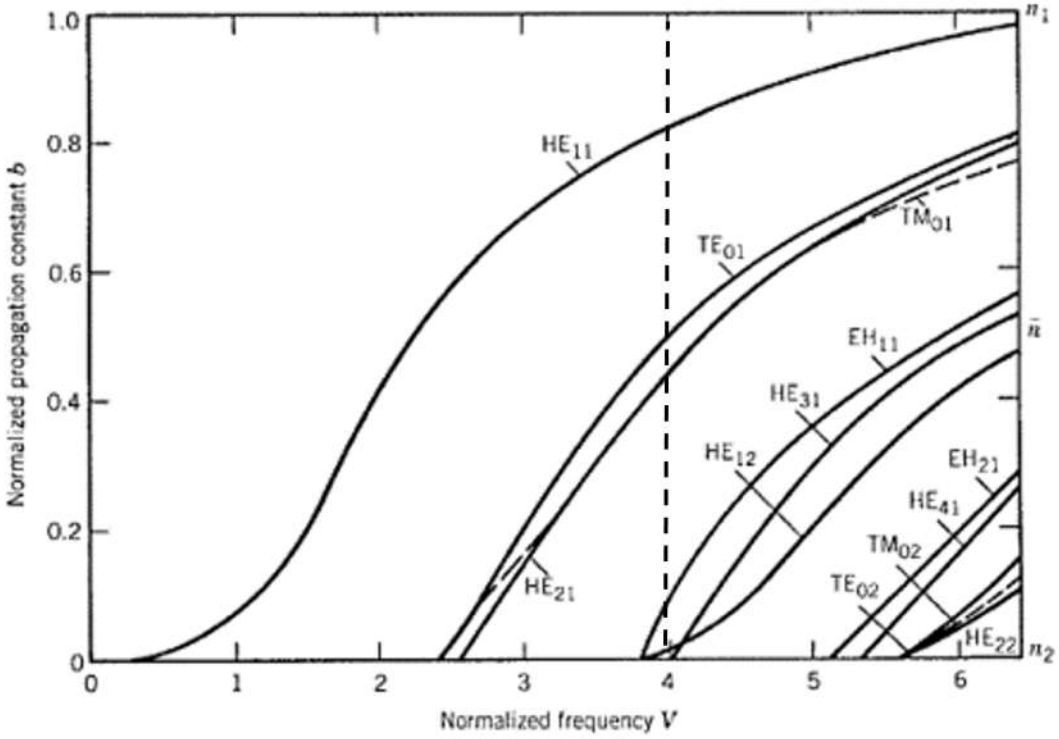

FIGURE 3.9: Dispersion curve of different modes as they propagate through the fiber, the doted line represents the V parameter given by 4 in this case meaning the fiber supports 4 modes and the fundamental mode [78] .

3.1.3 Coupling efficiency

Light propagating in a single mode fiber with high coupling efficiency has many applications in optical communication because of high bandwidth, suitability for long distance and minimal modal coupling. Beam coupled inside the fiber typically refers to a process of injecting a laser beam into an optical fiber so that the light is confined within the fiber's core and travels along its length. Coupling efficiency is the representation of how well the

incident beam can be coupled inside the fiber. This can be mathematically expressed as the function of the total power in the optical beam which is coupled in the fiber [79]. In order for light to be launched successfully into a single mode fiber the following steps need to be followed [80].
1. The beam radius size should approximate the fiber mode size.
2. The fiber tip should be at the focal plane of the beam waist.
3. Lastly the fiber should be aligned such that the beam waist enters the fiber at the correct orientation.
In order to obtain a high coupling efficiency the Gaussian mode from the laser source and the fiber mode should overlap perfectly and this can be represented by the overlap integral equation as follows [81]. If $f(r)$ is the field of the incident beam and $g(r)$ is the field of the fiber mode. Assuming that $f(r) = g(r)$, we have

$$\begin{aligned} f(r) &= \sum_i g_i(r), \\ \implies f(r)g_i^* &= \textstyle\sum_i c_i g_i(r) g_i^*(r), \\ \implies \textstyle\int_s f(r)g_i^*(r) &= c_i \textstyle\int_s g_i(r) g_i^*, \end{aligned} \tag{3.13}$$

now solving for c_i, we get

$$c_i = \frac{\int_s f(r)g_i^*(r)ds}{\int_s g_i(r)g_i^*(r)ds}, \tag{3.14}$$

the coupling efficiency can mathematically be written as

$$\eta = \frac{P_{out}}{P_{in}}. \tag{3.15}$$

We can now relate the coupling efficiency to the coefficient c_i in Eq.(3.14)

$$P_{out} = \frac{|c_i|^2}{\sum_i |c_i|^2} P_{in}, \tag{3.16}$$

where P_{out} is the output power, $\frac{|c_i|^2}{\sum_i |c_i|^2}$ is the normalized power and P_{in} is the input power.
Since $\sum_i |c_i|^2 = P_{in}$ from Eq.(3.16) we get

$$P_{out} = \frac{|c_i|^2}{P_{in}} P_{in} = |c_i|^2, \tag{3.17}$$

therefore coupling efficiency can be written as

$$\eta = \frac{|c_i|^2}{P_{in}}. \tag{3.18}$$

Where $|c_i|^2$ can be expressed as

$$|c_i|^2 = \frac{|\int_s f(r)g_i^*(r)ds|^2}{|\int_s g_i(r)g_i^*(r)ds|^2}. \tag{3.19}$$

The incident light of the Gaussian mode can be written as follows

$$f(r) = \frac{2P_{in}}{\pi w^2} \exp -(\frac{r}{w})^2. \tag{3.20}$$

The fiber mode can be written as

$$g(r) = \frac{2}{\pi \hat{w}^2} \exp -(\frac{r}{w})^2. \tag{3.21}$$

Where $\hat{w} = w$. The overlap integral in cylindrical coordinates can be written as follows

$$\begin{aligned} |c_i|^2 &= \frac{|\int\int f(r)g(r)rdrd\theta|^2}{|\int\int g(r)g^*(r)rdrd\theta|^2}, \\ &= \frac{4P_{in}}{(w\hat{w})^2[\frac{1}{w^2} - \frac{1}{\hat{w}^2}]}. \end{aligned} \tag{3.22}$$

Theoretically, coupling efficiency can be expressed as

$$\eta = \frac{4}{(w\hat{w})^2[\frac{1}{w^2} - \frac{1}{\hat{w}^2}]}. \tag{3.23}$$

Experimentally the coupling efficiency can be written as follows

$$\eta = \frac{P_{out}}{P_{in}}. \tag{3.24}$$

It is nearly impossible to couple all the light from the incident source into the fiber, this is due to the imperfection of the fiber during manufacturing and it is difficult to experimentally align the single mode fiber. Figure 3.10 compares the simulated and experimental results for the coupling efficiency.

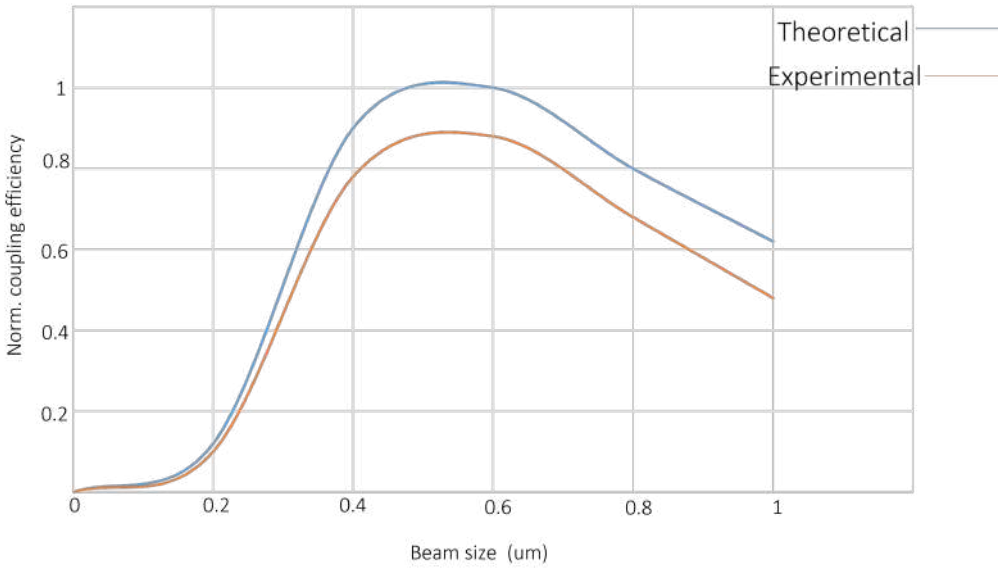

FIGURE 3.10: Plot of the experimental and theoretical coupling efficiency for a single mode fiber.

It is impossible to couple all the light into the fiber, when the incident mode is less than the fiber mode. Light injected into the fiber is lost into the cladding and excites the cladding mode. When the beam size of the fiber is bigger than the fiber mode, most of the light gets lost to the environment. From the graph we can notice a 88% coupling efficiency was obtained when the core radius of the fiber and the incident beam waist were approximately equal. A 430 nm - 633 nm wavelength single mode fiber with a core radius of used was 0.5 um.

3.2 Vector Flattop beam propagation in optical fiber

Figure 3.11 illustrates the experimental setup used to generate and detect vector flattop beams propagating in an optical fiber. A 633 nm HeNe beam was passed through a HWP that changes the polarisation state of the incident light to diagonally polarised light. It was then illuminated on the SLM display screen encoded with a hologram with azimuthal charge $l = 1$ with no grating and the modulated and unmodulated beams were reflected off the screen propagating collinear to each other, thus producing a vector flattop beam. Lens-1 and the objective lens were used to image the SLM screen, and an aperture was then used to filter out unwanted orders. The objective lens was also used to focus the beam waist into a 1 m with wavelengths ranging from 780 nm -970 nm step index fiber with a core radius of 2.1 um. The fiber coupler with lens (3 mm) and lens-2 were used to image the fiber plane to the DMD screen. The DMD screen was encoded with the complex conjugate of the generated mode for modal decomposition. Lens-3 was used to transfer the DMD plane to the Fourier plane and the camera recorded the intensity profiles of the detected modes. In this section we investigate how the fiber changes the polarisation state and modal content of the injected vector flattop beam.

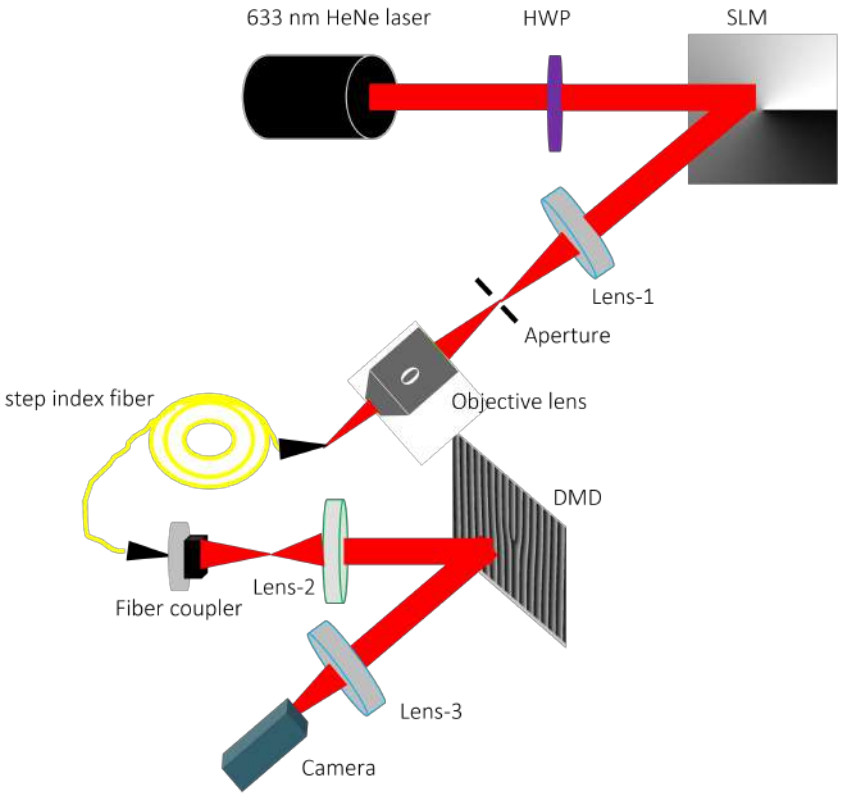

FIGURE 3.11: Experimental setup used to generate a vector flattop beam, which was coupled into a step index fiber and subsequently detected after emerging from the fiber.

Figure 3.12 is a comparison of the vector flattop beam before and and after propagating through a few mode fiber. We calculated the correlation between the vector flattop before the fiber and after the fiber and we found a 84% correlation.

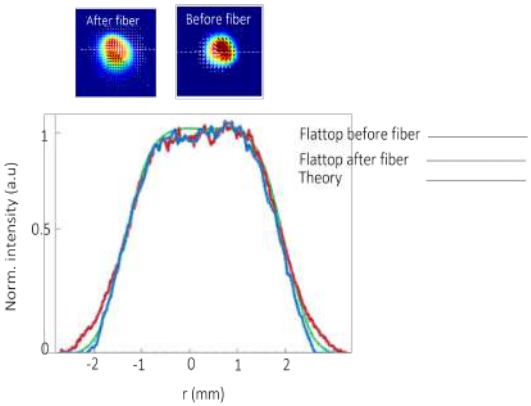

FIGURE 3.12: 1-D intensity profiles of the vector flattop beams before and after propagating through the fiber and the 2-D intensity profiles of the flattop before and after the fiber.

3.3 Polarisation and mode coupling analysis

3.3.1 Stokes Polarimetry

The state of polarisation of light can be defined using the orientation of the electric field which is given by $E(x,y,z,t)$, which depends on both position (x,y,z) and time t. The electric field vector field travelling in the z - direction across the fiber can be written as

$$E(x,y,z,t) = Re[(f_x(x,y)A_x(z,t))\hat{x} + (F_y(x,y)A_y(z,t))\hat{y}]. \tag{3.25}$$

Light can be described as two orthogonal electric field vectors which differ in both amplitude (A,F) and phase as follows

$$E_x(z,t) = E_{0x}\cos(\tau_w + \phi_0). \tag{3.26}$$

$$E_y(z,t) = E_{0y}\cos(\tau_w + \phi_0). \tag{3.27}$$

Polarisation of light occurs when the two electric field vectors differ in phase and amplitude [82]. The change in polarisation of the modes as they propagate through the fiber is caused by a phenomenon called birefringence when light is separated into two paths. This birefringence is caused by the imperfections of the fiber such as stress applied on the fiber by bending it or the change in atmospheric temperature. In this research we use the technique of Stokes Polarimetry to show how the state of polarisation of a vector flattop beam changes as it propagates through a step index, few mode fiber. In order to obtain the Stokes parameters we first need to determine the intensity measurements of the desired field. Figure (3.13) shows the intensity measurements of the flattop (a) before and (b)after propagating through the fiber.

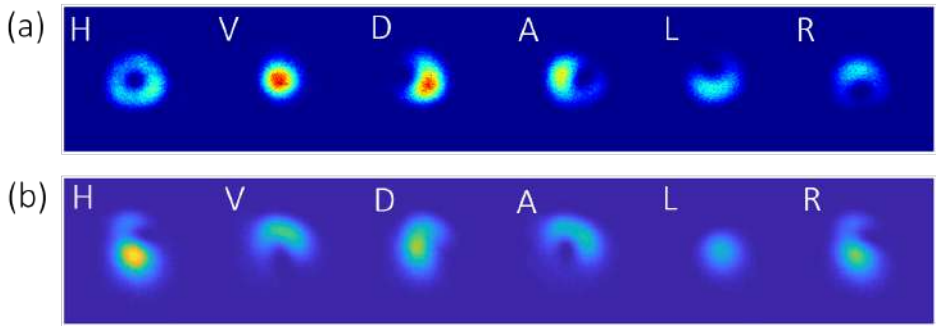

FIGURE 3.13: Illustrates the intensity measurements of the vector flattop: (a) is the intensity measurements before the fiber and (b) is the intensity measurements after the fiber.

From fig.(3.13), we can observe the change in the intensity measurements of the vector flattop beam before and after propagating through the fiber. As already stated in Chapter 2, from the intensity measurements we can determine the Stokes parameters. Figure 3.14 compares the Stokes parameter of the vector flattop beam (a) before and (b) after the fiber.

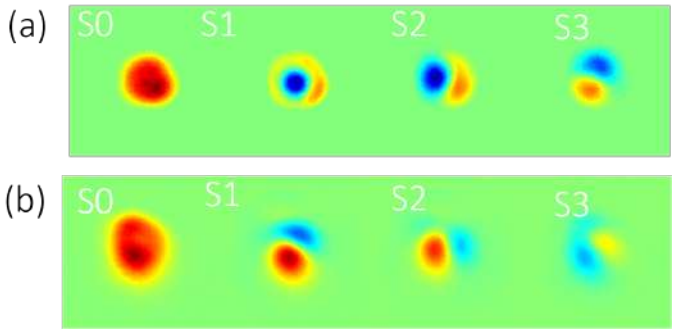

FIGURE 3.14: Illustration of the 2-D Stokes parameters of a vector flattop beam: (a) before the fiber and (b) after the fiber.

The Stokes parameters shown in fig. (3.14) can be used to reconstruct the polarisation state of the vector beams. Figure 3.15 shows the comparison between the reconstructed polarisation state (a) before and (b) after the fiber.

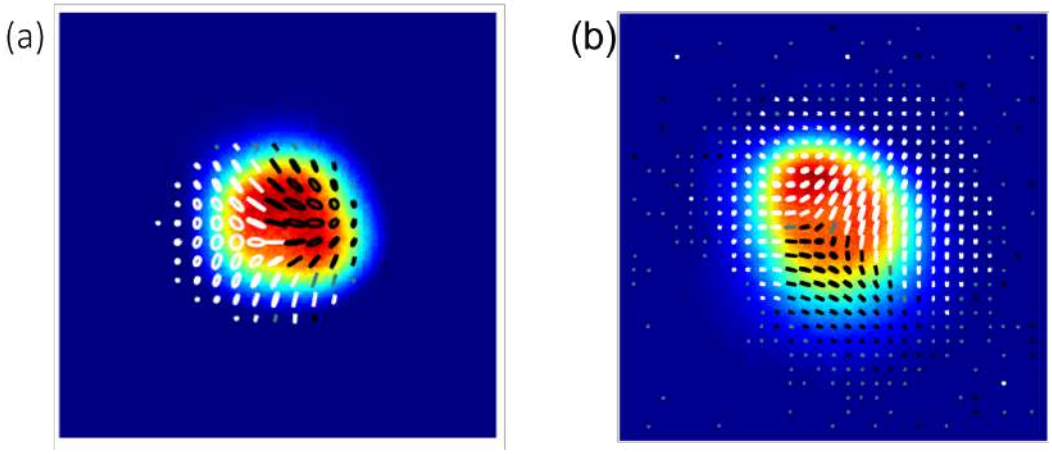

FIGURE 3.15: 2-D polarisation state of the vector flattop beams: (a) before the fiber and (b) after propagating through the fiber.

From the reconstructed polarisation states shown in fig. (3.15), we can observe how the polarisation of the output mode has changed compared to the input mode. Fibers are very sensitive to work with. It was also observed during the experiment that by applying any force (bending) or stretching the fiber the polarisation state of the output mode can be changed. Changing the injection position of the fiber can also change the polarisation of the output mode.

3.3.2 Modal coupling

Modal coupling in fibers can be defined as a process in which there is a transfer of energy between neighboring modes as they travel through the fiber and this can change the input mode. Mode coupling in fibers can be caused by a number of factors such as the imperfection of the core during the manufacturing process, by external perturbation experienced by the fiber such as

variation of the refractive index, bending of the fiber or the change in room temperature which can cause the fiber to expand or shrink [83, 84].

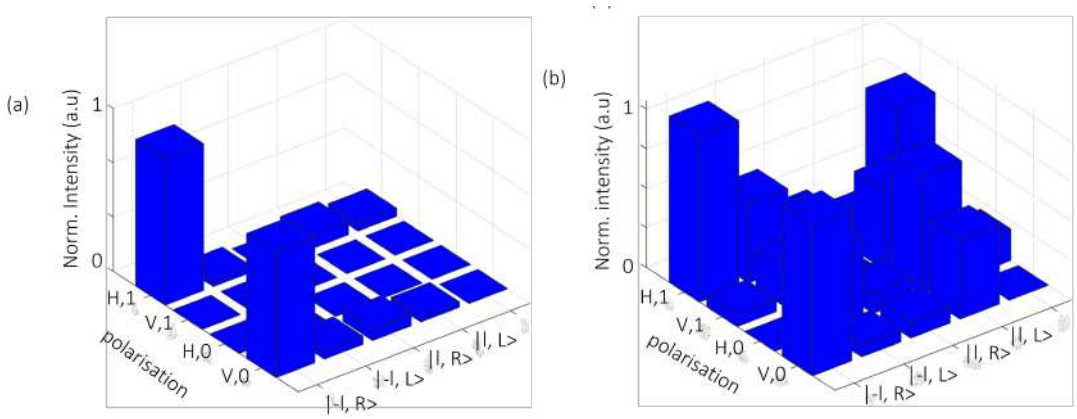

FIGURE 3.16: Modal decomposition of a vector flattop beam: (a) before the fiber and (b) after the fiber.

Figure 3.16 illustrates the modal decomposition of the vector flattop beam (a) before the fiber and we can only notice two peaks, which represents the Gaussian and vortex beams used to generate the vector flattop beam and (b) we can see several peaks which tells us that the modes couple as the propagate through they fiber. The bending or stretching of the fiber not only affects the polarisation of the mode propagating through it, but it also affects which modes are being excited subsequently affecting how the modes couple among each other. By injecting only a Gaussian beam into the fiber we can produce a flattop beam after the fiber, this means that the Gaussian beam can excite and couple with the $l = 1$ mode inside the fiber as it propagates generating a flattop beam. This can also be achieved by injecting a vortex beam into the fiber coupling and exciting the Gaussian mode to produce a flattop beam. Figure 3.17 shows the 1-D intensity profile of the and experimental vortex and Gaussian beams which were injected individually into the fiber. The calculated correlation between the simulated and experimental vortex and Gaussian beams was found to be 85% and 91% respectively.

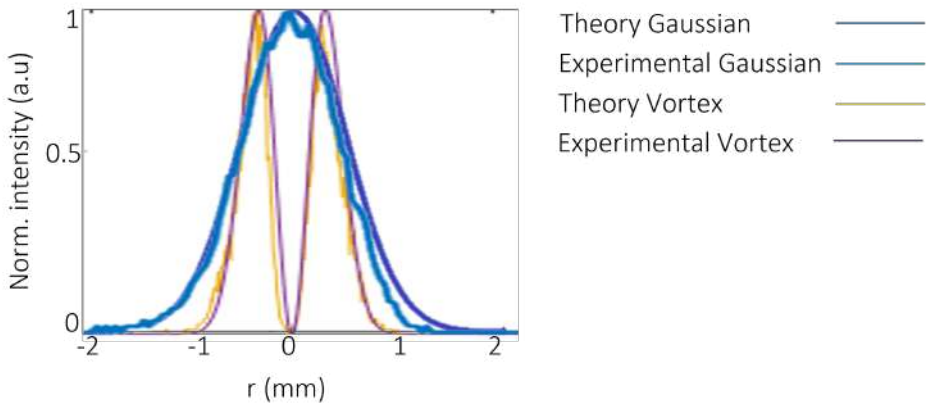

FIGURE 3.17: 1-D intensity distribution of the simulated and experimental vortex and Gaussian beams

We simulated the Stokes parameters and modal analysis of the vortex and Gaussian beams before propagating through an optical fiber. Figure 3.18 shows the 2-D intensity measurements of the vortex and Gaussian beams before the fiber

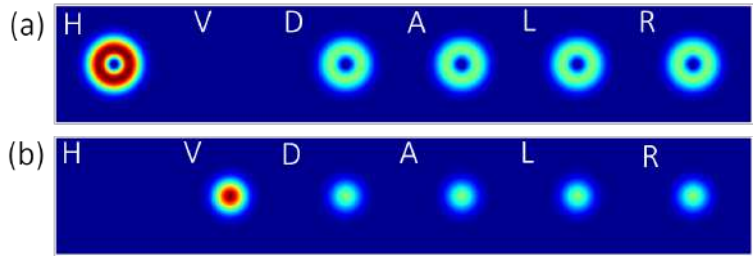

FIGURE 3.18: 2-D simulated intensity measurements of (a) the vortex beam and (b) the Gaussian beam before the fiber.

From the simulated intensity measurements we can now calculate the Stokes parameters of the vortex and Gaussian beams before the fiber. Figure 3.19 illustrates (a) Stokes parameters of the vortex beam and (b) is the Stokes parameters of the Gaussian beam before the fiber.

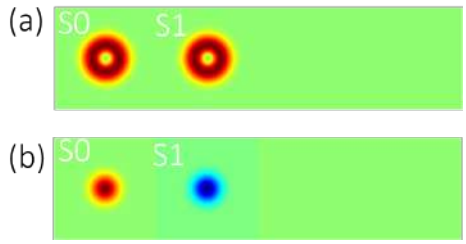

FIGURE 3.19: Illustrates simulated (a) Stokes parameters of the vortex beam and (b) is the Stokes parameters of the Gaussian beam before the fiber.

From the Stokes parameters we can then reconstruct the polarisation states of the two fields. Figure 3.20 shows the reconstructed polarisation states of the Vortex and Gaussian fields respectively before the fiber.

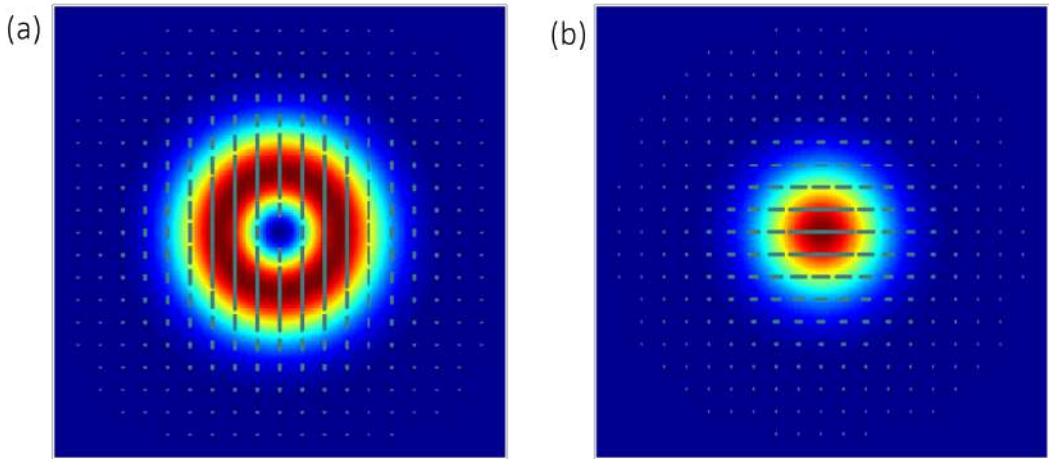

FIGURE 3.20: Simulated reconstructed polarisation state of the vortex and Gaussian beam respectively.

Figure 3.21 shows the 1-D intensity profile of the flattop beam before the fiber, flattop generated by injecting only a Gaussian and flattop generated by injecting only a vortex. On top is the 2-D intensity distribution of the vector flattop before the fiber, generated by injecting a Gaussian and vortex beam respectively.

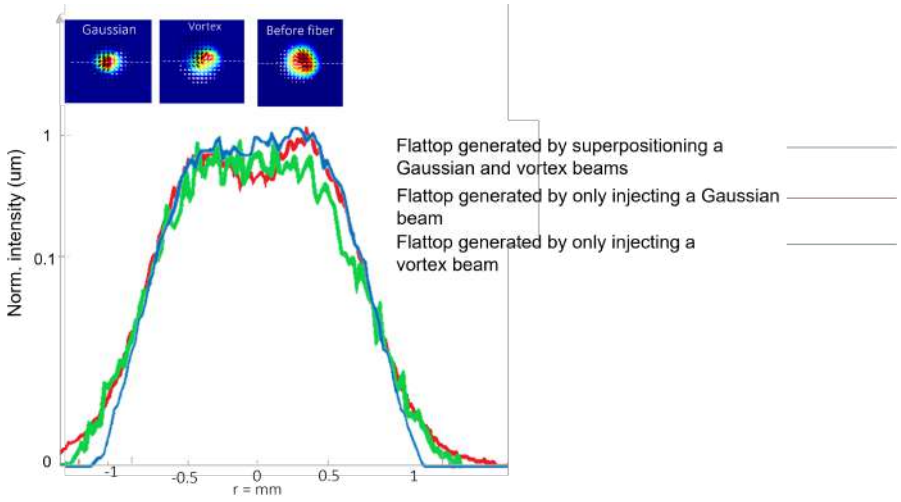

FIGURE 3.21: Illustration of 1-D intensity profiles of the vector flattop beams before the fiber, generated by injecting only a Gaussian beam into the fiber and generated by injecting only a vortex beam into the fiber.

Another method of generating a vector flattop beam is by injecting only a Gaussian beam or only a vortex beam into the fiber. Firstly we injected the Gaussian beam only to generate the vector flattop beam and this was compared with the vector flattop generated in free space with a correlation of 62%. Thus we can conclude that we can generate a vector flattop by injecting only a Gaussian beam.
Secondly we injected only a vortex beam into the fiber to generate a vector flattop beam and the correlation with the vector flattop beam before the fiber was calculated to be 78% as such we can conclude that we can generate the vector flattop by encoding only a vortex beam. This is because modes that are close together or in the same group are more likely to couple than those that are further apart from each other. We also performed Stokes parameters and modal coupling analysis.

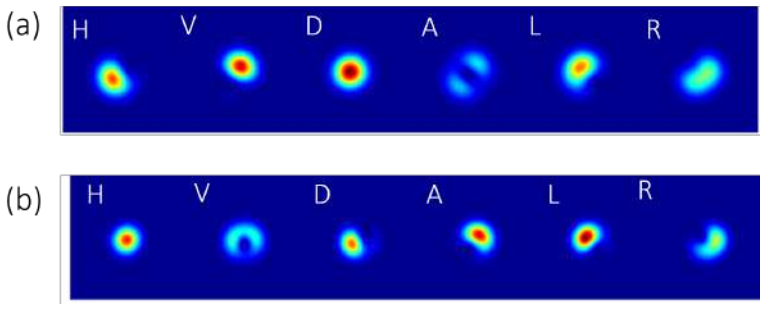

FIGURE 3.22: 2-D intensity measurements of the flattops after the fiber (a) generated by injecting only a vortex and (b) generated by injecting only a Gaussian.

Figure 3.22 shows the intensity measurements of the flattops after the fiber (a) generated by injecting only a vortex mode and we can see two petals

on the diagonal polarisation which indicates coupling between the mode $l = \pm 1$ and (b) generated by injecting only a Gaussian beam. From the intensity measurements we can determine the Stokes parameters.

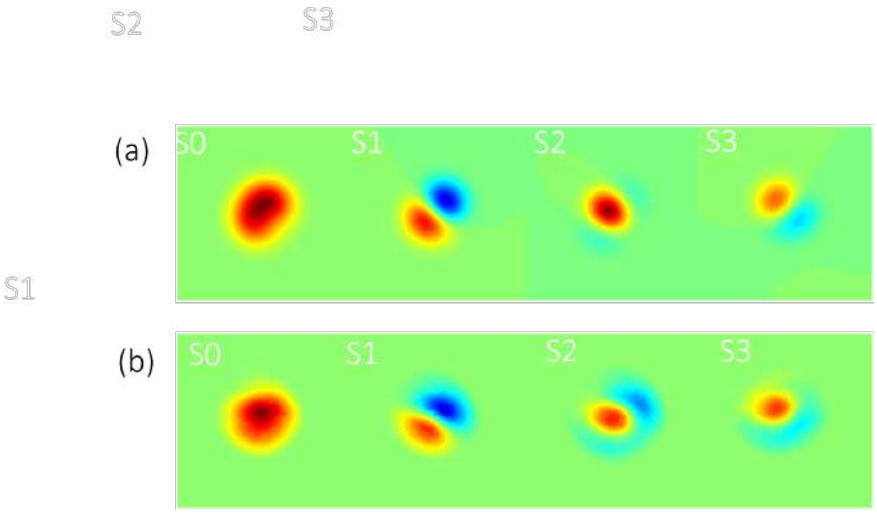

FIGURE 3.23: Stokes parameters of the flattop beam after the fiber (a) generated by injecting only a vortex and (b) generated by injecting only a Gaussian.

Figure 3.23 shows the Stokes parameters of the flattop beam after the fiber (a) generated by injecting only a vortex, because of the coupling between $l = \pm 1$ we notice a change in the shape of the flattop. We can see how the $S0$ in fig 3.23 (a) has an elongated shape as compared to fig. 3.19 (b), this can also be seen in Chapter 2, section 2.4 (b) which has a circular shape. We can now reconstruct the polarisation state of the flattop beams after the fiber.

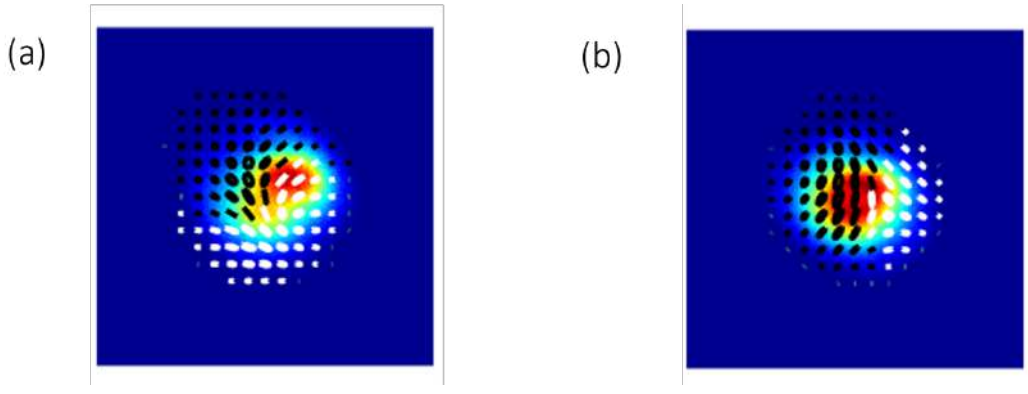

FIGURE 3.24: 2-D reconstructed polarisation state of the flattop after the fiber (a) generated by injecting a vortex and (b) generated by injecting only a Gaussian beam into the fiber.

Figure 3.24 is the reconstructed polarisation state of the flattop after the fiber (a) generated by injecting only a vortex, which we can see an elongated shape which is caused by the coupling between $l \pm 1$ and $l = 0$ and (b) generated by injecting only a Gaussian beam. The fiber did not only change the

shape of the output beam but also the polarisation state. The fiber acts differently depending on the mode injected thus we see the difference in the polarisation of the flattop beams.
Figure 3.25 shows the simulated modal decomposition of the (a) vortex beam and (b) Gaussian beam respectively before the fiber. We notice only one peak in both cases.

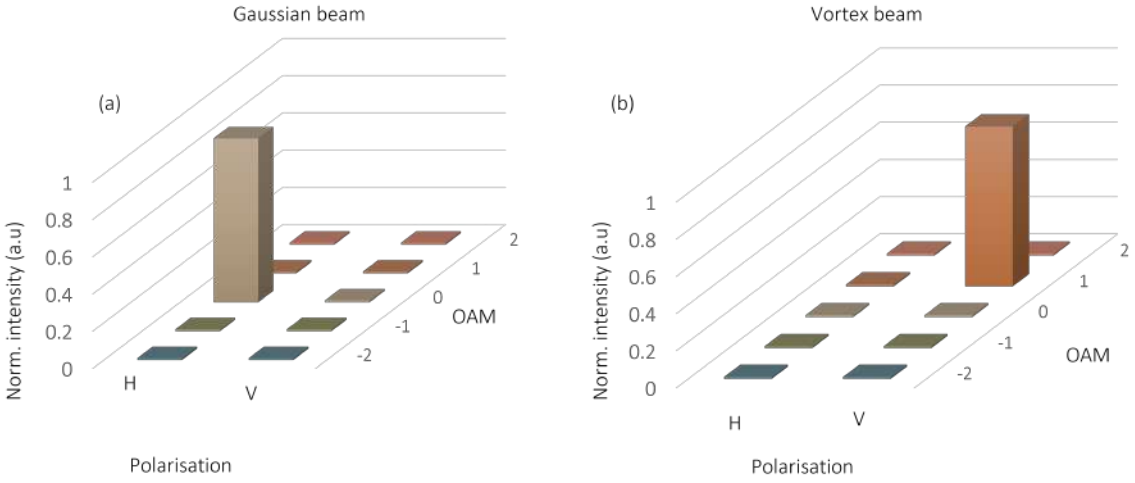

FIGURE 3.25: The simulated modal decomposition of the (a) Gaussian beam and (b) Vortex beam respectively before the fiber.

Modal decomposition was also used to determine how the modes couple into each other as they propagate inside the fiber.

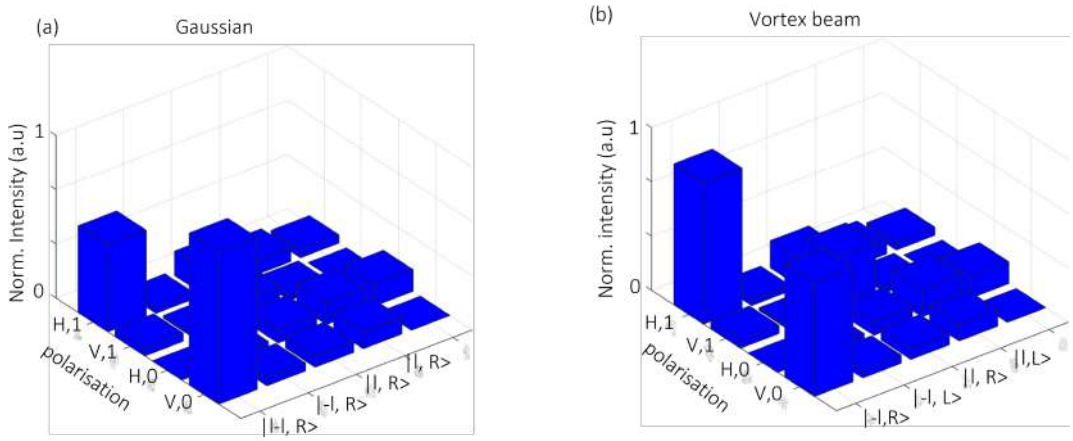

FIGURE 3.26: Modal decomposition of flattop beams after the fiber (a) generated by injecting only a vortex and (b) generated by injecting only a Gaussian beam.

Figure 3.26 shows the modal content of the flattop beam after the fiber generated by (a) injecting only a vortex and we can see three main peaks ($l = \pm 1$ and $l = 0$), and we can also see the small peaks which shows the

transfer of energy between modes as they propagate through the fiber. (b) Is the modal decomposition of the flattop generated after the fiber by injecting only a Gaussian beam. We can only notice two peaks and small peaks that also suggest we also have modal coupling between the modes as they travel through the fiber. We can conclude from the results obtain in this section that it is better to generate a vector flattop beam before propagating through the fiber than generating a vector flattop beam by only injecting a Gaussian beam or vortex beam.

Chapter 4

Conclusion and Future Work

In this dissertation we discuss the properties of a uniform flattop beam and how it changes as it propagates through a few mode fiber. We compare the Stokes polarimetry measurements before and after the fiber, and also the modal content of the initial and emerging flattop mode. In Chapter 1, we discuss the theoretical behaviour of light by using Maxwell's equation to derive the Helmholtz wave equation. Different types of laser beam parameters such as the radius of curvature, Rayleigh range, beam waist were discussed. We also discuss the solution to the wave equation i.e the fundamental solution to the wave equation (Gaussian beams), the LG modes with both radial and azimuthal dependence, the vortex which only depends on the azimuthal index, the HG modes with Hermits polynomials (m, n indices) and lastly we discuss the vector flattop which is generated from the superposition of the Gaussian and vortex modes which are orthogonal to each other.
In Chapter 2, we discuss how to generate and detect spatial modes, using a SLM. We firstly give a brief introduction of how SLMs work, and how holograms are encoded digitally to shape light dynamically. We discuss the importance of calibrating SLMs for specific wavelengths before implementing beam shaping,for our research we used a 633 nm HeNe laser. We also discuss how we calibrate SLMs using interferometric techniques. We show how the calibration curve looks like before and after calibration, with the phase shift ranging from 0 to 2π after calibration. We discuss the two techniques that we use to shape light in the laboratory by using SLM, which is the complex amplitude modulation and the phase only modulation. We look at the characteristics of a Digital Micro-mirror Device, and how it is used to tailor different properties of light. The generation and detection of modes was demonstrated in the laboratory as a proof-of-concept showing the different LG mode intensity profiles, which had a correlation of 86% between the simulated and experimentally generated LG modes. The SLM was used to generated vector flattop beams by modulating only the phase of the incident beam. We calculated the correlation between the simulated and experimental vector flattop beams and obtained a correlation of 92%. We discussed how to measure the Stokes parameters and how it can be used to determine the change in polarisation state of an optical field. In order to determine the Stokes parameters we should first obtain the intensity measurements of the desired field and from the Stokes parameters we can reconstruct the polarisation state of the field. We discuss how to use a DMD to perform modal decomposition on the field of interest by encoding a complex conjugate hologram of the desired

mode on the DMD display screen.
In Chapter 3 we discuss how light propagates through an optical fiber. We also look at the different types of fibers and their parameters, for this research a 1 meter step index few mode fiber with V parameter of 4 was used. We measured the coupling efficiency of a Gaussian mode as it propagates through a single mode fiber and the experimental results and a coupling efficiency of 88% was achieved. A flattop beam was propagated through a few mode fiber and the correlation between the flattop before the fiber and after the fiber was obtained to be 86%. Stokes polarimetry measurements and modal decomposition analysis were made. It is observed that the fiber alters both the polarisation state and modal content of the input mode.

4.1 Future Work

Applying stress (such as bending the fiber) or applying pressure to the fiber can change the modes excited by the fiber, and can also change how the modes couple as they propagate through the fiber.

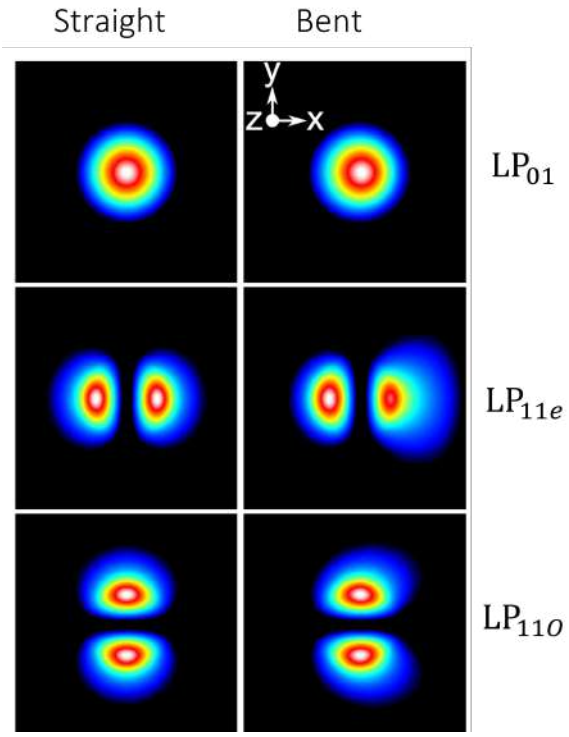

FIGURE 4.1: Illustration of how the fiber sees the modes propagating under different condition, with no stress or bending and when the fiber is bent.

Figure (4.1) shows how the mode changes inside the fiber if stress is applied to the fiber. An experiment can be conducted to see how the modes change as they propagate through the fiber, when the fiber is exposed to different stresses and pressure and the Stoke polarimetry measurements and

modal decomposition analysis can be performed. The angle at which the input beam enters the fiber also determines which modes get excited and how modes couple into each other as they propagate. During my MSc we have played with the angle at which the mode enters the beam and we were able to detect vector modes by changing the angle of incident. We can perform and experiment where we change the angle at which the mode enters the fiber and measure how the Stokes polarimetry and modal content of the input and emerging mode changes. For future work, we can propagate radial modes into the fiber and analyse the modal decomposition and Stokes polarimetry before and after the fiber.

Bibliography

1. Goodman, J. W. Introduction to Fourier optics. 3rd. *Roberts and Company Publishers* **3** (2005).
2. Dickey, F. M. & Lizotte, T. E. *Laser beam shaping applications* (CRC Press, 2017).
3. Dickey, F. M. *Laser beam shaping: theory and techniques* (CRC press, 2018).
4. Huray, P. G. *Maxwell's equations* (John Wiley & Sons, 2011).
5. Griffiths, D. J. *Introduction to electrodynamics* (Prentice Hall New Jersey, 1962).
6. Galvez, E. J. Gaussian beams. *Colgate University* (2009).
7. Levy, U., Silberberg, Y. & Davidson, N. Mathematics of vectorial Gaussian beams. *Advances in Optics and Photonics* **11,** 828–891 (2019).
8. Self, S. A. Focusing of spherical Gaussian beams. *Applied optics* **22,** 658–661 (1983).
9. Abramochkin, E. & Volostnikov, V. Generalized gaussian beams. *Journal of Optics A: Pure and Applied Optics* **6,** S157 (2004).
10. Jordan, R. H. & Hall, D. G. Free-space azimuthal paraxial wave equation: the azimuthal Bessel–Gauss beam solution. *Optics letters* **19,** 427–429 (1994).
11. Svelto, O. & Hanna, D. C. *Principles of lasers* (Springer, 1998).
12. Quimby, R. S. *Photonics and lasers: an introduction* (John Wiley & Sons, 2006).
13. Allen, L., Beijersbergen, M. W., Spreeuw, R. & Woerdman, J. Orbital angular momentum of light and the transformation of Laguerre-Gaussian laser modes. *Physical Review A* **45,** 8185 (1992).
14. Arlt, J., Kuhn, R. & Dholakia, K. Spatial transformation of Laguerre–Gaussian laser modes. *Journal of modern optics* **48,** 783–787 (2001).
15. Lerner, V., Shwa, D., Drori, Y. & Katz, N. Shaping Laguerre–Gaussian laser modes with binary gratings using a digital micromirror device. *Optics letters* **37,** 4826–4828 (2012).
16. Andrews, D. L. *Photonics, Volume 1: Fundamentals of photonics and physics* (John Wiley & Sons, 2015).
17. Allen, L., Padgett, M. & Babiker, M. in *Progress in optics* 291–372 (Elsevier, 1999).

18. Allen, L. & Padgett, M. The orbital angular momentum of light: An introduction. *Twisted Photons: Applications of Light with Orbital Angular Momentum,* 1–12 (2011).
19. Morton, N. An introduction to the Poynting vector. *Physics Education* **14,** 301 (1979).
20. Saghafi, S., Sheppard, C. & Piper, J. Characterising elegant and standard Hermite–Gaussian beam modes. *Optics communications* **191,** 173–179 (2001).
21. Lü, B. & Ma, H. A comparative study of elegant and standard Hermite–Gaussian beams. *Optics communications* **174,** 99–104 (2000).
22. Cai, Y. & Lin, Q. The elliptical Hermite–Gaussian beam and its propagation through paraxial systems. *Optics communications* **207,** 139–147 (2002).
23. Zhan, Q. Cylindrical vector beams: from mathematical concepts to applications. *Advances in Optics and Photonics* **1,** 1–57 (2009).
24. Maurer, C., Jesacher, A., Fürhapter, S., Bernet, S. & Ritsch-Marte, M. Tailoring of arbitrary optical vector beams. *New Journal of Physics* **9,** 78 (2007).
25. Ndagano, B., Sroor, H., McLaren, M., Rosales-Guzmán, C. & Forbes, A. Beam quality measure for vector beams. *Optics letters* **41,** 3407–3410 (2016).
26. Forbes, A. *Laser beam propagation: generation and propagation of customized light* (CRC Press, 2014).
27. Andrews, D. L. & Babiker, M. *The angular momentum of light* (Cambridge University Press, 2012).
28. Milione, G., Sztul, H., Nolan, D. & Alfano, R. Higher-order Poincaré sphere, Stokes parameters, and the angular momentum of light. *Physical review letters* **107,** 053601 (2011).
29. Ma, H. *et al.* Generation of flat-top beam with phase-only liquid crystal spatial light modulators. *Journal of Optics* **12,** 045704 (2010).
30. McLaren, M., Khanyile, T., Mthunzi, P. & Forbes, A. *Optical trapping with Super-Gaussian beams* in *Novel Techniques in Microscopy* (2013), JT2A–34.
31. Bhebhe, N., Rosales-Guzman, C. & Forbes, A. Classical and quantum analysis of propagation invariant vector flat-top beams. *Applied optics* **57,** 5451–5458 (2018).
32. Amako, J. & Sonehara, T. Kinoform using an electrically controlled birefringent liquid-crystal spatial light modulator. *Applied Optics* **30,** 4622–4628 (1991).
33. Efron, U. *Spatial light modulator technology: materials, devices, and applications* (CRC press, 1994).
34. Maurer, C., Jesacher, A., Bernet, S. & Ritsch-Marte, M. What spatial light modulators can do for optical microscopy. *Laser & Photonics Reviews* **5,** 81–101 (2011).

35. Neff, J. A., Athale, R. A. & Lee, S. H. Two-dimensional spatial light modulators: a tutorial. *Proceedings of the IEEE* **78,** 826–855 (1990).

36. Casasent, D. Spatial light modulators. *Proceedings of the IEEE* **65,** 143–157 (1977).

37. Efron, U. Spatial light modulator technology: materials, devices, and applications. *OPTICAL ENGINEERING-NEW YORK-MARCEL DEKKER INCORPORATED-* **49,** 47–47 (1995).

38. Scharf, T. *Polarized light in liquid crystals and polymers* (John Wiley & Sons, 2007).

39. Efron, U., Wu, S.-T. & Bates, T. Nematic liquid crystals for spatial light modulators: recent studies. *JOSA B* **3,** 247–252 (1986).

40. De La Tocnaye, J. D. B. & Dupont, L. Complex amplitude modulation by use of liquid-crystal spatial light modulators. *Applied Optics* **36,** 1730–1741 (1997).

41. Konforti, N., Marom, E. & Wu, S.-T. Phase-only modulation with twisted nematic liquid-crystal spatial light modulators. *Optics letters* **13,** 251–253 (1988).

42. Forbes, A., Dudley, A. & McLaren, M. Creation and detection of optical modes with spatial light modulators. *Advances in Optics and Photonics* **8,** 200–227 (2016).

43. Arrizón, V., Ruiz, U., Carrada, R. & González, L. A. Pixelated phase computer holograms for the accurate encoding of scalar complex fields. *JOSA A* **24,** 3500–3507 (2007).

44. Gray, A., Barkhouser, R., Hope, S. C., Smee, S. A. & Robberto, M. *Scattered light testing of digital micromirror devices (DMDs)* in *Advances in Optical and Mechanical Technologies for Telescopes and Instrumentation III* **10706** (2018), 1680–1687.

45. Dudley, D., Duncan, W. M. & Slaughter, J. *Emerging digital micromirror device (DMD) applications* in *MOEMS display and imaging systems* **4985** (2003), 14–25.

46. Scholes, S., Kara, R., Pinnell, J., Rodrıguez-Fajardo, V. & Forbes, A. Structured light with digital micromirror devices: a guide to best practice. *Optical Engineering* **59,** 041202 (2019).

47. Kreis, T. M., Aswendt, P. & Höfling, R. Hologram reconstruction using a digital micromirror device. *Optical Engineering* **40,** 926–933 (2001).

48. Sampsell, J. B. Digital micromirror device and its application to projection displays. *Journal of Vacuum Science & Technology B: Microelectronics and Nanometer Structures Processing, Measurement, and Phenomena* **12,** 3242–3246 (1994).

49. Nesbitt, R. S., Smith, S. L., Molnar, R. A. & Benton, S. A. *Holographic recording using a digital micromirror device* in *Practical holography XIII* **3637** (1999), 12–20.

50. Singh, K., Tabebordbar, N., Forbes, A. & Dudley, A. Digital Stokes polarimetry and its application to structured light: tutorial. *JOSA A* **37,** C33–C44 (2020).
51. Saleh, B. E. & Teich, M. C. *Fundamentals of photonics* (john Wiley & sons, 2019).
52. Rukhlenko, I. D., Dissanayake, C. & Premaratne, M. Visualization of electromagnetic-wave polarization evolution using the Poincaré sphere. *Optics letters* **35,** 2221–2223 (2010).
53. Thompson, B. J., Goldstein, D. & Goldstein, D. H. Polarized Light, revised and expanded (2003).
54. Schulze, C. *et al.* Wavefront reconstruction by modal decomposition. *Optics express* **20,** 19714–19725 (2012).
55. Huang, N. E. *Review of empirical mode decomposition* in *Wavelet Applications VIII* **4391** (2001), 71–80.
56. Schmid, P. J., Li, L., Juniper, M. P. & Pust, O. Applications of the dynamic mode decomposition. *Theoretical and computational fluid dynamics* **25,** 249–259 (2011).
57. Schulze, C., Dudley, A., Flamm, D., Duparre, M. & Forbes, A. Measurement of the orbital angular momentum density of light by modal decomposition. *New Journal of Physics* **15,** 073025 (2013).
58. Flamm, D. *et al.* Fast M 2 measurement for fiber beams based on modal analysis. *Applied optics* **51,** 987–993 (2012).
59. Litvin, I. A., Dudley, A., Roux, F. S. & Forbes, A. Azimuthal decomposition with digital holograms. *Optics Express* **20,** 10996–11004 (2012).
60. Tyndall, J. *Lectures and Essays* **10** (Watts, 1909).
61. Dong, L. & Samson, B. *Fiber lasers: basics, technology, and applications* (CRC press, 2016).
62. Blanc, W. & Dussardier, B. Formation and applications of nanoparticles in silica optical fibers. *Journal of Optics* **45,** 247–254 (2016).
63. Senior, J. M. & Jamro, M. Y. *Optical fiber communications: principles and practice* (Pearson Education, 2009).
64. Hecht, J. Birth of Fiber-Optic Imaging and Endoscopes. *OSA Centur y of Optics*, 53.
65. Lee, B. Review of the present status of optical fiber sensors. *Optical fiber technology* **9,** 57–79 (2003).
66. Kneebone, R. Total internal reflection: an essay on paradigms. *Medical education* **36,** 514–518 (2002).
67. Feynman, R. P., Leighton, R. B. & Sands, M. The feynman lectures on physics; vol. i. *American Journal of Physics* **33,** 750–752 (1965).
68. Zhu, S., Yu, A., Hawley, D. & Roy, R. Frustrated total internal reflection: A demonstration and review. *American Journal of Physics* **54,** 601–607 (1986).

69. Shirley, J. W. An early experimental determination of Snell's law. *American Journal of Physics* **19,** 507–508 (1951).

70. Snitzer, E. Cylindrical dielectric waveguide modes. *JOSA* **51,** 491–498 (1961).

71. Kapron, F., Keck, D. B. & Maurer, R. D. Radiation losses in glass optical waveguides. *Applied Physics Letters* **17,** 423–425 (1970).

72. GHATAK, A. A., Ghatak, A., Thyagarajan, K. & Thyagarajan, K. *An introduction to fiber optics* (Cambridge university press, 1998).

73. Snyder, A. W. & Love, J. D. Optical waveguide theory. *J. Opt. Soc. Am. A* **3,** 378 (1986).

74. Feit, M. & Fleck, J. Light propagation in graded-index optical fibers. *Applied optics* **17,** 3990–3998 (1978).

75. Arrue, J. *et al.* Design of mode scramblers for step-index and graded-index plastic optical fibers. *Journal of lightwave technology* **23,** 1253–1260 (2005).

76. Murakami, Y., Kawana, A. & Tsuchiya, H. Cut-off wavelength measurements for single-mode optical fibers. *Applied optics* **18,** 1101–1105 (1979).

77. Willner, A. *Optical fiber telecommunications* (Academic Press, 2019).

78. Jones, A. L. Coupling of optical fibers and scattering in fibers. *JOSA* **55,** 261–271 (1965).

79. Garcia, K. J. Calculating component coupling coefficients. *Laser focus world* **36,** 51–56 (2000).

80. Yeh, C. *Handbook of fiber optics: Theory and applications* (Academic Press, 2013).

81. Gilsdorf, R. W. & Palais, J. C. Single-mode fiber coupling efficiency with graded-index rod lenses. *Applied optics* **33,** 3440–3445 (1994).

82. Cloude, S. *Polarisation: applications in remote sensing* (OUP Oxford, 2009).

83. Fang, L. & Wang, J. Full-vectorial mode coupling in optical fibers. *IEEE Journal of Quantum Electronics* **54,** 1–7 (2018).

84. Cardama, A. & Kornhauser, E. Modal analysis of coupling problems in optical fibers. *IEEE Transactions on Microwave Theory and Techniques* **23,** 162–169 (1975).